Optimal Trajectories for Maneuvering Reentry Vehicles

by

Aditya Undurti

Submitted to the Department of Aeronautics and Astronautics
in partial fulfillment of the requirements for the degree of

Master of Science in Aeronautics and Astronautics

at the

MASSACHUSETTS INSTITUTE OF TECHNOLOGY

May 2007

Author . . . .
Department of Aeronautics and Astronautics
May 23, 2007

Certified by . . . .
David W. Miller, Ph.D.
Professor, Department of Aeronautics and Astronautics
Thesis Supervisor

Certified by . . . .
Ronald J. Proulx, Ph.D.
Principal Member of the Technical Staff
Thesis Supervisor

Accepted by . . . .
Jaime Peraire
Chairman, Department Committee on Graduate Students

Optimal Trajectories for Maneuvering Reentry Vehicles

by

Aditya Undurti

Submitted to the Department of Aeronautics and Astronautics
on May 23, 2007, in partial fulfillment of the
requirements for the degree of
Master of Science in Aeronautics and Astronautics

Abstract

Many demanding aerospace missions today require maneuverable re-entry vehicles that can fly trajectories that have stringent path and terminal constraints, including those that cannot be written as drag or energy constraints. This work presents a method based on trajectory optimization techniques to assess the capabilities of the re-entry vehicle by computing the landing and re-entry footprints while meeting these conditions. The models used also account for important non-linear effects seen during hypersonic flight. Several different vehicles are studied, and the effects of parameters such the maximum G-loading, stagnation point heat rate, and the maximum L/D are analyzed.

Thesis Supervisor: David W. Miller, Ph.D.
Title: Professor, Department of Aeronautics and Astronautics

Thesis Supervisor: Ronald J. Proulx, Ph.D.
Title: Principal Member of the Technical Staff

Acknowledgments

First, I would like to thank my advisor Ron Proulx at the Draper Laboratory for his guidance over the past 2 years. He has always had my concerns in mind, and has acted as a mentor to me throughout my time at Draper. I am grateful to Jim Shearer and Roy Setturlund for their invaluable advice and feedback. I would also like to thank Anil Rao for giving me valuable advice since my sophomore year, and for opening my eyes to all the opportunities at MIT and Draper.

I am also grateful to my faculty advisor Prof. David Miller for his guidance, both for this thesis and the PhD qualifying exams. I wish to thank Prof. Jonathan How for his excellent class in Optimal Control last spring, whose concepts are extensively used in this thesis. I look forward to working with him over the next 3 years for my PhD. I am grateful to all the brilliant professors in the Aero/Astro Department from whom I have learned so much.

I would like to thank all my friends at MIT - Rajiv, Vikas, Tara, Premal, Jen, Carolyn, Kranthi, Sukant, Preet, Angelin, and many, many others who have made these past 2 years some of the most fun and memorable in my life. I am already excited for 3 more years of studying in the S-P lounge, lunching in the Kendall Food Court, partying, watching movies at 4 AM, and driving around in a rented BMW.

I would like to thank my family for their incredible support - first my grandparents in India, for constantly thinking about us although we are so far away. I continue to be astonished by my grandfather's sharp mind, and my grandmother's unbounded energy and optimism. She has always taught me to realize that nothing is stronger than the strength that comes from within, and it is her advice that has carried me this far. I would also like to thank my sister Arundhati - whether to talk about life, or to watch old reruns of Star Trek, she has always been an ideal *Akka* (big sister).

And finally, I would like to thank my parents for all their advice, guidance and love. They sacrificed a life of comfort in India so that Arundhati and I could pursue our dreams. When we first arrived in this country, they had little besides the hope that we would do well. No matter how much I accomplish, nothing makes me more proud than to feel that I have met their hopes. This thesis and all the work I have put into it is dedicated to them.

This thesis was prepared at the Charles Stark Draper Laboratory, Inc., under the Trajectory Optimization Internal Research and Development Contract CON05000-2 Project ID 21127 Activity ID 001

Aditya Undurti

Assignment

Draper Laboratory Report Number T-1581.

In consideration for the research opportunity and permission to prepare my thesis by and at The Charles Stark Draper Laboratory, Inc., I hereby assign my copyright of the thesis to The Charles Stark Draper Laboratory, Inc., Cambridge, Massachusetts.

MAY 24 2007

Aditya Undurti

Date

THIS PAGE INTENTIONALLY LEFT BLANK

Contents

THIS PAGE INTENTIONALLY LEFT BLANK

List of Figures

List of Tables

THIS PAGE INTENTIONALLY LEFT BLANK

Chapter 1

Introduction

The political and military situation in the modern world is characterized by the spread of dangerous technology to unstable nations and stateless groups, both of whom might act in unpredictable ways. Furthermore, with the spread of missile technology, hostile nations and stateless groups even in distant parts of the world pose a significant threat. Therefore, the ability to deal with rapidly evolving threats and fast-changing situations anywhere in the world is essential to maintaining security in the foreseeable future.

Current capabilities, mostly developed during the Cold War, were designed for large-scale warfare against an enemy that uses conventional military tactics, with fixed strategic assets. However, in the new global environment, these capabilities are inadequate, primarily because 1) the modern enemy might not have fixed strategic assets 2) the enemy might use unconventional, unpredictable tactics and 3) current capabilities require a long time to mobilize and act upon information about new threats, while the ground situation could be changing by the hour [1].

These shortcomings point to the need for new capabilities that can 1) deal with an enemy that might not have a fixed location and can move quickly and 2) respond quickly and accurately, anywhere in the world - on time-scales of hours, rather than days. The capability to strike anywhere in the world within such a time-frame currently exists in the form of Intercontinental Ballistic Missiles (ICBMs) and Submarine-Launched Ballistic Missiles (SLBMs). However, these systems were designed to carry unconventional munitions and are therefore ill-suited to conventional precision strikes. Also, these systems are ballistic, which greatly

---

[1] E. M. Grossman, *Air Force Proposes New Strike Missile*, Military.com, April 8 2006

limits their ability to re-target upon receiving updated information about a mobile target. Finally, using these systems by simply replacing the nuclear warhead with a conventional one could lead to misinterpretation and misunderstanding by other nuclear-armed nations. Therefore another key requirement would be the ability to "geographically separate" this system from nuclear capabilities [1].

Thus there is a need for a weapons system that can carry conventional munitions, carry out precision strikes anywhere in the world, and have the ability to maneuver and re-target during flight. One suggestion [1] is to use a long-range land-based system with a maneuverable re-entry vehicle. Such a system would be separable from nuclear-capable SLBMs. When given an in-flight target update, the re-entry vehicle would have the ability to maneuver to its new target. The ability to maneuver also ensures the ability to strike with precision.

This work primarily looks at re-entry vehicles that can maneuver in the atmosphere using aerodynamic controls.

1.1 Maneuverable Re-Entry Vehicles

Several types of re-entry vehicles have been investigated in the past. Clarke investigated a "Common Aero Vehicle" (CAV), a re-entry vehicle that departs from a launch vehicle and returns to Earth with the purpose of delivering weapons, payloads or cargo to a specified location [1]. The vehicle weighs 1300-2400 lbs when fully loaded with a cross-range maneuverability of at least 2400 nautical miles, and re-enters the atmosphere at a speed of 7000 m/s and at an altitude of about 40 km. The vehicle is also assumed to have lift proportional to angle of attack, and a drag polar that increases quadratically with lift [1]. The large change in the drag coefficient and the location of the center of pressure in the transonic regime is not accounted for.

Other vehicles include the X-33 considered by Ngo and Doman [3], and Mease et. al. [6]. The X-33 is an autonomous, reusable launch vehicle with two linear aerospike engines and eight aerodynamic control surfaces: inner and outer elevons, rudders and flaps. At the beginning of the re-entry phase, the vehicle is traveling at 10,000 ft/s (about 3300 m/s) at an altitude of 180,000 feet (54,900 m) [3]. The same vehicle is also considered by Saraf et. al. [7]. Another re-entry vehicle considered (by Bairstow [8]) is the Crew Exploration Vehicle, which is designed to re-enter the Earth's atmosphere with a crew on board. This vehicle uses bank angle modulation (and in that sense is similar to the Apollo re-entry vehicles) to reach a pre-determined landing site [8]. Finally, the Space Shuttle is another re-entry vehicle which has flown successfully and whose dynamics and guidance schemes are well-understood [11] [12] [13].

The vehicle considered in this work is significantly different from any of the vehicles summarized above. This is because the missions that the new vehicle would be required to fulfill are different from the ones that the X-33, CEV and Shuttle were designed for. The new vehicle is not required to carry a crew, and is therefore subject to less strict acceleration and heat constraints than the manned vehicles. It would also be required to carry munitions such as Earth-penetrating "bunker-busters", which need to be dispensed under more physically demanding conditions than the structures of these manned vehicles could possibly handle. Finally, while the Common Aero Vehicle (CAV) is a good candidate, as Clarke states in [1], "many technical challenges stand between concept and development... [including] designing a thermal protection system, a propulsion system, a guidance and control system, and a payload release system." The constraints imposed on the CAV in [1] include a dynamic pressure constraint of 47 kPa, which corresponds to a speed of about 280 m/s at sea level. However, Earth-penetrating weapons must typically be able to fly at 1160 m/s at sea level. Finally, the aerodynamic model used does not account for important hypersonic non-linear effects, such as the large increase in drag coefficient and the large shift in the center of pressure in the transonic regime. For this reason, a vehicle that is different from all of the above is chosen.

The vehicle chosen is one designed by Textron Systems Inc. that is designed to fly at altitudes of over 72,000 feet and speeds of up to Mach 21 [14]. This vehicle has reaction jets at its base, close to the center line and also has a movable center-of-mass, which is always kept at the center of pressure of the vehicle. However, the vehicle used in this work is somewhat simpler, with a fixed center-of-mass. The aerodynamic characteristics are obtained from Textron Systems Inc. in the form of tables which give the non-dimensionalized aerodynamic coefficients as functions of angle-of-attack and Mach number. These tables capture the important non-linear aerodynamic effects of hypersonic flight, and are presented in greater detail later. A conceptual drawing of the vehicle is shown below in Figure 1.1.

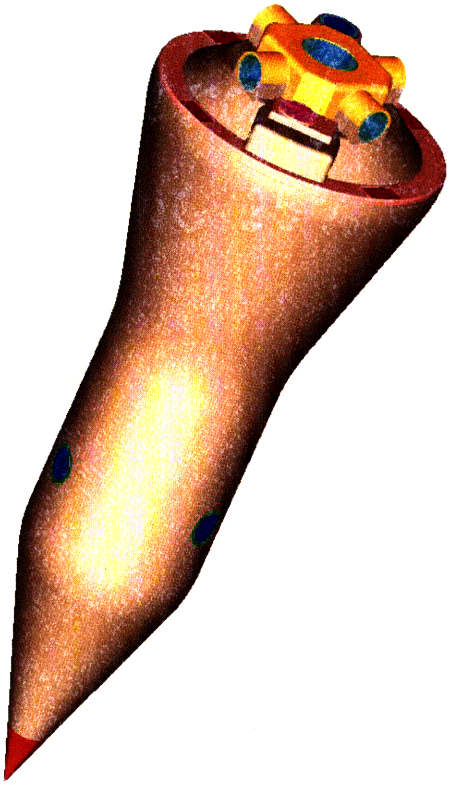

Figure 1-1: *The novel trajectory-shaping reentry vehicle designed by Textron Systems Inc.*

1.2 Mission Design and Parameters

There are two types of missions that the vehicle must be able to perform. These are 1) the Earth Penetrator mission and 2) the Submunitions deployment mission.

The Earth Penetrator mission requires the vehicle to strike its target at a speed of 3800 ft/s, with a flight path angle of $\gamma = -90$ deg on level terrain, i.e. the velocity vector must be perpendicular to the ground at impact. Also, the angle of attack of must be 0 deg, i.e. the axis of symmetry of the vehicle (the nose of the vehicle) must be aligned with the velocity vector.

The Submunitions Deployment mission requires the vehicle to end its trajectory at an altitude of 3 km at a speed of 1300 ft/s, with a flight path angle of $\gamma = 0$ deg. Thus the vehicle must be flying horizontally so that it can deploy its payload. Figure 1-2 below shows the two missions.

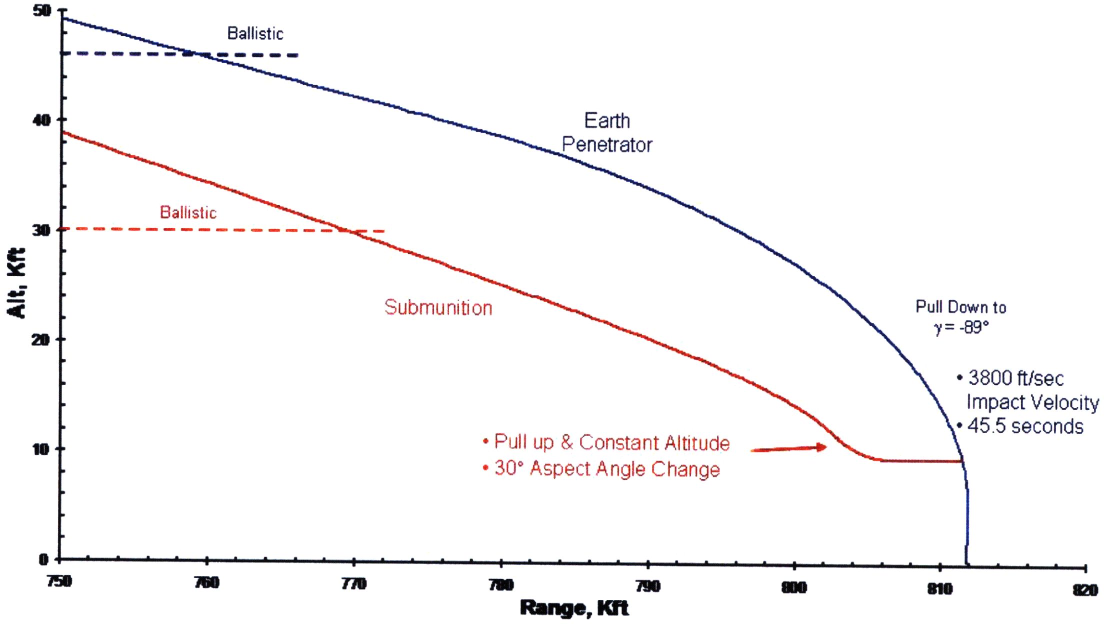

Figure 1-2: *The Earth Penetrator and Submunitions Deployment mission*

However, it is not sufficient for the vehicle to simply achieve the two missions described above. It must also be able to re-target to a different location when an in-flight target update is received. Therefore we need some measure of how much the vehicle can maneuver, and how broad an area it can reach. This "reachable" area can be defined by examining the capabilities and limits of the vehicle - in particular, the terminal points of trajectories that maximize the downrange, the minimize the uprange, and maximize the crossrange would be points lying on the outer edge of this region. In general, both in this work as well as prior work ([7], [3]) this "reachable" region is referred to as the "Footprint" of the vehicle. The larger the footprint, the greater the ability of the vehicle to re-target to a new target location. Figure 1.2 illustrates this concept.

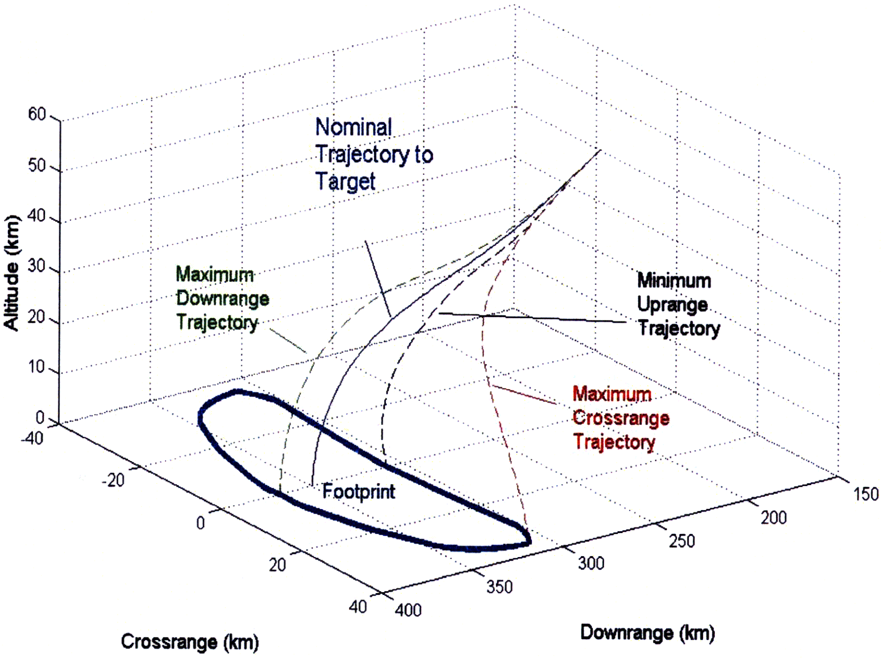

Figure 1-3: *The maximum downrange, minimum uprange and the maximum crossrange represent 3 points on the "Footprint", the outer edge of the region on the ground that can be reached by the re-entry vehicle*

There has been prior work in computing footprints, primarily landing footprints for manned vehicles with glide capability, such as the Space Shuttle [12] and the X-33 [3]. Jackson [12] and Barrows [13] use energy methods to calculate the footprint capability of the Shuttle, and use this information to plan for potential landing sites in the event of an abort. As the detailed analysis in [13] shows, this analysis is based on the assumption that the flight path angle γ is small. This, together with the "glide" assumption that lift is approximately the same as the weight ($L = W$) allows one to write an analytical solution for the flight path angle as a function of speed, L/D and other variables. However, since the types of missions being considered in this work involve flight path angles that are not small, and since the trajectories required to achieve these missions are most likely to be far from the glide condition, Jackson and Barrows' methods cannot easily be applied here. Vinh [9] also computes a landing footprint for re-entry vehicles, but uses what is essentially a shooting method to achieve the terminal conditions - a method which he remarks is "very tedious". Furthermore, he also uses the assumption of equilibrium glide to solve this complex problem. Since equilibrium glide is not a valid assumption for the current problem, Vinh's methods cannot be directly applied.

Ngo and Doman make use of ideas from optimal control theory to derive a footprint for an X-33 experiencing control effector failures [3]. This analysis also makes use of some linearizing assumptions, in particular that the flight path angle is close to zero and the normal acceleration vector is small. Since neither of these two conditions will necessarily be true for the missions being considered here, Ngo and Doman's analysis cannot easily be applied either.

Other work on calculating footprints was done by Saraf et. al. [7] making no linearizing assumptions, but their control laws require the upper bound of the flight path angle be 0 deg, i.e. $\gamma < 0$. This restriction would prevent the vehicle from skipping. As we will see later, under some initial conditions, the Textron vehicle does indeed skip for some missions. Therefore the analysis of Saraf et. al. would be too restrictive. Also, the methods presented in [7] are energy-based methods. The terminal condition on the vehicle is written as an energy condition, i.e. they incorporate terminal constraints on altitude and speed. However, there is no easy means by which to include terminal constraints on the flight path angle, which as we have seen is a mission-critical constraint. Furthermore, the method also relies on estimating angle-of-attack profiles which may be difficult to do in the case of highly non-linear aerodynamics. Finally, we will see that the Textron vehicle demonstrates behavior such as out-of-plane maneuvers which would be hard to reproduce with the approximate method. For these reasons, the methods presented by Saraf et. al. do not seem to apply to the vehicle and missions under consideration.

Clearly, the nature of the missions and the aerodynamics of the vehicle are non-linear, and the non-linear effects are likely to be important. Therefore, any technique used to solve this problem must be able to handle this non-linear behavior. Non-linear dynamics can be handled well using methods from Optimal Control [25]. Furthermore, since the computation of the footprint involves computing extremal quantities such as the *maximum* downrange, the *minimum* uprange and *maximum* crossrange, Optimal Control methods lend themselves well to solving this problem.

Prior work in using optimal control methods to design trajectories for systems with non-linear dynamics has been done by K. P. Bollino and I. M. Ross [4], P. F. Shaffer and I. M. Ross [5], K. D. Mease et. al. [6], as well as Clarke [1]. In [4], Bollino and Ross showed that trajectories for a re-entry vehicle with non-linear aerodynamics could be computed efficiently using pseudospectral methods to solve the Optimal Control problem. This formulation allowed the authors to incorporate terminal conditions on not just the speed and altitude, but the flight path angle as well. Shaffer and Ross use the same methods to compute trajectories for re-entry vehicles experiencing control surface failures [5]. Mease et. al. compare two methods - one where the angle-of-attack profile is specified and a feasible trajectory generated for that profile, and another which uses optimal control methods. They show that optimal control methods allows for greater capability to shape the trajectory, and is capable of achieving specified terminal conditions (such as the final heading angle) [6].

In this work, we combine the landing footprint concept (similar to the ideas presented in Saraf [7], Jackson [12]) with the trajectory optimization methods which have been used successfully by Ross and Bollino [4] and Ross and Shaffer [5]. This allows us to compute the footprint capability of the Textron vehicle even while accounting for the non-linear aerodynamics and flight path angle constraints, both of which will play an important role in the behavior of the vehicle. We will further extend the idea of the "landing footprint" by defining a "re-entry footprint," which can be seen as the region in the state space at re-entry ("piercepoint") from which a vehicle can reach a given target. This and other concepts will be explained in greater detail later in the work.

The numerical method used in solving this complex optimal control problem is the Pseudospectral method as implemented in DIDO, an object-oriented computer program for solving dynamic optimization problems [15]. Similar pseudospectral methods were used by Ross and Bollino [4], Ross and Shaffer [5], and Clarke [1]. In general, direct methods such as collocation [20] and pseudospectral methods [21] have been shown to be more efficient than other procedures for a wide variety of problems. DIDO is capable of solving smooth and non-smooth hybrid optimal control problems defined over a time interval that may be fixed or free [15]. Once the dynamic model of the vehicle is developed, and the optimal control problem formulated, DIDO will be used to numerically solve the problem. The dynamic model and the formulation of the optimal control problem are presented in the following sections.

Chapter 2

Coordinate Frames

In the formulation of the dynamics of the vehicle, we use the following coordinate frames:

- Earth Centered Inertial Frame (ECI)
- Earth Centered Earth Fixed Frame (ECEF)
- East-Up-South Frame (EUS), also called the Local-Vertical Local-Horizontal Frame (L)
- Velocity Frame (V)
- Body Frame (B)

2.1 Earth Centered Inertial Frame (ECI)

The Earth-Centered Inertial Frame is a right-handed coordinate frame fixed in inertial space and centered at the center of the Earth. The x-axis $\mathbf{x_I}$ points passes through 0 degrees latitude and 0 degrees longitude at a time $t = 0$, the z-axis $\mathbf{z_I}$ points in the direction of the Earth's rotation, and the y-axis $\mathbf{y_I} = \mathbf{z_I} \times \mathbf{x_I}$ completes the right-handed coordinate system.

2.2 Earth Centered Earth Fixed Frame (ECEF)

The Earth Centered Earth Fixed frame is a right handed coordinate frame that is fixed to the Earth at all times and centered at the center of the Earth. This frame rotates with the Earth, and is therefore not inertial. The x-axis $\mathbf{x_E}$ passes through 0 degrees latitude and 0 degrees longitude at all times, the z-axis $\mathbf{z_E}$ points in the direction of the Earth's rotation, and the y-axis $\mathbf{y_E} = \mathbf{z_E} \times \mathbf{x_E}$ completes the right-handed coordinate system.

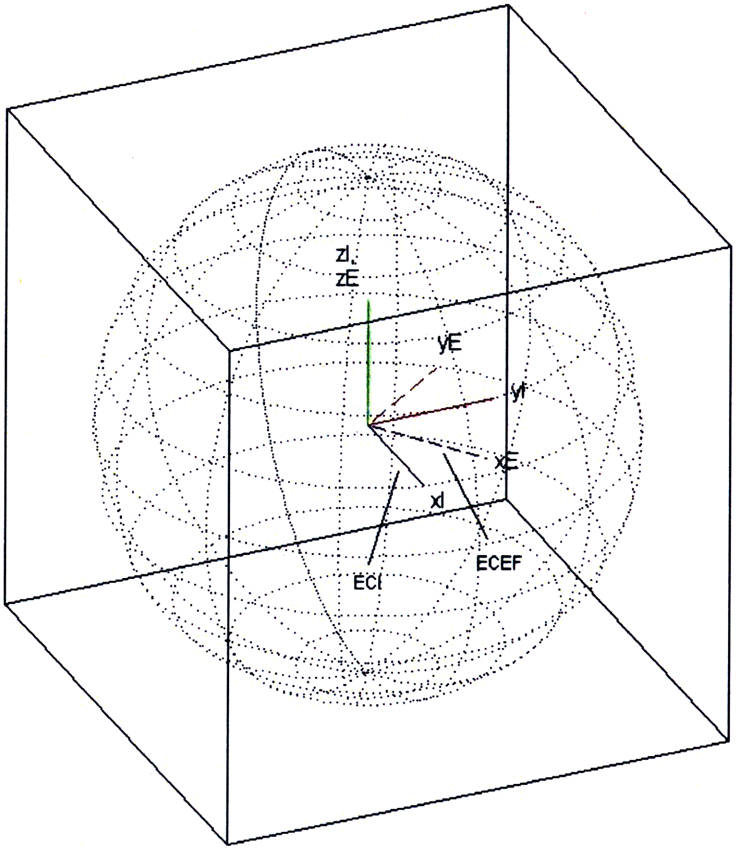

Figure 2-1: The figure shows the relation between the Earth-Centered Inertial (ECI) frame and the Earth-Centered Earth-Fixed (ECEF) frame

The transformation to go from ECI to ECEF is a straightforward rotation of the ECI axis about the $\mathbf{z_E} = \mathbf{z_I}$ axis by an angle $\omega_E t$ where ω_E is the rotation rate of the Earth and t is the time elapsed since the definition of the ECI frame. In the Earth model used throughout this work, the rotation rate is assumed to be constant in both magnitude and direction (no precession or nutation).

$$\mathbf{T_I^E} = \begin{bmatrix} \cos\omega_E t & \sin\omega_E t & 0 \\ -\sin\omega_E t & \cos\omega_E t & 0 \\ 0 & 0 & 1 \end{bmatrix}$$

The rotation rate of the ECEF frame with respect to the ECI frame is given by

$$\omega_{\mathbf{I}}^{\mathbf{E}} = \omega_E \mathbf{z_I}$$

2.3 East-Up-South Frame (EUS)

The East-Up-South Frame is a non-inertial frame centered at the position of the center of mass of the vehicle. The x-axis $\mathbf{x_L}$ points to the East, the y-axis $\mathbf{y_L}$ points away from the center of the Earth and the z-axis $\mathbf{z_L} = \mathbf{x_L} \times \mathbf{y_L}$ points South. The Earth is assumed to be perfectly spherical.

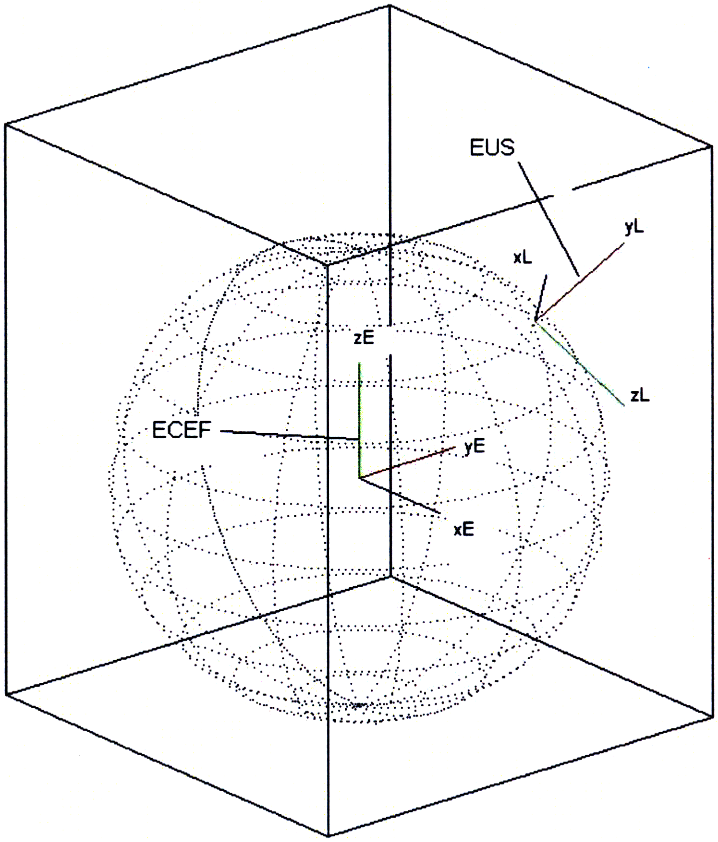

Figure 2-2: The figure shows the relation between the Earth-Centered ECEF frame and the East-Up-South frame

The transformation to go from ECEF to the EUS frame is obtained by first rotating the ECEF frame about the $\mathbf{z_E}$ axis by the longitude μ, then rotating about the new y-axis by the latitude λ. This frame now has its x-axis pointed in the radially outward direction (from the center of the Earth), the y-axis pointed East, and the z-axis pointed North. To turn this Up-East-North frame into the East-Up-South frame, we rotate about the new z-axis by $\pi/2$, and then about the new x-axis by π. Note that this frame is similar to the North-East-Down frame that is more commonly used, but with the x-axis in the East direction (instead of North), and the Up direction defined as positive (instead of Down). The overall transformation can be written as

$$\mathbf{T_E^L} = \begin{bmatrix} 1 & 0 & 0 \\ 0 & \cos\pi & \sin\pi \\ 0 & -\sin\pi & \cos\pi \end{bmatrix} \begin{bmatrix} \cos\pi/2 & \sin\pi/2 & 0 \\ -\sin\pi/2 & \cos\pi/2 & 0 \\ 0 & 0 & 1 \end{bmatrix} \begin{bmatrix} \cos\lambda & 0 & -\sin\lambda \\ 0 & 1 & 0 \\ \sin\lambda & 0 & \cos\lambda \end{bmatrix} \begin{bmatrix} \cos\mu & \sin\mu & 0 \\ -\sin\mu & \cos\mu & 0 \\ 0 & 0 & 1 \end{bmatrix}$$

$$\mathbf{T_E^L} = \begin{bmatrix} -\sin\mu & \cos\mu & 0 \\ \cos\lambda\cos\mu & \cos\lambda\sin\mu & -\sin\lambda \\ -\cos\mu\sin\lambda & -\sin\lambda\sin\mu & -\cos\lambda \end{bmatrix}$$

The rotation rate of the EUS frame with respect to the ECEF frame is given by

$$\omega_{\mathbf{E}}^{\mathbf{L}} = \dot{\mu}\mathbf{z_E} + \dot{\lambda}\mathbf{x'_E}$$

Where $\mathbf{x'_E}$ is the vector obtained from rotating the $\mathbf{x_E}$ vector about the $\mathbf{z_E}$ direction by angle μ. Therefore

$$\mathbf{x'_E} = \begin{bmatrix} \cos\mu & -\sin\mu & 0 \\ \sin\mu & \cos\mu & 0 \\ 0 & 0 & 1 \end{bmatrix} \mathbf{x_E}$$

$$\mathbf{x'_E} = \cos\mu\mathbf{x_E} + \sin\mu\mathbf{y_E}$$

Therefore we get

$$\omega_{\mathbf{E}}^{\mathbf{L}} = \dot{\lambda}\cos\mu\mathbf{x_E} + \dot{\lambda}\sin\mu\mathbf{y_E} + \dot{\mu}\mathbf{z_E}$$

2.4 Velocity Frame (V)

The Velocity frame is a non-inertial frame centered at the position of the center of mass of the vehicle, and is given by rotating the EUS frame about the $-\mathbf{y_L}$ axis by the heading angle ψ and then about the new $\mathbf{z_L}$ axis by the flight path angle γ. Thus the x-axis of the V frame $\mathbf{x_V}$ is coincident with the direction of the velocity vector.

The transformation from the EUS frame to the V frame is given by a rotation about the y-axis by angle ψ followed by a rotation about the z-axis by an angle γ.

$$\mathbf{T_L^V} = \begin{bmatrix} \cos\gamma & \sin\gamma & 0 \\ -\sin\gamma & \cos\gamma & 0 \\ 0 & 0 & 1 \end{bmatrix} \begin{bmatrix} \cos\psi & 0 & \sin\psi \\ 0 & 1 & 0 \\ -\sin\psi & 0 & \cos\psi \end{bmatrix}$$

$$\mathbf{T_L^V} = \begin{bmatrix} \cos\psi\cos\gamma & \sin\gamma & \cos\gamma\sin\psi \\ -\cos\psi\sin\gamma & \cos\gamma & -\sin\gamma\sin\psi \\ -\sin\psi & 0 & \cos\psi \end{bmatrix}$$

The rotation rate of the V frame with respect to the EUS frame is

$$-\dot{\psi}\mathbf{y_L} + \dot{\gamma}\mathbf{z_V}$$

Since $\mathbf{z_V} = T_V^L\mathbf{z_L} = T_L^{V^T}\mathbf{z_L} = -\sin\psi\mathbf{x_L} + \cos\psi\mathbf{z_L}$,

$$-\dot{\psi}\mathbf{y_L} - \dot{\gamma}\sin\psi\mathbf{x_L} + \dot{\gamma}\cos\psi\mathbf{z_L}$$

2.5 Body Frame (B)

The Body frame is a non-inertial frame centered at the position of the center of mass of the vehicle and is fixed to the vehicle. The x-axis is coincident with the main axis (the axis of asymmetry) of the vehicle, while the y-axis and the z-axis are chosen such that they are both normal to the x-axis and to each other. Since the vehicle is assumed to have axial symmetry, the exact orientation of the y and z axes in the y-z plane can be chosen arbitrarily, as long as they remain orthogonal.

The transformation from the V frame to the B frame is given by a rotation about the y-axis by angle θ followed by a rotation about the z-axis by an angle ϕ.

$$\mathbf{T_V^B} = \begin{bmatrix} \cos\phi & \sin\phi & 0 \\ -\sin\phi & \cos\phi & 0 \\ 0 & 0 & 1 \end{bmatrix} \begin{bmatrix} \cos\theta & 0 & \sin\theta \\ 0 & 1 & 0 \\ -\sin\theta & 0 & \cos\theta \end{bmatrix}$$

$$\mathbf{T_V^B} = \begin{bmatrix} \cos\theta\cos\phi & \sin\phi & \cos\phi\sin\theta \\ -\cos\theta\sin\phi & \cos\phi & -\sin\phi\sin\theta \\ -\sin\theta & 0 & \cos\theta \end{bmatrix}$$

The rotation rate of the B frame with respect to the V frame is given by

$$\omega_{\mathbf{V}}^{\mathbf{B}} = -\dot{\theta}\mathbf{y_V} + \dot{\phi}\mathbf{z_B}$$

Since $\mathbf{z_B} = T_B^V \mathbf{z_V} = T_V^{B^T} \mathbf{z_V} = -\sin\theta\mathbf{x_V} + \cos\theta\mathbf{z_V}$,

$$\omega_{\mathbf{V}}^{\mathbf{B}} = -\dot{\phi}\sin\theta\mathbf{x_V} - \dot{\theta}\mathbf{y_V} + \dot{\phi}\cos\theta\mathbf{z_V}$$

The attitude of the body can be written in terms of not just θ and ϕ, but in terms of the aerodynamic angles - the angle of attack α and the lift bank angle σ. The angle of attack is the angle between the axis of symmetry of the vehicle and the velocity vector, i.e. the angle between $\mathbf{x_B}$ and $\mathbf{x_V}$. For an axially symmetric body, the lift bank angle σ is defined by first finding the plane in which the angle of attack α lies, and then calculating the angle that plane makes with the $\mathbf{x_V}, \mathbf{y_V}$ plane. If $\sigma = 0$, then the angle of attack lies in the $\mathbf{x_V}, \mathbf{y_V}$ plane.

Based on the definitions above, we can relate the aerodynamic angles α and σ to the Euler angles θ and ϕ.

$$\cos\alpha = \mathbf{x_B}.\mathbf{x_V}$$

Using the transformation T_V^B, to write $\mathbf{x_V} = \cos\theta\cos\phi\mathbf{x_V} - \sin\phi\mathbf{y_V} - \cos\phi\sin\theta\mathbf{z_V}$, we get

$$\cos \alpha = \cos \theta \cos \phi \tag{2.1}$$

To find σ, first we find the normal vector to the plane in which α lies. This is given by

$$\mathbf{n} = \frac{\mathbf{x_V} \times \mathbf{x_B}}{|\mathbf{x_V} \times \mathbf{x_B}|} \tag{2.2}$$

We can easily show that

$$\mathbf{x_V} \times \mathbf{x_B} = -\cos \theta \sin \phi \mathbf{z_B} + \sin \theta \mathbf{y_B}$$

Therefore

$$\mathbf{n} = \frac{-\sin \phi \cos \theta \mathbf{z_B} + \sin \theta \mathbf{y_B}}{\sqrt{\sin \theta^2 + \cos \theta^2 \sin \phi^2}}$$

We can rewrite the $\mathbf{n}$ vector in the V frame using the coordinate transformation T_B^V. This can be shown to give

$$\mathbf{n} = \frac{-\sin \phi \cos \theta \mathbf{z_B} + \sin \theta \mathbf{y_B}}{\sqrt{\sin \theta^2 + \cos \theta^2 \sin \phi^2}} = \frac{\sin \theta \cos \phi \mathbf{y_V} - \sin \phi \mathbf{z_V}}{\sqrt{\sin \theta^2 + \cos \theta^2 \sin \phi^2}}$$

Next, we see that by definition

$$\mathbf{n}.\mathbf{y_V} = \cos (\pi/2 - \sigma) = \sin \sigma$$

Therefore we can relate σ to θ and ϕ by

$$\sin \sigma = \frac{\cos \phi \sin \theta}{\sqrt{\sin^2 \theta + \cos^2 \theta \sin^2 \phi}} \tag{2.3}$$

Equations (2.1) and (2.3) tell us how to compute α and σ from θ and ϕ. We can rewrite the equations to get θ and ϕ in terms of α and σ. From Equation 2.3 we get

$$\frac{\cos^2\phi\sin^2\theta}{\sin^2\theta+\cos^2\theta(1-\cos^2\phi)}=\sin^2\sigma$$

$$\frac{\cos^2\phi-\cos^2\theta\cos^2\phi}{1-\cos^2\phi\cos^2\theta}=\sin^2\sigma$$

Using Equation (2.1) we get

$$\frac{\cos^2\phi-\cos^2\alpha}{1-\cos^2\alpha}=\sin^2\sigma$$

$$\cos^2\phi=\cos^2\alpha+\sin^2\alpha\sin^2\sigma$$

Thus for the angle ϕ we get the following relation in terms of α and σ

$$\cos\phi=\sqrt{\cos^2\alpha+\sin^2\alpha\sin^2\sigma} \tag{2.4}$$

Now using Equation (2.1), and using the result from Equation (2.4) above, we get for θ

$$\cos\theta=\frac{\cos\alpha}{\sqrt{\sin^2\alpha\sin^2\sigma+\cos^2\alpha}} \tag{2.5}$$

Next we will write the angular rotation of the B frame with respect to the V frame in terms of the angles α, σ and their rates $\dot{\alpha}$ and $\dot{\sigma}$. We start by writing the angular velocity as

$$\omega_{\mathbf{V}}^{\mathbf{B}}=-\dot{\alpha}\mathbf{n}-\dot{\sigma}\mathbf{x_V}$$

Using Equation (2.2) for $\mathbf{n}$ we get

$$\omega_{\mathbf{V}}^{\mathbf{B}}=\dot{\alpha}\left(\frac{-\sin\theta\cos\phi\mathbf{y_V}+\sin\phi\mathbf{z_V}}{\sqrt{\sin^2\theta+\cos^2\theta\sin^2\phi}}\right)-\dot{\sigma}\mathbf{x_V}$$

$$\omega_{\mathbf{V}}^{\mathbf{B}} = \frac{-\dot{\alpha}\sin\theta\cos\phi}{\sqrt{\sin^2\theta + \cos^2\theta\sin^2\phi}}\mathbf{y_V} + \frac{\dot{\alpha}\sin\phi}{\sqrt{\sin^2\theta + \cos^2\theta\sin^2\phi}}\mathbf{z_V} - \dot{\sigma}\mathbf{x_V} \tag{2.6}$$

Simplifying the $\mathbf{y_B}$ term first, we see that the denominator is

$$\sqrt{\sin^2\theta + \cos^2\theta\sin^2\phi} = \sqrt{\sin^2\theta + \cos^2\theta(1-\cos^2\phi)} = \sqrt{1-\cos^2\phi\cos^2\theta}$$

Using Equation (2.1) we get

$$\sqrt{1-\cos^2\phi\cos^2\theta} = \sqrt{1-\cos^2\alpha} = \sin\alpha \tag{2.7}$$

The numerator of the $\mathbf{y_V}$ term in Equation (2.6) is

$$\sin\theta\cos\phi = \sqrt{(1-\cos^2\theta)\cos^2\phi} = \sqrt{\cos^2\phi - \cos^2\alpha} = \sqrt{\sin^2\alpha\sin^2\sigma} = \sin\alpha\sin\sigma \tag{2.8}$$

where we have used the result from Equation (2.4) for $\cos\phi$.

Next we look at the $\mathbf{z_V}$ term in Equation (2.6). Since this term has a $\sin\phi$ in it, we first write $\sin\phi$ in terms of α and σ

$$\sin\phi = \sqrt{1-\cos^2\phi} = \sqrt{1-\cos^2\alpha - \sin^2\alpha\sin^2\sigma} = \sin\alpha\cos\sigma \tag{2.9}$$

Using Equations (2.7), (2.8) and (2.9), together with Equation (2.4), in Equation (2.6) we get

$$\omega_{\mathbf{V}}^{\mathbf{B}} = -\dot{\alpha}\sin\sigma\mathbf{y_V} + \dot{\alpha}\cos\sigma\mathbf{z_V} - \dot{\sigma}\mathbf{x_V} \tag{2.10}$$

Chapter 3

Dynamics

3.1 4 Degrees-Of-Freedom Rotating Earth Model

The motion of the re-entry vehicle is modeled as a standard 3-DOF system with a quadratic lag in the control system. The states of the basic 3-DOF system are the radius (distance from the center of the Earth) r, the longitude μ, the latitude λ, the speed V, the flight path angle γ and the heading angle ψ. The controls for a standard 3-DOF system would be the angle of attack α and the lift vector direction σ. However, since a quadratic lag is assumed in the control system, the actual controls are the commanded angle of attack α_c and the commanded lift vector direction σ_c. The actual angle of attack α, and the lift vector direction σ, as well as the rates of change of these two quantities $\beta = \dot{\alpha}$ and $\tau = \dot{\sigma}$ are considered states. Thus we have a 4-DOF system with 8 states in total.

The rotation of the Earth is an important factor when designing a trajectory, particularly if the trajectory is of long duration. For instance, if a trajectory is 15 minutes long, the Earth would have rotated 2.5 degrees during that time - a difference of almost 280 km. Therefore the rotation of the Earth needs to be considered. Furthermore, the sphericity of the Earth must also be accounted for, particularly if the distances traversed are of the comparable order of magnitude as the mean radius of the Earth (6378.1 km).

Taking into account all these factors, we get the following 4-DOF system, which is similar to the models used in similar work, such as Ross and Bollino [4].

$$
\begin{aligned}
\dot{r} &= V \sin\gamma \\
\dot{\mu} &= \frac{V \cos\psi \cos\gamma}{r \cos\lambda} \\
\dot{\lambda} &= \frac{V \cos\gamma \sin\psi}{r} \\
\dot{V} &= -\frac{D}{m} - g \sin\gamma \\
&+ \Omega^2 r \cos\lambda \left(\sin\gamma \cos\lambda - \cos\gamma \sin\lambda \sin\psi\right) \\
\dot{\gamma} &= \frac{L \cos\sigma}{mV} + \left(\frac{V}{r} - \frac{g}{V}\right) \cos\gamma \\
&+ 2\Omega \cos\lambda \cos\psi + \frac{\Omega^2 r}{V} \cos\lambda \left(\cos\gamma \cos\lambda + \sin\gamma \sin\lambda \sin\psi\right) \\
\dot{\psi} &= \frac{L \sin\sigma}{mV \cos\gamma} - \frac{V}{r} \cos\gamma \cos\psi \tan\lambda \\
&+ 2\Omega \left(\tan\gamma \cos\lambda \sin\psi - \sin\lambda\right) - \frac{\Omega^2 r}{V \cos\gamma} \sin\gamma \cos\lambda \cos\psi \\
\dot{\alpha} &= \beta \\
\dot{\beta} &= -2\zeta\omega\beta - \omega^2 \left(\alpha_c - \alpha\right) \\
\dot{\sigma} &= \tau \\
\dot{\tau} &= -2\zeta\omega\tau - \omega^2 \left(\sigma_c - \sigma\right)
\end{aligned}
\tag{3.1}
$$

Ω is the rotation rate of the Earth, 7.2921150000e-05 rad/s. L is the lift (defined as the total aerodynamic force acting normal to the velocity vector), D is the drag (defined as the total aerodynamic force acting parallel to the velocity vector), m is the mass of the vehicle, ζ and ω are parameters that together define the characteristics of the second-order lag.

The aerodynamic forces on the vehicle are the lift L and the drag D, which in general can be written as

$$
\begin{aligned}
L &= \frac{1}{2}\rho(x, y, z) V^2 C_L(\alpha, M) S \\
D &= \frac{1}{2}\rho(x, y, z) V^2 C_D(\alpha, M) S
\end{aligned}
$$

C_L is the lift coefficient and C_D is the drag coefficient, and are both functions of the angle of attack α and the Mach number M. S the reference area is a property of the vehicle. ρ is the atmospheric density, and is in general a function of position, particularly altitude. Although ρ is also a function of time (for instance, the time of day, season and year), it is assumed to be a constant for the duration of the trajectories being considered. In general, the actual density on any given day and at any given time will deviate from its predicted value even with the best atmospheric models, but these small deviations (which may be considered as noise) are also ignored.

3.1.1 Singularity

Note that the equation for the heading angle (ψ) has a singularity at $\gamma = \frac{\pi}{2}$, because one of the terms in right side of the expression for $\dot{\psi}$ is $\frac{L \sin\sigma}{mV \cos\gamma}$.

This singularity can be handled by constraining $\sigma = 0$ in the terminal stages. Physically, this means that the lift vector must stay in the $\mathbf{y_V}, \mathbf{x_V}$ plane in the V frame. Setting $\sigma = 0$ does not directly effect the right-hand side of $\dot{r}$, $\dot{\mu}$, $\dot{\lambda}$ and $\dot{V}$ in Equations 3.1, but the expressions for the other states simplify as follows:

$$
\begin{aligned}
\dot{\gamma} &= \frac{L}{mV} + \left(\frac{V}{r} - \frac{g}{V}\right)\cos\gamma \\
&+ 2\Omega\cos\lambda\cos\psi + \frac{\Omega^2 r}{V}\cos\lambda\left(\cos\gamma\cos\lambda + \sin\gamma\sin\lambda\sin\psi\right) \\
\dot{\psi} &= -\frac{V}{r}\cos\gamma\cos\psi\tan\lambda \\
&+ 2\Omega\left(\tan\gamma\cos\lambda\sin\psi - \sin\lambda\right) - \frac{\Omega^2 r}{V\cos\gamma}\sin\gamma\cos\lambda\cos\psi \\
\dot{\alpha} &= \beta \\
\dot{\beta} &= -2\zeta\omega\beta - \omega^2\left(\alpha_c - \alpha\right) \\
\sigma &= 0 \\
\tau &= 0
\end{aligned}
\qquad (3.2)
$$

Note that despite fixing σ to 0, the heading angle might change because of the natural curvature and rotation of the Earth.

However, it is unphysical for the system to have discontinuous states or rates of change.

Therefore the following continuity conditions must be imposed between the first phase (when σ is not constrained to be 0, and the motion is governed by Equations (3.1)) and the second phase (when $\sigma = 0$ and the motion is governed by Equations (3.2)). The continuity conditions required to ensure that the model is physical are:

$$r_{1f} = r_{2i}$$

$$\dot{r}_{1f} = \dot{r}_{2i}$$

$$\mu_{1f} = \mu_{2i}$$

$$\dot{\mu}_{1f} = \dot{\mu}_{2i}$$

$$\lambda_{1f} = \lambda_{2i}$$

$$\dot{\lambda}_{1f} = \dot{\lambda}_{2i}$$

$$V_{1f} = V_{2i}$$

$$\dot{V}_{1f} = \dot{V}_{2i}$$

$$\gamma_{1f} = \gamma_{2i}$$

$$\dot{\gamma}_{1f} = \dot{\gamma}_{2i}$$

$$\psi_{1f} = \psi_{2i}$$

$$\dot{\psi}_{1f} = \dot{\psi}_{2i}$$

$$\alpha_{1f} = \alpha_{2i}$$

$$\dot{\alpha}_{1f} = \dot{\alpha}_{2i}$$

$$\sigma_{1f} = \sigma_{2i} = 0$$

$$\dot{\sigma}_{1f} = \dot{\sigma}_{2i} = 0$$

x_{1f} is the final value of state x at the end of the first phase, and x_{2i} is the initial value of the state x at the beginning of the second phase, and so on.

3.2 4 Degrees-of-Freedom Spherical Earth Model

When the flight time associated with a trajectory is small enough for the rotation of the Earth to be ignored, the 4-DOF rotating Earth model can be greatly simplified by letting the rotation rate of the Earth $\Omega = 0$. This can be done because the Coriolis acceleration is typically of the order $10^{-3}g$ [9]. Several terms on the right hand side of Equations (3.1) can be ignored and the dynamics simply as shown below.

$$\begin{aligned}
\dot{r} &= V \sin\gamma \\
\dot{\mu} &= \frac{V\cos\psi\cos\gamma}{r\cos\lambda} \\
\dot{\lambda} &= \frac{V\cos\gamma\sin\psi}{r} \\
\dot{V} &= -\frac{D}{m} - g\sin\gamma \\
\dot{\gamma} &= \frac{L\cos\sigma}{mV} + \left(\frac{V}{r} - \frac{g}{V}\right)\cos\gamma \\
\dot{\psi} &= \frac{L\sin\sigma}{mV\cos\gamma} - \frac{V}{r}\cos\gamma\cos\psi\tan\lambda \\
\dot{\alpha} &= \beta \\
\dot{\beta} &= -2\zeta\omega\beta - \omega^2\left(\alpha_c - \alpha\right) \\
\dot{\sigma} &= \tau \\
\dot{\tau} &= -2\zeta\omega\tau - \omega^2\left(\sigma_c - \sigma\right)
\end{aligned} \tag{3.3}$$

The model derived here is essentially the same as used by Lianghui et. al. in [16], with additional states due to the quadratic lag that has been built into the control system. Note that this model has the same singularity as in Equations (3.1) but this singularity can be handled in exactly the same way as in the rotating Earth case. The resulting model would look exactly like Equations (3.2) with $\Omega = 0$.

3.3 4 Degrees-of-Freedom Flat Earth Model

Examining the spherical Earth model in Equations (3.3), we see that the model simplifies significantly when the radius of the Earth is much greater than the distances traveled by the vehicle in its trajectory, i.e. the Earth can be treated as being flat.

We derive the flat-Earth model by setting $r = R_e + h$, where R_e is the radius of the Earth and h is the height above the surface of the Earth, i.e. the altitude [9]. The equations for the states thus become

$$
\begin{aligned}
\dot{h} &= V \sin\gamma \\
\dot{\mu} &= \frac{V\cos\psi\cos\gamma}{(R_e + h)\cos\lambda} \\
\dot{\lambda} &= \frac{V\cos\gamma\sin\psi}{R_e + h} \\
\dot{V} &= -\frac{D}{m} - g\sin\gamma \\
\dot{\gamma} &= \frac{L\cos\sigma}{mV} + \left(\frac{V}{R_e + h} - \frac{g}{V}\right)\cos\gamma \\
\dot{\psi} &= \frac{L\sin\sigma}{mV\cos\gamma} - \frac{V}{R_e + h}\cos\gamma\cos\psi\tan\lambda \\
\dot{\alpha} &= \beta \\
\dot{\beta} &= -2\zeta\omega\beta - \omega^2(\alpha_c - \alpha) \\
\dot{\sigma} &= \tau \\
\dot{\tau} &= -2\zeta\omega\tau - \omega^2(\sigma_c - \sigma)
\end{aligned}
$$

Assuming flat Earth essentially means assuming that $R_e >> h$, and so we replace all instances of $R_e + h$ by R_e.

$$
\begin{aligned}
\dot{h} &= V \sin\gamma \\
\dot{\mu} &= \frac{V\cos\psi\cos\gamma}{(R_e)\cos\lambda} \\
\dot{\lambda} &= \frac{V\cos\gamma\sin\psi}{R_e}
\end{aligned}
$$

$$\begin{aligned}
\dot{V} &= -\frac{D}{m} - g\sin\gamma \\
\dot{\gamma} &= \frac{L\cos\sigma}{mV} + \left(\frac{V}{R_e} - \frac{g}{V}\right)\cos\gamma \\
\dot{\psi} &= \frac{L\sin\sigma}{mV\cos\gamma} - \frac{V}{R_e}\cos\gamma\cos\psi\tan\lambda \\
\dot{\alpha} &= \beta \\
\dot{\beta} &= -2\zeta\omega\beta - \omega^2(\alpha_c - \alpha) \\
\dot{\sigma} &= \tau \\
\dot{\tau} &= -2\zeta\omega\tau - \omega^2(\sigma_c - \sigma)
\end{aligned}$$

The downrange distance traveled is $R_\lambda\mu$, where R_λ is the radius of the circle defined by a latitude λ. Therefore $R_\lambda = R_e\cos\lambda$. The crossrange distance traveled is $R_e\lambda$ (note that there is no additional $\cos\mu$ term because longitudes are defined as great circles while latitudes are defined as being parallel to the equator). Thus setting $x = R_e\mu\cos\lambda$ and $z = R_e\lambda$, and $h = y$, we get

$$\begin{aligned}
\dot{x} &= V\cos\psi\cos\gamma \\
\dot{y} &= V\sin\gamma \\
\dot{z} &= V\cos\gamma\sin\psi \\
\dot{V} &= -\frac{D}{m} - g\sin\gamma \\
\dot{\gamma} &= \frac{L\cos\sigma}{mV} + \left(\frac{V}{R_e} - \frac{g}{V}\right)\cos\gamma \\
\dot{\psi} &= \frac{L\sin\sigma}{mV\cos\gamma} - \frac{V}{R_e}\cos\gamma\cos\psi\tan\lambda \\
\dot{\alpha} &= \beta \\
\dot{\beta} &= -2\zeta\omega\beta - \omega^2(\alpha_c - \alpha) \\
\dot{\sigma} &= \tau \\
\dot{\tau} &= -2\zeta\omega\tau - \omega^2(\sigma_c - \sigma)
\end{aligned}$$

Finally, when we let $R_e \to \infty$, we see that several terms drop out and we get the flat Earth model [9].

$$\begin{aligned}
\dot{x} &= V\cos\psi\cos\gamma \\
\dot{y} &= V\sin\gamma \\
\dot{z} &= V\cos\gamma\sin\psi \\
\dot{V} &= -\frac{D}{m} - g\sin\gamma \\
\dot{\gamma} &= \frac{L\cos\sigma}{mV} + -\frac{g}{V}\cos\gamma \\
\dot{\psi} &= \frac{L\sin\sigma}{mV\cos\gamma} \\
\dot{\alpha} &= \beta \\
\dot{\beta} &= -2\zeta\omega\beta - \omega^2\left(\alpha_c - \alpha\right) \\
\dot{\sigma} &= \tau \\
\dot{\tau} &= -2\zeta\omega\tau - \omega^2\left(\sigma_c - \sigma\right)
\end{aligned} \tag{3.4}$$

3.3.1 Singularity

The equation for the heading angle (ψ) still has the singularity at $\gamma = \frac{\pi}{2}$, due to the term

$$\dot{\psi} = \frac{L\sin\sigma}{mV\cos\gamma}$$

We deal with this singularity the same way as before - by constraining $\sigma = 0$ in the terminal stages. Thus the equations of motion in the flat Earth case at the terminal phase of the trajectory reduce to

$$\begin{aligned}
\dot{x} &= V\cos\psi_0\cos\gamma \\
\dot{y} &= V\sin\gamma \\
\dot{z} &= V\sin\psi_0\cos\gamma \\
\dot{V} &= -\frac{D}{m} - g\sin\gamma \\
\dot{\gamma} &= \frac{L}{mV} - \frac{g\cos\gamma}{V}
\end{aligned} \tag{3.5}$$

$$
\begin{aligned}
\dot{\psi} &= 0 \\
\dot{\alpha} &= \beta \\
\dot{\beta} &= -2\zeta\omega\beta - \omega^2\left(\alpha_c - \alpha\right) \\
\sigma &= 0 \\
\tau &= 0
\end{aligned}
$$

Note that in the flat Earth case, setting $\sigma =$ also constrains the heading angle ψ to remain constant, ψ_0. The continuity conditions are the same as presented in the rotating Earth case, with the additional constraint that

$$
\begin{aligned}
\psi_{1f} &= \psi_{2i} = \psi_0 \\
\dot{\psi_{1f}} &= \dot{\psi_{2i}} = 0
\end{aligned}
$$

3.4 3 Degrees-of-Freedom Flat Earth Model

The equations of motion of the vehicle can be simplified if no lag is assumed between the commanded angle of attack α_c and the actual angle of attack α, as well as the commanded lift vector direction σ_c and the actual lift vector direction σ. This eliminates the four states α, β, τ and σ and replaces the controls α_c and σ_c by α and σ. The resulting simplified 3-DOF system is shown below.

$$\begin{aligned}
\dot{x} &= V\cos\psi\cos\gamma \\
\dot{y} &= V\sin\psi\cos\gamma \\
\dot{z} &= V\sin\gamma \\
\dot{V} &= -\frac{D}{m} - g\sin\gamma \\
\dot{\gamma} &= \frac{L\cos\sigma}{mV} - \frac{g\cos\gamma}{V} \\
\dot{\psi} &= \frac{L\sin\sigma}{mV\cos\gamma}
\end{aligned} \tag{3.6}$$

This model has the same singularity as in the 4-DOF models, and it can be dealt with in exactly the same way as before. Thus the equations of motion and continuity conditions for the second phase of the trajectory would be the same as Equations (3.5), but without the states α, β, σ and τ and with α and σ as the controls instead of α_c and σ_c. Note that this simplified model derived here is the same as those used in previous work by Lu et. al. [17].

Chapter 4

Vehicle

The vehicle being considered is a hypersonic aerodynamic vehicle with a reaction control system. The geometry of the vehicle has three major parts - a front cone, a cylinder in the middle, and the frustum of a cone at the rear. The most important feature of this vehicle is that it has high drag, with a maximum L/D of less than 1 [14]. Thus the vehicle loses speed rapidly upon atmospheric re-entry, a feature that will have important implications for the resulting trajectories. The vehicle also has limits on the maximum stagnation point heat rate, and the maximum G-load. Furthermore, the vehicle's control system has response time constraints and angle of attack constraints. These properties are presented in this section.

4.1 Aerodynamics

The aerodynamic characteristics of this vehicle are defined by the coefficient of the normal force (C_N) and the coefficient of the axial force (C_X). Also important is the center of pressure (C_P) which defines the point where the aerodynamic forces act. All three coefficients are defined as follows:

$$\begin{aligned} C_N &= \frac{N}{qS} \\ C_X &= \frac{X}{qS} \\ C_P &= \frac{x_P}{qLS} \end{aligned} \tag{4.1}$$

Where $q = \frac{1}{2}\rho v^2$ is the dynamic pressure, S is the reference area, and L is the reference length. Reference [23] gives the values of S and L for this particular vehicle, and also presents C_X, C_N and C_P as tables, with Mach number M (and thus speed) and angle of attack α as the independent variables. These tables are reproduced below.

Mach / α	0	1.0	5.0	10.0	15.0	30.0
0.0	-1.0663	-1.0663	-1.0532	-1.0120	-0.9950	-1.0900
1.0	-1.0663	-1.0663	-1.0532	-1.0120	-0.9950	-1.0900
1.2	-1.0663	-1.0663	-1.0532	-1.0120	-0.9950	-1.0900
1.5	-1.0663	-1.0663	-1.0532	-1.0120	-0.9950	-1.0900
2.0	-1.0663	-1.0663	-1.0532	-1.0120	-0.9950	-1.0900
3.0	-0.7950	-0.7950	-0.7904	-0.7791	-0.7970	-0.9694
4.0	-0.6803	-0.6803	-0.6795	-0.6811	-0.7135	-0.9694
5.0	-0.5656	-0.5656	-0.5686	-0.5831	-0.6300	-0.9694
8.0	-0.4455	-0.4455	-0.4531	-0.4842	-0.6000	-0.9694
10.0	-0.4095	-0.4095	-0.4185	-0.4552	-0.6000	-0.9694
12.5	-0.3914	-0.3914	-0.4012	-0.4410	-0.6000	-0.9694
15.0	-0.3732	-0.3732	-0.3839	-0.4267	-0.6000	-0.9694
20.0	-0.3634	-0.3634	-0.3748	-0.4211	-0.6000	-0.9694
25.0	-0.3634	-0.3634	-0.3748	-0.4211	-0.6000	-0.9694

Table 4.1: *The axial force coefficient* C_X *as a function of angle of attack and Mach number*

Mach / α	0	1.0	5.0	10.0	15.0	30.0
0.0	0.0	.0837	.4283	.8837	1.5	3.11
1.0	0.0	.0837	.4283	.8837	1.5	3.11
1.2	0.0	.0837	.4283	.8837	1.5	3.11
1.5	0.0	.0837	.4283	.8837	1.5	3.11
2.0	0.0	.0837	.4283	.8837	1.5	3.11
3.0	0.0	.0887	.4510	.9414	1.5	3.11
4.0	0.0	.0882	.4455	.9224	1.5	3.11
5.0	0.0	.0877	.4399	.9034	1.5	3.11
8.0	0.0	.0855	.4247	.8632	1.5	3.11
10.0	0.0	.0846	.4189	.8491	1.5	3.11
12.5	0.0	.0841	.4151	.9409	1.5	3.11
15.0	0.0	.0835	.4113	.8327	1.5	3.11
20.0	0.0	.0830	.4080	.8225	1.5	3.11
25.0	0.0	.0830	.4080	.8225	1.5	3.11

Table 4.2: *The normal force coefficient* C_N *as a function of angle of attack and Mach number*

Mach / α	0	1.0	5.0	10.0	15.0	30.0
0.0	2.396	2.396	2.412	2.249	2.546	2.736
1.0	2.396	2.396	2.412	2.249	2.546	2.736
1.2	2.396	2.396	2.412	2.249	2.546	2.736
1.5	2.396	2.396	2.412	2.249	2.546	2.736
2.0	2.396	2.396	2.412	2.249	2.546	2.736
3.0	2.483	2.483	2.496	2.532	2.679	2.736
4.0	2.508	2.508	2.516	2.550	2.684	2.736
5.0	2.534	2.534	2.536	2.569	2.689	2.736
8.0	2.551	2.551	2.542	2.571	2.689	2.736
10.0	2.551	2.551	2.540	2.569	2.689	2.736
12.5	2.551	2.551	2.537	2.568	2.689	2.736
15.0	2.550	2.550	2.534	2.565	2.689	2.736
20.0	2.550	2.550	2.531	2.559	2.689	2.736
25.0	2.550	2.550	2.531	2.559	2.689	2.736

Table 4.3: *The center of pressure* C_P *as a function of angle of attack and Mach number. The reference length is 18.84 inches, while the length of the vehicle is 80.1 inches*

In order to make computations easier, the aerodynamic tables from [23] are approximated with analytical functions, and some coefficients in the functions are chosen to match the table data. The functions chosen for each coefficient is shown below:

$$\begin{aligned} C_N &= a_N\alpha + b_N v + c_N \\ C_X &= a_X e^{-b_X(v-c_X)} + d_X \\ C_P &= \frac{a_P}{(1+e^{-v/c+b_P})} + c_P \end{aligned} \tag{4.2}$$

The coefficients a_N, b_N, c_N, a_X, b_X, c_X, d_X, a_P, b_P, c_P are all determined by using the method of least-squares to find the best fit to the table data from [23]. c is the speed of sound, approximated as being a constant 330 m/s.

From these coefficients, we can calculate the lift coefficient C_L and the drag coefficient C_D:

$$\begin{aligned} C_L &= -C_X \sin\alpha + C_N \cos\alpha \\ C_D &= C_X \cos\alpha + C_N \sin\alpha \end{aligned} \tag{4.3}$$

Some features of the vehicle are apparent from the functions chosen above - the center of pressure, for instance, is similar to a smoothed Heaviside step function with a "step" at $M = 1$, which is to be expected since the center of pressure moves significantly between subsonic and supersonic flight regimes. Similarly, the axial force coefficient C_X shows a large increase in the transonic region, as one would expect.

Also note that the axial force coefficient does not show much increase as angle of attack increases, but *decreases* with increasing Mach number. This does not mean that the axial force itself is decreasing - but the decrease in C_X is due to the fact that the dynamic pressure q increases quadratically with speed. Thus a decreasing C_X shows that the increase in the axial force is slower than quadratic.

The plots below show the normal force coefficient C_N, the axial force coefficient C_X and the center of pressure C_P as functions of Angle of Attack α and Mach Number M.

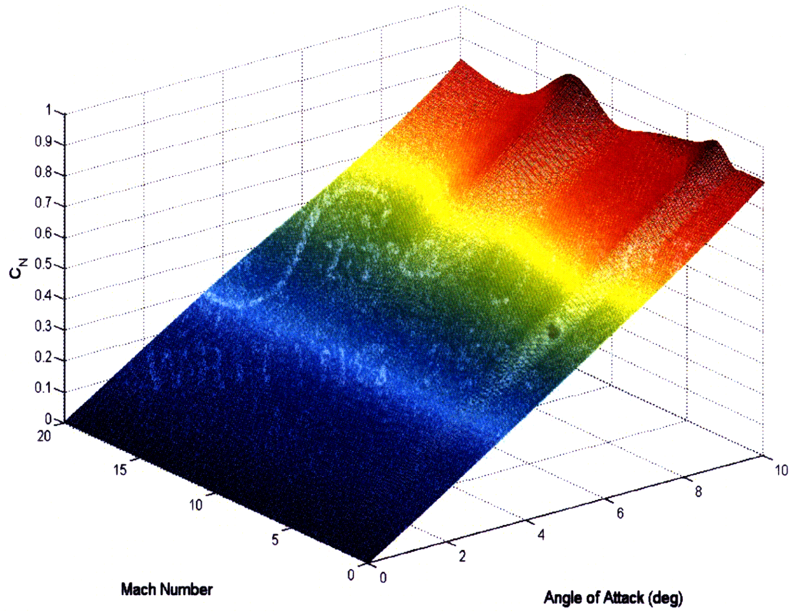

Figure 4-1: *The normal force coefficient as a function of angle of attack and Mach number*

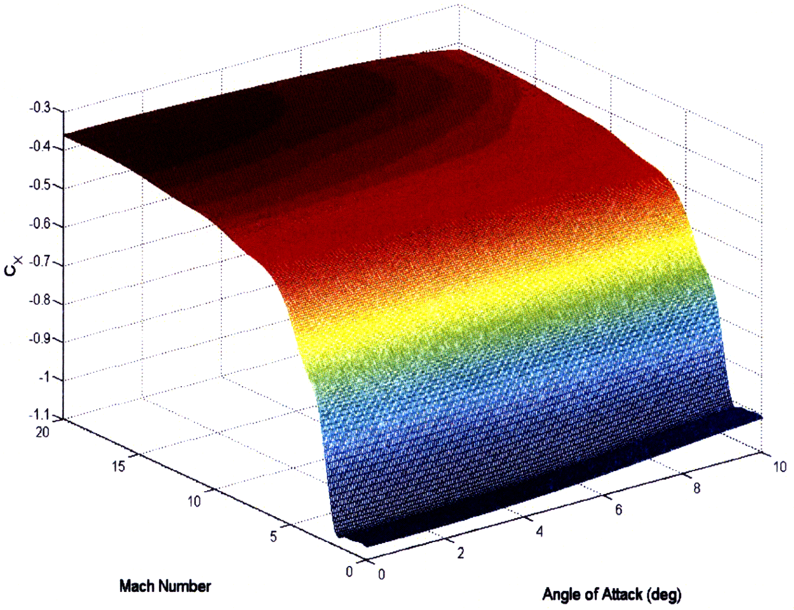

Figure 4-2: *The axial force coefficient as a function of angle of attack and Mach number*

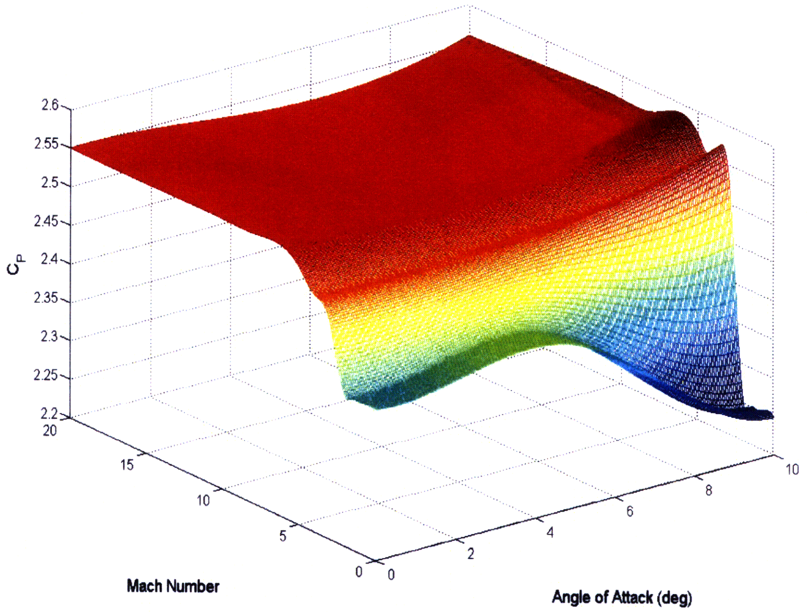

Figure 4-3: *The normalized center of pressure as a function of angle of attack and Mach number*

4.2 Constraints

The primary physical constraints on the vehicle are the stagnation point heat rate, the G-load, the maximum angle of attack and the control system response time.

4.2.1 Stagnation Point Heat Rate

The vehicle cannot sustain an indefinite amount of aerodynamic heating. This is expressed as a constraint on the stagnation point heating rate of the vehicle, $\dot{q}$. The relation between the air density, speed and heat rate is given in [24] as:

$$\dot{q} = 17600 \left(\frac{1}{r_n}\right)^{0.5} \left(\frac{\rho}{\rho_0}\right)^{0.5} \left(\frac{v}{v_c}\right)^{3.15}$$

Where v_c is the speed of a circular orbit at zero altitude (7.9 km/s), r_n is the radius of curvature of the nose, ρ the atmospheric density and ρ_0 the atmospheric density at sea level. This stagnation point heat-rate must be less than the limit, written here as $\dot{q}_{max}$. For this vehicle the limit arbitrarily was chosen to be $\dot{q}_{max} = 23\ Btu/s/ft^2$. The constraint can therefore be written as

$$17600 \left(\frac{1}{r_n}\right)^{0.5} \left(\frac{\rho}{\rho_0}\right)^{0.5} \left(\frac{v}{v_c}\right)^{3.15} < \dot{q}_{max} \tag{4.4}$$

4.2.2 G-Load

The maximum G-load limit that the vehicle can sustain is given as $60g$s. However, an additional safety margin is introduced and the G-load is limited to be $55g$s. The G-load is defined as the total non-gravitational forces acting on the vehicle, in this case the total aerodynamic force $\sqrt{L^2 + D^2}$. Therefore the G-load constraint can be written as

$$\sqrt{L^2 + D^2} < F_{max}$$

Where $F_{max} = 55 \times g \times m$ and m is the mass of the vehicle.

Although in this work we use the total G-loading, it is entirely possible that the different components of the G-load have different constraints. For example, the vehicle might be stronger in the axial direction than in the lateral direction. Therefore it is conceivable that there could be situations in which specific components of the G-load in the body frame can be constrained separately. One of the big advantages of using direct methods to solve optimization problems is the ease with which these new constraints can be added [15].

4.2.3 Angle of Attack

The maximum angle of attack the vehicle can achieve is given by Textron [23] as $\alpha_{max} = 10$ deg. Therefore the constraint on the control as well the actual angle-of-attack (which is a state) can be written as

$$-10\ deg < \alpha_C < 10\ deg$$

$$-10\ deg < \alpha < 10\ deg$$

These limits on the angle of attack could arise from several physical reasons. The first is the stall limit - all aerodynamic surfaces are unable to generate lift beyond a certain angle of attack, and 10 deg could be this limit. Another reason could be because of the limits on the reaction control system. The vehicle is statically stable for most of its flight, so any non-zero angle-of-attack induces a restoring moment to bring the vehicle back to 0 deg. The greater the dynamic pressure of the air flow around the vehicle, the greater this restoring moment. And the greater the angle-of-attack, the greater the restoring moment. To hold the vehicle at a non-zero angle of attack, the vehicle would have to use its reaction control thrusters to compensate for this restoring moment. But the thrust available is limited, and therefore the maximum angle-of-attack the vehicle can be held at is also limited. In general this maximum angle-of-attack is a function of the dynamic pressure, but the model used here simplifies it to a constant.

4.2.4 Response Time

Note that in defining the quadratic lag between the commanded angle of attack α_C and the actual angle of attack α, two parameters were used: ω and ζ. The quadratic lag in the control system from Equations 3.1 are reproduced below:

$$\begin{aligned}
\dot{\alpha} &= \beta \\
\dot{\beta} &= -2\zeta\omega\beta - \omega^2 (\alpha_c - \alpha) \\
\dot{\sigma} &= \tau \\
\dot{\tau} &= -2\zeta\omega\tau - \omega^2 (\sigma_c - \sigma)
\end{aligned}$$

By balancing the moments on the vehicle [23], we can show that

$$\omega^2 = \frac{C_{N\alpha} q_\infty A_b L_{sm}}{I} \tag{4.5}$$

Where $C_{N\alpha}$ is the partial derivative of the normal force coefficient C_N with respect to the angle-of-attack, q_∞ is the dynamic pressure, A_b is the vehicle reference area, L_{sm} is the vehicle static margin, and I the lateral moment of inertia. Note that since we have an aerodynamic model for C_N in Equations (4.2) we can see that $C_{N\alpha} = a_N$. Also, the static margin L_{sm} is given by $L_{sm} = L_{ref}(C_M - C_P)$ where C_P is the center of pressure, C_M is the center of mass, and L_{ref} is the reference length used in defining C_P and C_M. The reference area A_b and the inertia I are given in [14]. For ζ, we use $\zeta = 0.7$ as a realistic value.

THIS PAGE INTENTIONALLY LEFT BLANK

Chapter 5

The Optimal Control Problem

The previous two sections have established the basic dynamics of the re-entry vehicle, and the properties that determine the relation between the controls and the states. Any of the models presented in Equations 3.1, 3.3 and 3.4 can be written in the form

$$\dot{\mathbf{x}} = \mathbf{f}(\mathbf{x}, \mathbf{u}) \tag{5.1}$$

The exact form of $\mathbf{f}$ depends on the model used. For the rotating Earth and spherical Earth models, the states are $\mathbf{x} = [r, \mu, \lambda, v, \gamma, \psi, \alpha, \beta, \sigma, \tau]$ (radius, longitude, latitude, speed, flight path angle, heading angle, angle-of-attack, rate of angle-of-attack, lift direction angle, rate of lift direction angle). For the flat Earth model, the states are $\mathbf{x} = [x, y, z, v, \gamma, \psi, \alpha, \beta, \sigma, \tau]$ (downrange, altitude, crossrange, speed, flight path angle, heading angle, angle-of-attack, rate of angle-of-attack, lift direction angle, rate of lift direction angle). The controls $\mathbf{u}$ are $\mathbf{u} = [\alpha_C, \sigma_C]$ (commanded angle-of-attack and commanded lift direction angle) in the 4-DOF models, and $\mathbf{u} = [\alpha\sigma]$ in the 3-DOF model. The function $\mathbf{f}$ incorporates both the kinematics and the aerodynamic models.

Besides the dynamics as given in Equation 5.1, we have both initial and terminal conditions on the state vector $\mathbf{x}$. The initial conditions are on the position (x, y and z in the flat Earth case, and r, μ and λ in the spherical/rotating Earth cases) and velocity (v, γ and ψ). The terminal conditions are on the angle-of-attack α, the speed v (1300 ft/s in the submunitions case, and 3800 ft/s in the Earth penetrator case) and flight path angle γ (-90 deg in the Earth penetrator case, 0 deg in the submunitions case). Additional constraints on the heading angle and the terminal position will be placed in specific cases that will be discussed later.

We also have path constraints that the vehicle must satisfy at all times. In our case, these are the G-loading and the stagnation point heat rate. In general, we can write these as

$$\mathbf{c}(\mathbf{x}, \mathbf{u}, t) \leq \mathbf{c}_{max}$$

The dynamics and the boundary conditions are not sufficient to determine a unique solution to the control history [25]. To be able to find a unique solution, we introduce a "cost function" J that we minimize while meeting all the boundary conditions and the dynamic conditions. This cost function can be the final downrange distance (which we can maximize or minimize), the final out-of-plane angle, or the control commanded integrated over time.

In general the cost function to be minimized is written as

$$J = h_f(\mathbf{x_f}, t_f) + \int g(\mathbf{x}, \mathbf{u}, t)dt$$

Where $h_f(\mathbf{x_f}, t_f)$ is the part of the cost that depends only on the terminal states (such as final downrange or final out-of-plane angle) and $g(\mathbf{x}, \mathbf{u}, t)$ is the part of the cost that depends on the entire state and control history (such as total commanded control).

Thus the general optimal control problem can be written as

$$minJ = h_f(\mathbf{x_f}, t_f) + \int g(\mathbf{x}, \mathbf{u}, t)dt$$

Subject to the dynamic constraints

$$\dot{\mathbf{x}} = \mathbf{f}(\mathbf{x}, \mathbf{u})$$

And the path constraints

$$\mathbf{c}(\mathbf{x}, \mathbf{u}, t) \leq \mathbf{c}_{max}$$

And the boundary conditions

$$\begin{aligned} \mathbf{x}(\mathbf{t_f}) &= \mathbf{x_f} && (5.2) \\ \mathbf{x}(\mathbf{t_i}) &= \mathbf{x_i} && (5.3) \end{aligned}$$

In optimal control theory, we solve this problem analytically by introducing the co-state vector $\mathbf{p}$, which has the same size as the state vector $\mathbf{x}$, and write the Hamiltonian as

$$H = g + \mathbf{p}^T\mathbf{x}$$

Then we can write the necessary conditions for the optimal solution [25] as

$$\dot{\mathbf{x}} = H_{\mathbf{p}} \tag{5.4}$$

$$-\dot{\mathbf{p}} = H_{\mathbf{x}} \tag{5.5}$$

And the control history $\mathbf{u}(t)$ is given by Pontryagin's Maximum Principle [25]

$$\mathbf{u}(t) = arg\ max_{\mathbf{u}} H \tag{5.6}$$

It can also be shown [25] that in addition to the boundary conditions on the states, the boundary conditions on the co-states are given by

$$p_i(t_f) = \frac{\partial h_t}{\partial x_i}(t_f) \tag{5.7}$$

Where h_t is the terminal cost.

The above condition holds for any costate p_i associated with a state if $x_i(t_f)$ is free (i.e. there is no terminal condition on the state). There is no terminal constraint on the costate if $x_i(t_f)$ is fixed.

In the next two sections, we apply these general results to the re-entry vehicle problem, using the very simple 3-DOF flat Earth model. As we will see, the simple conditions presented above become very complicated when applied to even this simple model.

5.1 Hamiltonian and Necessary Conditions

Applying the first set of necessary conditions (Equation 5.4) to the simplified 3-DOF flat Earth model given in Equations (3.6), we get the following Hamiltonian:

$$\begin{aligned} H &= g(\mathbf{x}, t) + p_1 v \cos\psi \cos\gamma + p_2 v \sin\psi \cos\gamma + p_3 v \sin\gamma - p_4 \tfrac{D}{m} \\ &\quad - p_4 g \sin\gamma + p_5 \tfrac{L\cos\sigma}{mv} - p_5 \tfrac{g\cos\gamma}{v} + p_6 \tfrac{L\sin\sigma}{mv\cos\gamma} \end{aligned} \tag{5.8}$$

Where the costate vector is given by $\mathbf{p} = [p_1\ p_2\ p_3\ p_4\ p_5\ p_6]$. The integrated path cost $g(\mathbf{x}, t)$ also appears in the Hamiltonian. Applying the first set of necessary conditions as in Equation (5.4), we get the system dynamics back:

$$\begin{aligned} \dot{x} &= V\cos\psi\cos\gamma \\ \dot{y} &= V\sin\gamma \\ \dot{z} &= V\sin\psi\cos\gamma \\ \dot{V} &= -\frac{D}{m} - g\sin\gamma \\ \dot{\gamma} &= \frac{L\cos\sigma}{mV} - \frac{g\cos\gamma}{V} \\ \dot{\psi} &= \frac{L\sin\sigma}{mV\cos\gamma} \end{aligned} \tag{5.9}$$

Applying the second set of necessary conditions (Equation 5.5) for the dynamics of the co-states, we get the following set of differential equations:

$$\begin{aligned} \dot{p_1} &= \frac{\partial g}{\partial x} \\ \dot{p_2} &= \frac{\partial g}{\partial y} - p_4 \frac{\partial D/\partial y}{m} + p_5 \frac{\cos\sigma \partial L/\partial y}{mv} + p_6 \frac{\sin\sigma \partial L/\partial y}{mv\cos\gamma} \\ \dot{p_3} &= \frac{\partial g}{\partial z} \end{aligned}$$

$$\begin{aligned}
\dot{p}_4 &= \frac{\partial g}{\partial v} + p_1\cos\psi\cos\gamma + p_2\sin\psi\cos\gamma + p_3\sin\gamma - p_4\frac{\partial D/\partial v}{m}\\
&\quad +p_5\frac{\cos\sigma\partial L/\partial v}{mv} - p_5\frac{L\cos\sigma}{mv^2} + p_5\frac{g\cos\gamma}{v^2} + p_6\frac{\sin\sigma\partial L/\partial v}{mv\cos\gamma}\\
&\quad -p_6\frac{L\sin\sigma}{mv^2\cos\gamma}\\
\dot{p}_5 &= \frac{\partial g}{\partial\gamma} + -p_1 v\cos\psi\sin\gamma - p_2 v\sin\psi\sin\gamma + p_3 v\cos\gamma - p_4 g\cos\gamma\\
&\quad +p_5\frac{g\sin\gamma}{v} + p_6\frac{L\sin\sigma\sec\gamma\tan\gamma}{mv}\\
\dot{p}_6 &= \frac{\partial g}{\partial\psi} - p_1 v\sin\psi\cos\gamma + p_2 v\cos\psi\cos\gamma
\end{aligned} \tag{5.10}$$

Note that there a number of partial derivatives to be evaluated in Equations (5.10). Setting aside the cost function partials, we first compute $\frac{\partial L}{\partial v}$, $\frac{\partial D}{\partial v}$, $\frac{\partial L}{\partial y}$, $\frac{\partial D}{\partial y}$. We evaluate these by first writing

$$\begin{aligned}
L &= \frac{1}{2}\rho v^2 S C_L\\
D &= \frac{1}{2}\rho v^2 S C_D
\end{aligned} \tag{5.11}$$

Equations 5.11 are just the definitions of lift and drag. Next, taking partial derivatives of these Equations with respect to altitude, we get

$$\begin{aligned}
\frac{\partial L}{\partial y} &= \frac{1}{2}\frac{\partial \rho}{\partial y} v^2 S C_L\\
\frac{\partial D}{\partial y} &= \frac{1}{2}\frac{\partial \rho}{\partial y} v^2 S C_D
\end{aligned} \tag{5.12}$$

Taking the partials with respect to the speed, we get

$$\begin{aligned}
\frac{\partial L}{\partial v} &= \frac{1}{2}\rho v^2 S\frac{\partial C_L}{\partial v} + \rho v S C_L\\
\frac{\partial D}{\partial v} &= \frac{1}{2}\rho v^2 S\frac{\partial C_D}{\partial v} + \rho v S C_D
\end{aligned} \tag{5.13}$$

Using the exponential model for the atmosphere, $\rho = \rho_0 e^{-y/H}$ (with $H = 7.1$ km for the Earth [22]), we get for Equations (5.12)

$$\begin{aligned} \frac{\partial L}{\partial y} &= -\frac{1}{2}\frac{1}{H}\rho v^2 S C_L = -\frac{L}{H} \\ \frac{\partial D}{\partial y} &= -\frac{1}{2}\frac{1}{H}\rho v^2 S C_D = -\frac{D}{H} \end{aligned} \tag{5.14}$$

Also, we know that C_L and C_D can be written in terms of C_N and C_X, which in turn are functions of angle of attack α and Mach number M

$$\begin{aligned} C_L &= C_N \cos\alpha - C_X \sin\alpha \\ C_D &= C_N \sin\alpha + C_X \cos\alpha \end{aligned} \tag{5.15}$$

$$\begin{aligned} C_N &= a_N \alpha + b_N v + c_N \\ C_X &= a_X e^{-b_X (v - c_X)} + d_X \end{aligned} \tag{5.16}$$

Using these expressions to compute $\frac{\partial C_L}{\partial v}$ and $\frac{\partial C_D}{\partial v}$ in Equations (5.13),

$$\frac{\partial C_L}{\partial v} = \frac{\partial C_N}{\partial v}\cos\alpha - \frac{\partial C_X}{\partial v}\sin\alpha = b_N \cos\alpha + b_X C_X \sin\alpha$$

$$\frac{\partial C_D}{\partial v} = \frac{\partial C_N}{\partial v}\sin\alpha + \frac{\partial C_X}{\partial v}\cos\alpha = b_N \sin\alpha - b_X C_X \cos\alpha \tag{5.17}$$

Equations (5.17), together with Equations (5.13) give us the expressions for $\frac{\partial L}{\partial v}$ and $\frac{\partial D}{\partial v}$.

5.2 The Maximum Principle and the Controls

Next, we have to determine the control to be applied as a function of the states and co-states, as derived using Pontryagin's Maximum Principle in Equation (5.6). To do this, we first have the write the Hamiltonian in a form that makes the controls α and σ explicit. From looking the Hamiltonian in Equation (5.8) we see that H is already explicitly written as a function of σ. We can make this more explicit by rewriting H as

$$H = \mathbb{B}_1 + \mathbb{B}_2 \sin\sigma + \mathbb{B}_3 \cos\sigma + g(\mathbf{x}, \alpha, \sigma, t) \tag{5.18}$$

$$\begin{aligned}
\mathbb{B}_1 &= p_1 v \cos\psi \cos\gamma + p_2 v \sin\psi \cos\gamma + p_3 v \sin\gamma - \frac{p_4 D}{m} - p_4 g \sin\gamma - \frac{p_5 g \cos\gamma}{v} \\
\mathbb{B}_2 &= \frac{p_6 L}{m v \cos\gamma} \\
\mathbb{B}_3 &= \frac{p_5 L}{m v}
\end{aligned}$$

In Equation 2.3, we have made the dependence of g on α and σ explicit. Thus exact form of H as a function of σ depends on the specific path cost function $g(\mathbf{x}, \alpha, \sigma, t)$ being considered.

Next we have to write H as an explicit function of α. Using Equations (5.16) in Equations (5.15), we get

$$\begin{aligned}
C_L &= (a_N \alpha + b_N v + c_N) \cos\alpha - (a_X e^{-b_X(v - c_X)} + d_X) \sin\alpha \\
C_D &= (a_N \alpha + b_N v + c_N) \sin\alpha + (a_X e^{-b_X(v - c_X)} + d_X) \cos\alpha
\end{aligned} \tag{5.19}$$

Using Equations (5.19) in Equations (5.11), together with the assumption that atmospheric density is an exponential function of altitude $\rho = \rho_0 e^{-y/H}$, we get

$$\begin{aligned}
L &= \frac{1}{2}\rho_0 e^{-y/H} v^2 S(a_N\alpha + b_N v + c_N)\cos\alpha - \frac{1}{2}\rho_0 e^{-y/H} v^2 S(a_X e^{-b_X(v-c_X)} + d_X)\sin\alpha \\
D &= \frac{1}{2}\rho_0 e^{-y/H} v^2 S(a_N\alpha + b_N v + c_N)\sin\alpha + \frac{1}{2}\rho_0 e^{-y/H} v^2 S(a_X e^{-b_X(v-c_X)} + d_X)\cos\alpha
\end{aligned}$$

Rewriting the above expressions we get

$$\begin{aligned}
L &= \left(\tfrac{1}{2}\rho_0 e^{-y/H} v^2 S a_N\right)\alpha\cos\alpha + \left(\tfrac{1}{2}\rho_0 e^{-y/H} v^3 S b_N + \tfrac{1}{2}\rho_0 e^{-y/H} v^2 S c_N\right)\cos\alpha \\
&+ \left(-\tfrac{1}{2}\rho_0 e^{-y/H} v^2 S a_X e^{-b_X(v-c_X)} - \tfrac{1}{2}\rho_0 e^{-y/H} v^2 S d_X\right)\sin\alpha
\end{aligned}$$

$$\begin{aligned}
D &= \left(\tfrac{1}{2}\rho_0 e^{-y/H} v^2 S a_N\right)\alpha\sin\alpha + \left(\tfrac{1}{2}\rho_0 e^{-y/H} v^3 S b_N + \tfrac{1}{2}\rho_0 e^{-y/H} v^2 S c_N\right)\sin\alpha \\
&+ \left(\tfrac{1}{2}\rho_0 e^{-y/H} v^2 S a_X e^{-b_X(v-c_X)} + \tfrac{1}{2}\rho_0 e^{-y/H} v^2 S d_X\right)\cos\alpha
\end{aligned}$$

We simplify the above by defining

$$\begin{aligned}
C_1 &= \frac{1}{2}\rho_0 e^{-y/H} v^2 S a_N \\
C_2 &= \frac{1}{2}\rho_0 e^{-y/H} v^3 S b_N + \frac{1}{2}\rho_0 e^{-y/H} v^2 S c_N \\
C_3 &= \frac{1}{2}\rho_0 v^2 S a_X e^{-b_X(v-c_X)} + \frac{1}{2}\rho_0 e^{-y/H} v^2 S d_X
\end{aligned}$$

In terms of these new quantities, we can write L and D as

$$\begin{aligned}
L &= C_1\alpha\cos\alpha + C_2\cos\alpha - C_3\sin\alpha \\
D &= C_1\alpha\sin\alpha + C_2\sin\alpha + C_3\cos\alpha
\end{aligned}$$

Using these expressions for L and D in Equation (5.8) for H, we get the the Hamiltonian as an explicit function of α

$$H = \mathbb{C}_1 + \mathbb{C}_2\alpha\cos\alpha + \mathbb{C}_3\alpha\sin\alpha + \mathbb{C}_4\cos\alpha + \mathbb{C}_5\sin\alpha + g(\mathbf{x}, \alpha, \sigma, t) \tag{5.20}$$

$$\begin{aligned}
\mathbb{C}_1 &= p_1 v\cos\psi\cos\gamma + p_2 v\sin\psi\cos\gamma + p_3 v\sin\gamma - p_4 g\sin\gamma - p_5 g\frac{\cos\gamma}{v} \\
\mathbb{C}_2 &= C_1\frac{p_5\cos\sigma}{mv} + C_1\frac{p_6\sin\sigma}{mv\cos\gamma} \\
\mathbb{C}_3 &= -C_1\frac{p_4}{m} \\
\mathbb{C}_4 &= \left(\frac{C_2 p_5\cos\sigma}{mv} + \frac{C_2 p_6\sin\sigma}{mv\cos\gamma} - \frac{C_3 p_4}{m}\right) \\
\mathbb{C}_5 &= -C_2\frac{p_4}{m} - C_3\frac{p_5\cos\sigma}{mv} - C_3\frac{p_6\sin\sigma}{mv\cos\gamma} \\
C_1 &= \frac{1}{2}\rho_0 e^{-y/H}v^2 S a_N \\
C_2 &= \frac{1}{2}\rho_0 e^{-y/H}v^3 S b_N + \frac{1}{2}\rho_0 e^{-y/H}v^2 S c_N \\
C_3 &= \frac{1}{2}\rho_0 e^{-y/H}v^2 S a_X e^{-b_X(v-c_X)} + \frac{1}{2}\rho_0 e^{-y/H}v^2 S d_X
\end{aligned}$$

Again, Equation 5.20 shows that H depends on the specific path cost function $g(\mathbf{x}, \alpha, \sigma, t)$.

5.3 Solution Methods

In the two sections above, we have seen the Equations that need to be solved for the re-entry problem. The system given by Equations 5.9 and 5.10 needs to be solved with the controls given by minimizing Equations 5.18 and 5.20 respectively. Clearly, the system is extremely complicated with boundary conditions at both the initial and terminal times. An analytical solution in this case is not possible. A numerical solution to the system of Equations 5.9 and 5.10 involves solving a boundary-value problem that has 12 variables - twice the original system. Such methods are called "Indirect Methods" [18]. Since solving boundary-value problems is well-understood, we first show that it is possible to numerically solve Equations 5.9 and 5.10 given boundary conditions. Then, we will turn to "Direct Methods" which are much simpler to implement, especially with highly constrained systems.

5.3.1 Indirect Method

The problem we first solve is the simplest one - an Earth Penetrator trajectory with a flat Earth model with no out-of-plane maneuvers, i.e. lift direction angle $\sigma = 0$ and heading angle $\psi = 0$ at all times. This implies that the crossrange $z = 0$ at all times. Similarly, the co-states associated with z and ψ, p_3 and p_6 respectively, can be set to zero. Thus the model given in Equations 5.9 and 5.10 simplifies further, with essentially four states and four co-states. The initial conditions are chosen to be $x_i = 0$ km, $y_i = 100$ km, $v_i = 23000$ ft/s, $\gamma_i = -13$ deg. The terminal conditions are $y_f = 0$ km, $v_f = 3800$ ft/s, $\gamma_f = -80$ deg. For the sake of simplicity, we set the terminal time to be fixed at 66 seconds. The terminal angle-of-attack α_f is unconstrained. For this problem, the cost will be defined as

$$J = \int_0^{t_f} \alpha^2 dt$$

Using $g(\mathbf{x}, \alpha, \sigma, t) = \alpha^2$ in Equation 5.20, we see that the Hamiltonian is

$$H = \mathbb{C}_1 + \mathbb{C}_2 \alpha \cos\alpha + \mathbb{C}_3 \alpha \sin\alpha + \mathbb{C}_4 \cos\alpha + \mathbb{C}_5 \sin\alpha + \alpha^2 \tag{5.21}$$

Where $\mathbb{C}_1, \mathbb{C}_2, \mathbb{C}_3, \mathbb{C}_4, \mathbb{C}_5$ are all as given in Equation 5.20. The control α at any time is that value of α which minimizes H.

Using the fact that $z = 0$, $\psi = 0$, $\sigma = 0$, $p_3 = 0$ and $p_6 = 0$, Equations 5.9 for the states becomes

$$\begin{aligned} \dot{x} &= V\cos\gamma \\ \dot{y} &= V\sin\gamma \\ \dot{V} &= -\frac{D}{m} - g\sin\gamma \\ \dot{\gamma} &= \frac{L}{mV} - \frac{g\cos\gamma}{V} \end{aligned} \tag{5.22}$$

And Equations 5.10 for the co-states become

$$\begin{aligned}
\dot{p}_1 &= 0 \\
\dot{p}_2 &= -p_4\frac{\partial D/\partial y}{m} + p_5\frac{\cos\sigma\partial L/\partial y}{mv} \\
\dot{p}_4 &= p_1\cos\psi\cos\gamma + p_2\sin\psi\cos\gamma - p_4\frac{\partial D/\partial v}{m} \\
&+p_5\frac{\cos\sigma\partial L/\partial v}{mv} - p_5\frac{L\cos\sigma}{mv^2} + p_5\frac{g\cos\gamma}{v^2} \\
\dot{p}_5 &= -p_1 v\cos\psi\sin\gamma - p_2 v\sin\psi\sin\gamma - p_4 g\cos\gamma \\
&+p_5\frac{g\sin\gamma}{v}
\end{aligned} \tag{5.23}$$

Where α is given by

$$\alpha = argmin\left(\mathbb{C}_1 + \mathbb{C}_2\alpha\cos\alpha + \mathbb{C}_3\alpha\sin\alpha + \mathbb{C}_4\cos\alpha + \mathbb{C}_5\sin\alpha + \alpha^2\right) \tag{5.24}$$

Since the system shown above has 8 states $(x, y, z, v, \gamma, p_1, p_2, p_3, p_4)$, 8 boundary conditions are needed to find a unique solution. These boundary conditions are

$$\begin{aligned}
x_i &= 0 \\
y_i &= 100km \\
v_i &= 23000ft/s \\
\gamma_i &= -13deg \\
p_{1f} &= 0 \\
y_f &= 0km \\
v_f &= 3800ft/s \\
\gamma_f &= -80deg
\end{aligned} \tag{5.25}$$

Equations 5.22, 5.23, 5.24, 5.25 together provide a complete set of differential equations and boundary conditions that can now be solved numerically.

The variables in the problem have very different orders of magnitude - for instance, the downrange is of the order of several hundreds of kilometers (of order 10^5 meters) while the speed is of the order of thousands of meters per second (of order 10^3 m/s) and the flight path angle is of the order of radians (of order 10^0 radians). Since such large variations in the orders of magnitude tend to greatly increase the computation time (or maybe even make the problem numerically infeasible [15]), standard SI units are *not* used. Instead, all the variables are scaled to roughly be of order 1. The length scale for the problem is chosen to be 400 km and the time scale 60 seconds. The speeds are therefore scaled to be of order 400000/60 m/s = 6666.67 m/s. Angles are not scaled, since angles measured in radians are already of order 1.

Another issue to be considered is the solving for α in Equation 5.24. The most obvious way to solve for α is to take the derivative and set it to zero. However, we find that when this is done, getting α requires solving a transcendental equation. Since this cannot be done analytically, we must either use a numerical minimization method or an approximate method. Here, we first choose to use an approximate method. At each time step, a quadratic polynomial is fit to the Hamiltonian. The minimum of this quadratic polynomial is then easily computed and used as the control at that time step. While this is an approximation, it will be shown later that the approximation is very good.

With this scaling and controls, we solve the system of differential equations with boundary conditions using the MATLAB utility `bvp4c`, which solves boundary-value problems using a collocation technique. The solution for the states and co-states *in scaled variables* is shown below in Figures 5-1 and 5-2. De-scaling the variables and plotting the altitude and downrange, we see the shape of the trajectory in Figure 5-3. The trajectory shows that the vehicle lofts itself to stay at high altitudes (and therefore not lose too much speed), and then turns towards the ground to reach its terminal flight path angle constraint. These features will be discussed in detail later - here we only wish to illustrate the Indirect Method for solving the optimal control problem.

Finally, in Figure 5-4 we compare the Hamiltonian to its quadratic approximation using the states at one point in the trajectory. At the time step shown, the actual minimum is at $\alpha = 6.41$ deg while the minimum for the quadratic approximation is at $\alpha = 6.47$ deg. The difference is small, but not negligible. When a numerical minimization method is used to find, α run times increase from about 5 seconds (for the quadratic approximation) to several hours. Thus the quadratic approximation has significant error, but trying to find the actual minimum greatly increases the computational power required. Furthermore, if additional controls were added (such as σ for instance) and additional states added (for out-of-plane motion or for control system delays), the size of the system of differential equations rapidly grows. As seen before, the full system has 16 states and co-states and 2 control variables. When the rotation and curvature of the Earth are added, the dynamics become more complex. In addition, it was found while solving the problem that Indirect Methods are very sensitive to the initial guess provided to the boundary-value problem solver [18]. With a bad initial guess, the solver might not find a solution even if one exists. Furthermore, no path constraints have been considered here. As these important features are added, the computational power required by Indirect Methods grows very quickly. For this reason, previous work in this area ([4], [5], [1], [2]) has focused on using Direct Methods.

A more common approach, Direct Methods evaluate the differential equations for the dynamics at discrete node points in time and connect the nodes with a parameterized function. The problem then becomes a non-linear programming problem that can be solved using non-linear programming software such as SNOPT. DIDO is a software tool that uses globally orthogonal Legendre Polynomials to represent the dynamics of the system at the node points. The method implemented in DIDO is known as the Legendre Pseudospectral Method, and next we will solve the same problem using DIDO and compare the results and computational performance with the Indirect Method presented here.

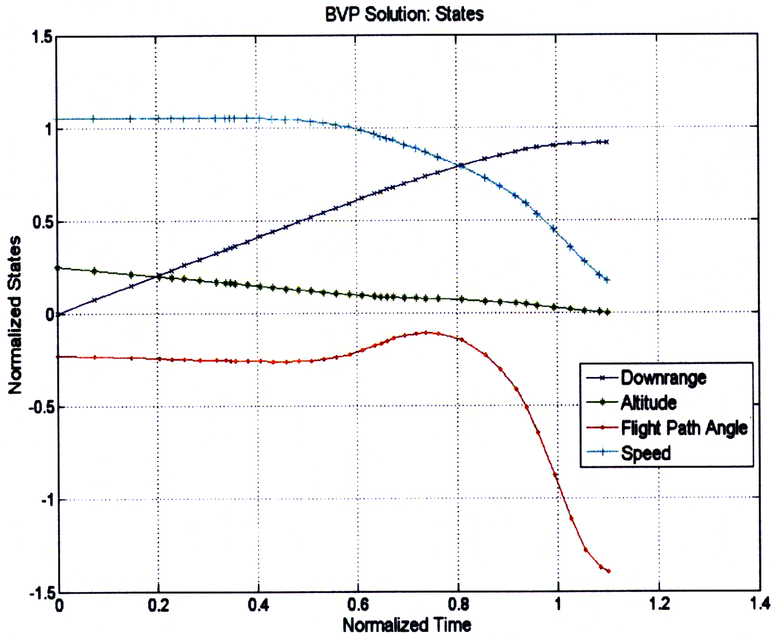

Figure 5-1: *The solution to the boundary-value problem showing the scaled states*

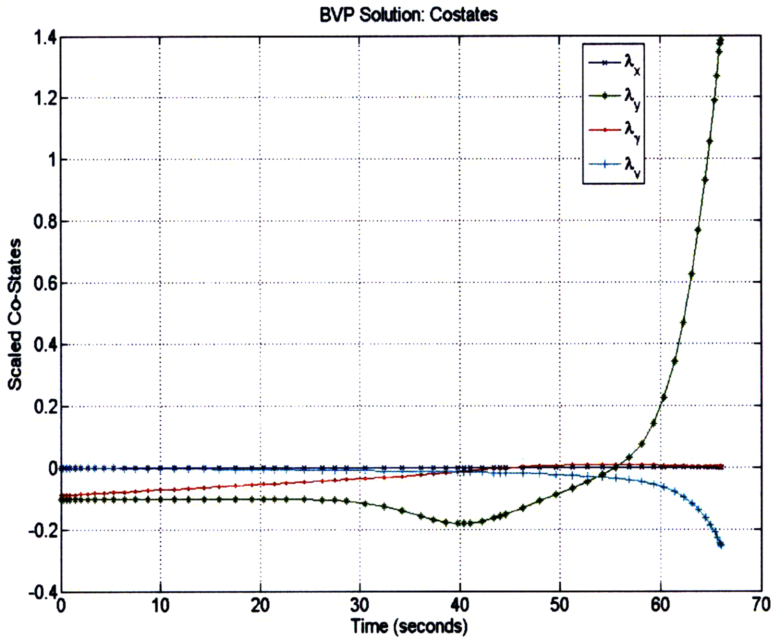

Figure 5-2: *The solution to the boundary-value problem showing the scaled co-states*

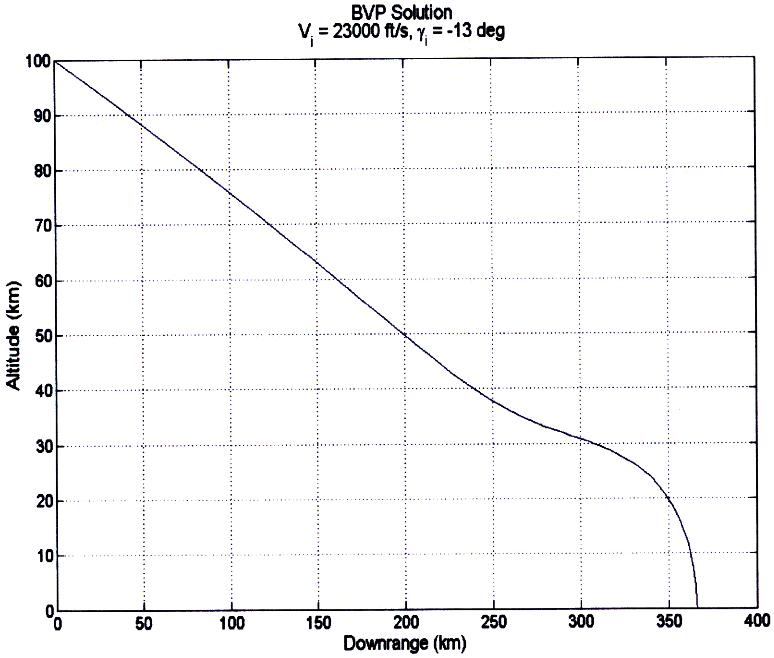

Figure 5-3: *The trajectory obtained by solving the boundary-value problem*

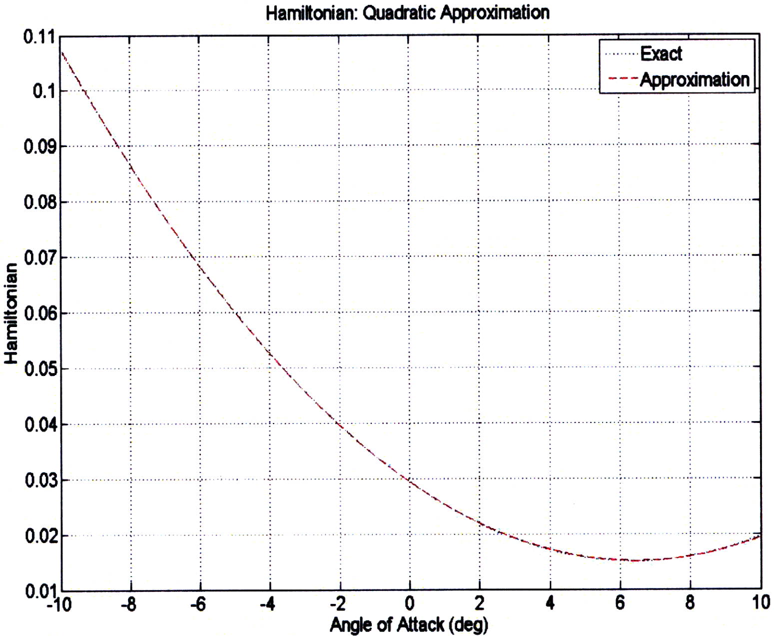

Figure 5-4: *The Hamiltonian and its quadratic approximation*

5.3.2 Direct Methods

Solving the same problem described previously using DIDO, we get the trajectory shown in Figure 5-5. Clearly, there is some difference between the solution obtained by each of the methods. This is most likely due to the quadratic approximation used in the Indirect method. This is seen more clearly in Figure 5-6, which shows that the controls are different in each of the cases. This quadratic approximation also results in differences in the co-states, as Figure 5-7 shows in the case of the altitude co-state. The same is true for the other co-states. The corresponding altitude states as shown in Figure 5-8 are very close, despite the quadratic approximation. Figure 5-9 shows the Hamiltonian as it varies with time and α throughout the computed trajectory. The behavior of the Hamiltonian is complex, and thus the simplified quadratic approximation has a significant impact on the computed controls.

The computation times required for each of the methods shows that Indirect Methods, even with the quadratic approximation to the Hamiltonian, take longer than Direct Methods. As mentioned previously, when the controls were computed using MATLAB's function minimization utility `fmincon`, run-times were greatly increased. Furthermore, adding additional features such as free terminal time, path constraints, and additional states for the control system delays are very straightforward with Direct Methods [20] and in particular DIDO [15]. Furthermore, Direct Methods do not require an initial guesses for the co-states, which are typically hard to obtain but are necessary for Indirect Methods. And finally, Direct Methods are much less sensitive to initial guesses than Indirect Methods [18]. For these reasons, Direct Methods as implemented in DIDO will be used in this work.

An additional advantage of using Direct Methods is that in the computation of the landing footprint, various types of path and terminal cost functions will be used - for instance, minimum control, maximum downrange, maximum out-of-plane angle, and minimum uprange. If Indirect Methods were used, each of these cost functions would generate a different Hamiltonian and a different set of terminal constraints on the states and co-states. For this reason, it is particularly desirable to use Direct Methods and DIDO in particular, which makes the process of using different cost functions very straightforward [15].

Next we will look at the different cost functions that will be used in computing the landing footprint.

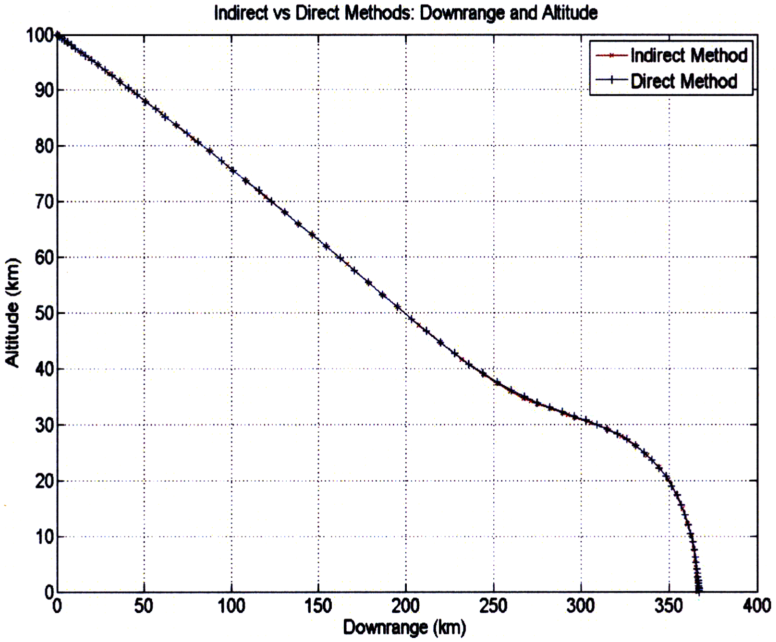

Figure 5-5: *Comparison of trajectories generated by the Indirect and Direct Methods*

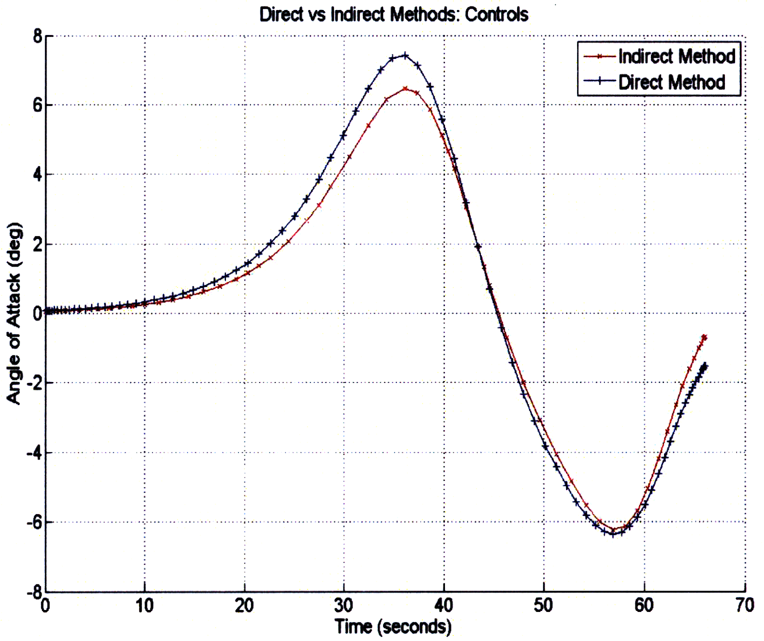

Figure 5-6: *Comparison of controls generated by the Indirect and Direct Methods*

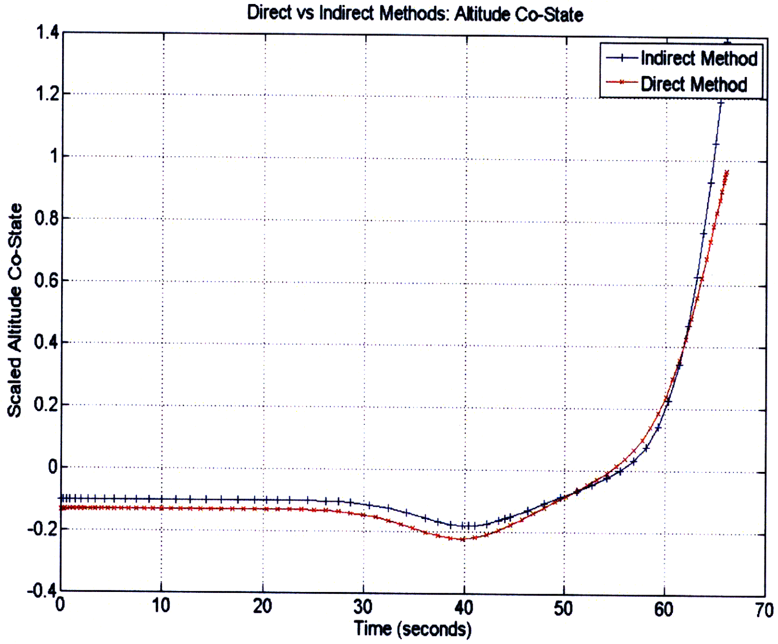

Figure 5-7: *Comparison of the altitude co-state generated by the Indirect and Direct Methods*

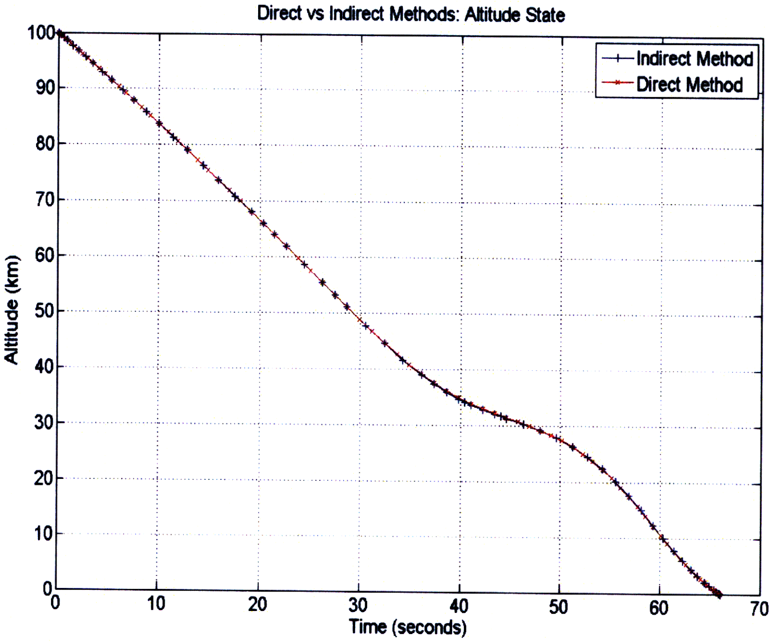

Figure 5-8: *Comparison of the altitude state generated by the Indirect and Direct Methods*

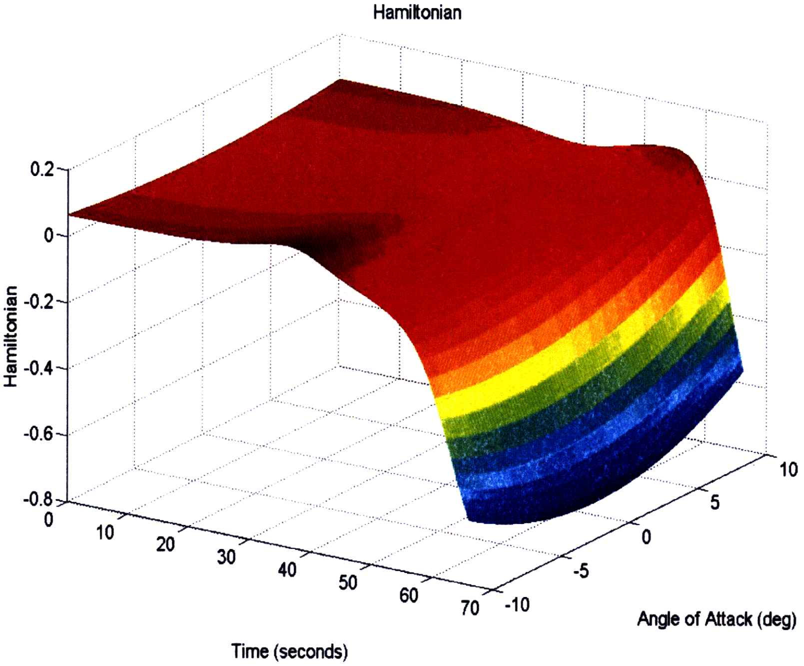

Figure 5-9: *The Hamiltonian along the optimal trajectory, as a function of angle-of-attack* α *at every time instant*

5.4 Footprint Computation: Flat Earth

The computation of the landing footprint of the vehicle involves computing the maximum downrange, the minimum uprange, and the maximum out-of-plane angle, as shown in Figure (1.2). All three of these parameters are functions of the terminal states, and these are presented here.

5.4.1 Distance

In the flat Earth case, the distance traveled is given by

$$d = \sqrt{x_f^2 + z_f^2}$$

By maximizing d, we get the maximum downrange, and by minimizing d we get the minimum uprange.

5.4.2 Maximum Out-of-Plane Angle

As we have seen before, the out-of-plane angle is given by

$$\Theta = \tan^{-1} \frac{z_f - z_0}{x_f - x_0} \tag{5.26}$$

To get the maximum out-of-plane angle, we maximize Θ.

In order to "fill in" the rest of the footprint that lies between the maximum downrange and the maximum out-of-plane angle, as well as the minimum uprange and the maximum out-of-plane angle, we need some intermediate points. We obtain these by constraining the trajectories such that their terminal point must lie at a specified out-of-plane angle, and then maximize downrange and minimize uprange. As this angle is varied from 0 to the maximum out-of-plane angle, the intermediate values are filled in. This is shown in Figure (5-10) below.

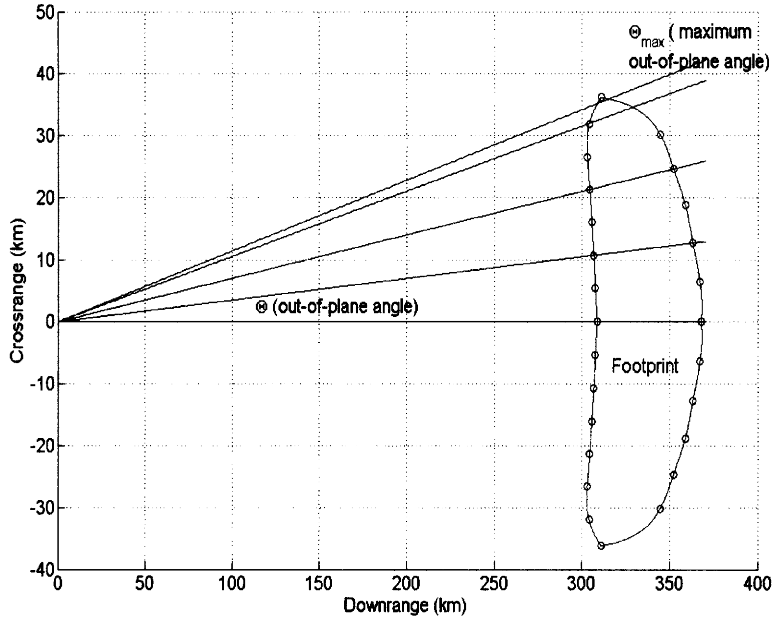

Figure 5-10: *A footprint as viewed from above: by constraining the terminal point to lie along one particular out-of-plane angle, and then finding the maximum-downrange trajectory and minimum-uprange trajectory, we can sweep out the entire landing footprint*

5.4.3 Terminal Angle Constraint

In order to sweep out a footprint, we need to constrain the terminal position of the trajectories to lie along the radial lines shown in Figure 5-10. The angle associated with each of the radial lines is clearly

$$\Theta = \tan^{-1} \frac{z_f - z_0}{x_f - x_0}$$

Therefore the constraint on the final position, given a targeted out-of-plane angle of Θ, can simply be expressed as

$$(z_f - z_0) - (x_f - x_0) \tan \Theta = 0 \tag{5.27}$$

5.5 Footprint Computation: Spherical Earth

The basic method by which a footprint is traced out remains the same in the spherical Earth formulation. However, the distance traveled must now be measured on the surface of the sphere, along a Great Circle. The out-of-plane angle traveled, which was a simple tan relation between the net downrange and net crossrange (Equation (5.26)) is now a much more complicated relation between the initial latitude and longitude and the final latitude and longitude. Similarly, the out-of-plane angle constraint is a more complex function of the initial and final latitudes and longitudes, instead of the simple relation between initial and final down- and crossranges presented in Equation (5.27). These relations are derived and presented in this section.

5.5.1 Maximum Downrange

The computation of distance in the spherical Earth case is now the distance along a Great Circle. The length of a line segment along a Great Circle of a sphere is given by the simple relation

$$d = R\Theta \tag{5.28}$$

Where Θ is the angle subtended at the center of the sphere by the line segment. Since the line segment is on a Great Circle, its length can simply be written as a function of the latitude and longitude at the terminal points of the segment. We do this by first expressing the terminal points of the segment in Cartesian coordinates

$$\begin{aligned}
\mathbf{r_i} &= R\cos\lambda_i\cos\mu_i\mathbf{i} + R\cos\lambda_i\sin\mu_i\mathbf{j} + R\sin\lambda_i\mathbf{k} \\
\mathbf{r_f} &= R\cos\lambda_f\cos\mu_f\mathbf{i} + R\cos\lambda_f\sin\mu_f\mathbf{j} + R\sin\lambda_f\mathbf{k}
\end{aligned}$$

Since $\mathbf{r_i}$ and $\mathbf{r_f}$ both originate at the center of the Earth, the angle between them will lie in a plane that passes through the center of the Earth, which by definition is Θ. Therefore we get Θ from

$$\begin{aligned}
\mathbf{r_i}.\mathbf{r_f} &= |\mathbf{r_i}||\mathbf{r_f}|\cos\Theta \\
\mathbf{r_i}.\mathbf{r_f} &= R^2\left(\cos\lambda_i\cos\lambda_f\cos(\mu_i-\mu_f)+\sin\lambda_i\sin\lambda_f\right) \\
|\mathbf{r_i}||\mathbf{r_f}|\cos\Theta &= R^2\cos\Theta
\end{aligned}$$

Therefore the distance in Equation (5.28) is

$$d = R\cos^{-1}(\cos\lambda_i\cos\lambda_f\cos(\mu_i-\mu_f)+\sin\lambda_i\sin\lambda_f) \tag{5.29}$$

For maximum downrange, we maximize d and for minimum uprange, we minimize d.

5.5.2 Maximum Out-of-Plane

The out-of-plane angle traveled is obtained by recognizing that the lines of constant out-of-plane angle (as shown in Figure 5-10) are now Great Circles that pass through the initial point. (see Figure 5-11).

The equation for a Great Circle is given by the intersection between a plane passing through the origin and the sphere. If the plane is given by

$$ax + by + cz = 0$$

Given the parametric equations of the sphere,

$$\begin{aligned}
x &= R\cos\lambda\cos\mu \\
y &= R\cos\lambda\sin\mu \\
z &= R\sin\lambda
\end{aligned}$$

The equation of a Great Circle is therefore

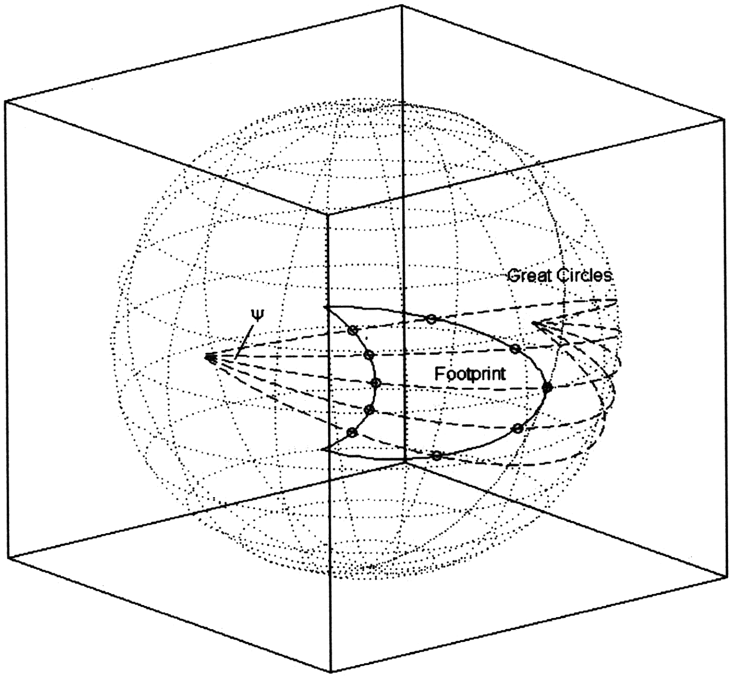

Figure 5-11: *The minimum and maximum distance (shown as black circles) along all the Great Circles passing through the initial point determine the footprint in a spherical Earth model*

$$a \cos\lambda \cos\mu + b \cos\lambda \sin\mu + c \sin\lambda = 0$$

We now need to find the coefficients a, b and c for the planes in which the Great Circles lie. These are the components of the normal vector of the plane. This normal vector must be calculated using

$$\mathbf{n} = \mathbf{r} \times \mathbf{t}$$

$\mathbf{r}$ is the radial vector from the center of the sphere to the surface, while $\mathbf{t}$ is the vector tangent to the Great Circle. These vectors are shown in Figure 5-12 below.

If we take the initial position (through which the plane must pass) as μ_0 and λ_0, we see that the parametric equations for all vectors tangent to Great Circles that pass through this initial latitude and longitude are

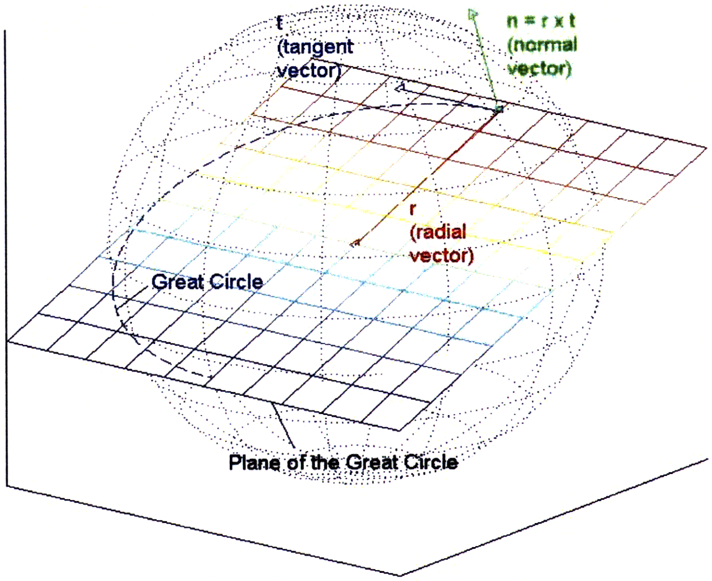

Figure 5-12: *The definition of the* $\mathbf{r}, \mathbf{t}, \mathbf{n}$ *vectors*

$$\mathbf{t} = (-\sin\lambda_0 \sin\mu_0 \sin\Theta + \cos\mu_0 \cos\Theta)\,\mathbf{j} + (-\sin\lambda_0 \cos\mu_0 \sin\Theta - \sin\mu_0 \cos\Theta)\,\mathbf{i} + \cos\lambda_0 \sin\Theta\mathbf{k}$$

By varying the angle Θ, we can get all possible Great Circles that pass through μ_0 and λ_0. Next, we see that the radial vector is given by

$$\mathbf{r} = \cos\lambda_0 \cos\mu_0\mathbf{i} + \cos\lambda_0 \sin\mu_0\mathbf{j} + \sin\lambda_0\mathbf{k}$$

$$\mathbf{r}\times\mathbf{t} = \mathbf{n} = -\cos\lambda_0 \cos\Theta\mathbf{k} + (\cos\mu_0 \sin\Theta + \sin\lambda_0 \sin\mu_0 \cos\Theta)\,\mathbf{j} + (-\sin\mu_0 \sin\Theta + \sin\lambda_0 \cos\mu_0 \cos\Theta)\,\mathbf{i}$$

Thus the equation of the Great Circle that passes through μ_0 and λ_0, and making an angle Θ with the local latitude is given by

$$a\cos\lambda\cos\mu + b\cos\lambda\sin\mu + c\sin\lambda = 0 \tag{5.30}$$

$$\begin{aligned} a &= -\sin\mu_0 \sin\Theta + \sin\lambda_0 \cos\mu_0 \cos\Theta \\ b &= \cos\mu_0 \sin\Theta + \sin\lambda_0 \sin\mu_0 \cos\Theta \\ c &= -\cos\lambda_0 \cos\Theta \end{aligned}$$

Solving the equation above for Θ, we get

$$\tan\Theta = \frac{\sin\lambda_0 \cos(\mu_0 - \mu) - \cos\lambda_0 \tan\lambda}{\sin(\mu_0 - \mu)} \tag{5.31}$$

To get the maximum out-of-plane angle, we have to maximize Θ.

5.5.3 Terminal Angle Constraint

The spherical Earth equivalent of the out-of-plane angle constraint given in Equation (5.27) is the constraint that the terminal latitude and longitude must lie on a Great Circle with a specific value of Θ. Therefore, to enforce this constraint, we would have to constrain the final latitude λ_f and the final longitude μ_f to be

$$a\cos\lambda_f \cos\mu_f + b\cos\lambda_f \sin\mu_f + c\sin\lambda_f = 0 \tag{5.32}$$

$$\begin{aligned} a &= -\sin\mu_0 \sin\Theta + \sin\lambda_0 \cos\mu_0 \cos\Theta \\ b &= \cos\mu_0 \sin\Theta + \sin\lambda_0 \sin\mu_0 \cos\Theta \\ c &= -\cos\lambda_0 \cos\Theta \end{aligned}$$

Chapter 6

Earth Penetrator

In this chapter, we begin looking at trajectories that satisfy the Earth penetrator mission with the vehicle models presented previously. We begin by looking at the 3-DOF flat Earth model, i.e. the simplest of model. We choose this model because it is computationally the least complex. We will also show later that although the curvature of the Earth and its rotation are both important, the nature of the trajectories and the basic behavior of the vehicle is captured well by the flat Earth model. Also, the time delays in the control system are very small (of the order of 0.017 s) and so there is no great loss of accuracy in using 3-DOF model instead of the 4-DOF model. Finally, DIDO like all direct methods requires an initial guess. First solving the simplified problem, and using that as an initial guess to solve the more complete problem improves total computational time significantly. For all these reasons, we begin by solving for trajectories in the 3-DOF model. The effects that were all ignored (curvature of the Earth, rotation of the Earth, the time delays) are re-introduced later.

We begin by analyzing the ballistic trajectory, and show the necessity of a maneuverable re-entry vehicle to be able to achieve the vehicle's missions. We then look at the vehicle's capabilities and the characteristics of its trajectories in accomplishing an Earth penetrator mission.

6.1 The Ballistic Trajectory

For the ballistic trajectory, all control inputs are 0. Thus, in the equations of motion reduce to

$$\begin{aligned}
\dot{x} &= V \cos\psi \cos\gamma \\
\dot{y} &= V \sin\psi \cos\gamma \\
\dot{z} &= V \sin\gamma \\
\dot{V} &= -\frac{D}{m} - g\sin\gamma \\
\dot{\gamma} &= -\frac{g\cos\gamma}{V} \\
\dot{\psi} &= 0
\end{aligned}$$

The equations are propagated using the initial conditions $x_i = 0$, $y_i = 100$ km, $z_i = 0$, $V_i = 23000$ ft/s, $\gamma_i = -13$ deg, $\psi_i = 0$. The resulting trajectory is shown below.

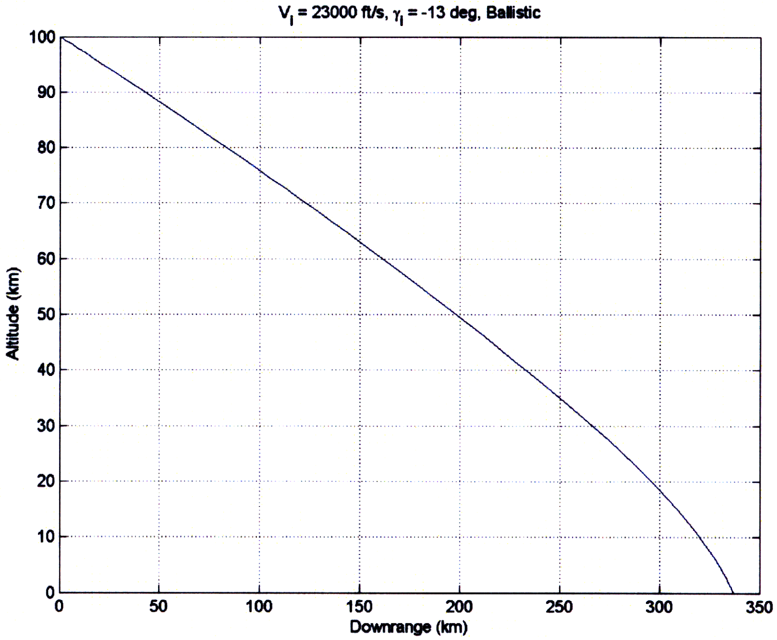

Figure 6-1: *The altitude as a function of downrange for initial conditions* $V_i = 23000$ *ft/s,* $\gamma_i = -13$ *degrees,* $\beta_i = 0$ *with no control applied*

Clearly, the ballistic trajectory does not satisfy any of the terminal conditions, either for the Earth Penetrator mission or the Submunitions mission. The terminal speed is under 500 m/s, which is much too slow for the Earth Penetrator mission (which needs a terminal speed of 1160 m/s) and too fast for the Submunitions mission (which requires a terminal speed of 390 m/s). Also, the terminal γ is -42 deg, which is too steep for the Submunitions mission (which requires a $\gamma = 0$) and too shallow for the Earth penetrator ($\gamma = -90$ deg). This shows the need for a maneuvering re-entry vehicle. However, the ballistic trajectory gives a rough measure of the downrange distances that can be expected, which is about 300 km. As we will see later, this is indeed the case for the Earth Penetrator mission, while the Submunitions mission can go much farther.

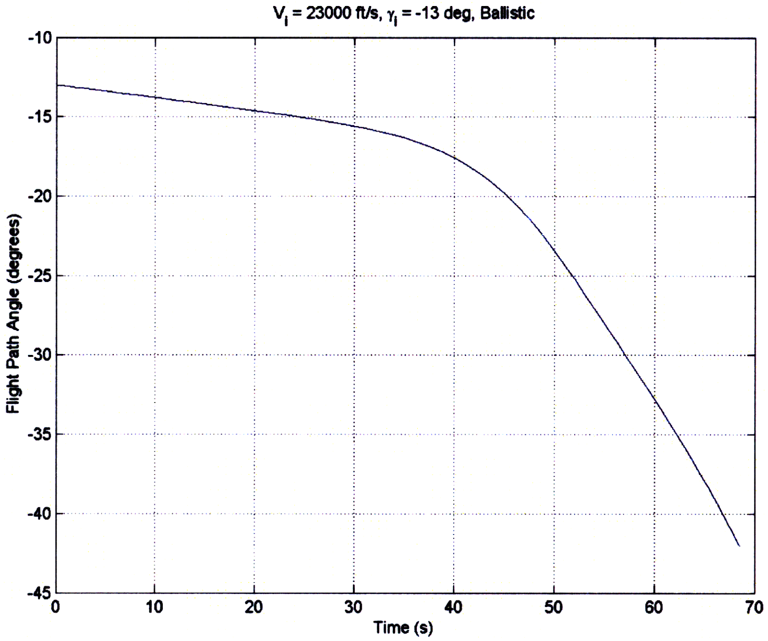

Figure 6-2: *The flight path angle history for the ballistic trajectory*

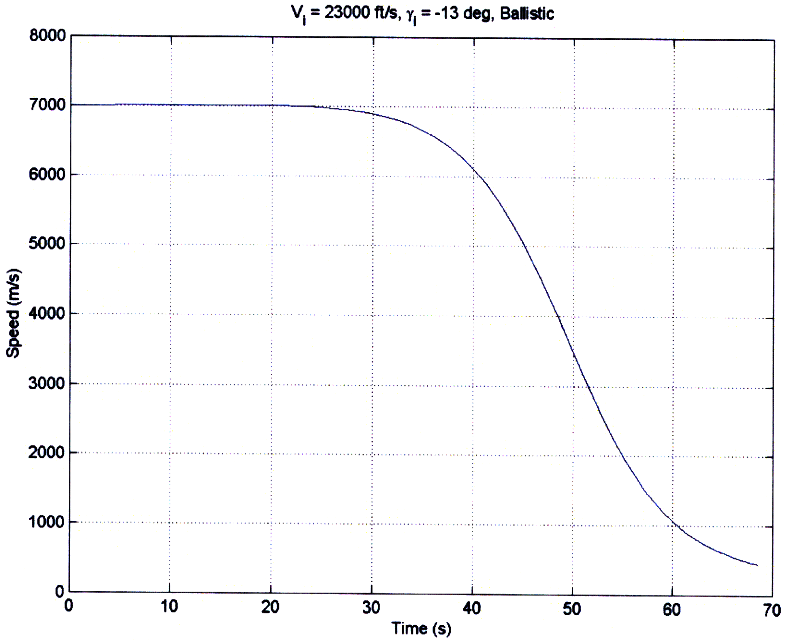

Figure 6-3: *The speed history for the ballistic trajectory*

6.2 Maximizing Downrange

One of the parameters used to assess the performance of this vehicle is the maximum downrange achievable, given some initial conditions and the terminal conditions. The fact that the vehicle has to meet terminal conditions restricts the maximum downrange. For example, since the terminal speed has to be over Mach 3, the vehicle cannot spend as much time traveling downrange, since drag is constantly acting on it.

We see in Figure 6-4 that the vehicle pulls up to a shallower γ (from $\gamma = -13$ deg to $\gamma = -3$ deg) soon after entering the sensible atmosphere (40 km altitude) to increase downrange. But since energy is being expended in this loft maneuver, the vehicle slows down, as we can see in Figure 6-6. Therefore, to meet the terminal speed constraint, the vehicle cannot stay at this shallow γ for long.

Also, the vehicle needs large amounts of downward lift to turn from a flight path angle of about -13 degrees to -80 degrees. This naturally means that for significant portions of its trajectory, the vehicle cannot use upward lift to stay aloft and fly farther downrange. From Figure 6-6, we see that the flight path angle changes the most after 60 seconds, indicating that the vehicle performs the large turn to $\gamma = -90$ degrees towards the end. Thus we see from Figure 6-5 that the additional downrange gained in the last 10 seconds is small compared to any 10-second interval in the middle of the trajectory.

In terms of the controls applied, we see in Figure 6-7 that the vehicle travels at the maximum allowed angle of attack of $\alpha = 10$ deg for as long as possible. After that, the vehicle quickly moves to a negative angle of attack, in order to be able to make the large turn to $\gamma = -80$ deg. Towards the end, the angle of attack again increases to be able to meet the $\alpha = 0$ deg terminal constraint. We see from the same figure that the lift direction angle stays at 0 deg, since intuitively the maximum downrange (for a non-rotating Earth) is when the vehicle stays in the same plane at all times.

In Figure 6-8, the G-loading figure shows two peaks - one at about 40 seconds and another at about 65 seconds. The first peak corresponds to the pull-up from $\gamma = -13$ degrees to $\gamma = -3$ degrees soon after entry into the sensible atmosphere. The second peak is due to the large amount of downward lift and drag that are needed to accomplish the final turn to $\gamma = -90$ degrees. However, note that the G-load always stays below $50g$s, indicating that the trajectory would remain the same even if the G-load were constrained to 55gs, as will be done later.

Also note in Figure 6-9 that the stagnation point heat rate stays well below the limit of 23 $Btu/s/ft^2$. Therefore, the maximum downrange trajectory will not be expected to change even when the stagnation point heat rate limit is introduced.

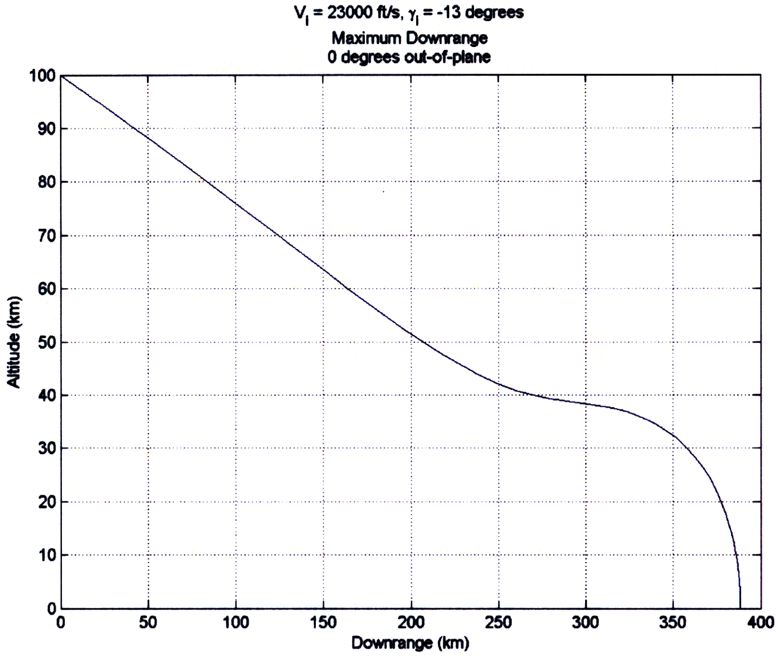

Figure 6-4: *The altitude vs downrange for Earth penetrator maximum downrange*

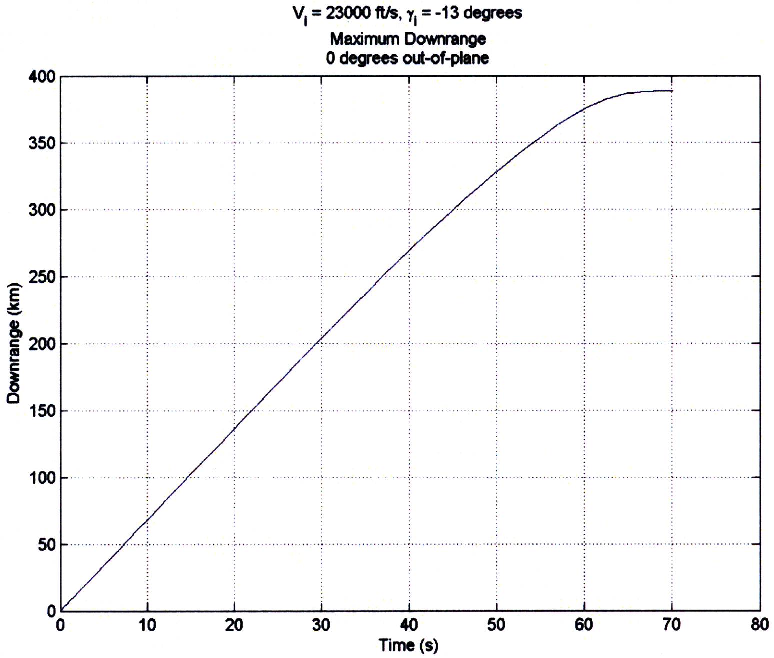

Figure 6-5: *The downrange history for the Earth penetrator maximum downrange trajectory*

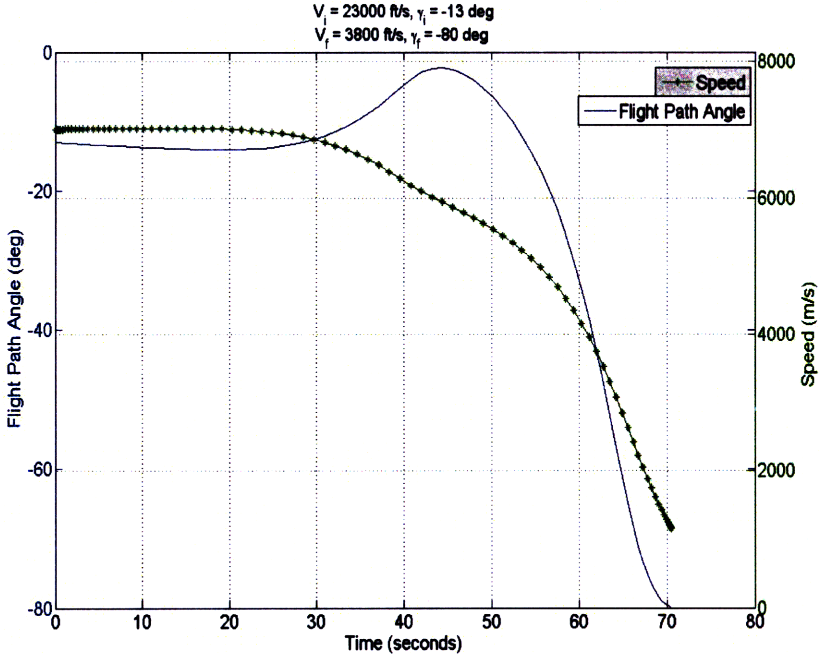

Figure 6-6: *The flight path angle and speed for Earth penetrator maximum downrange*

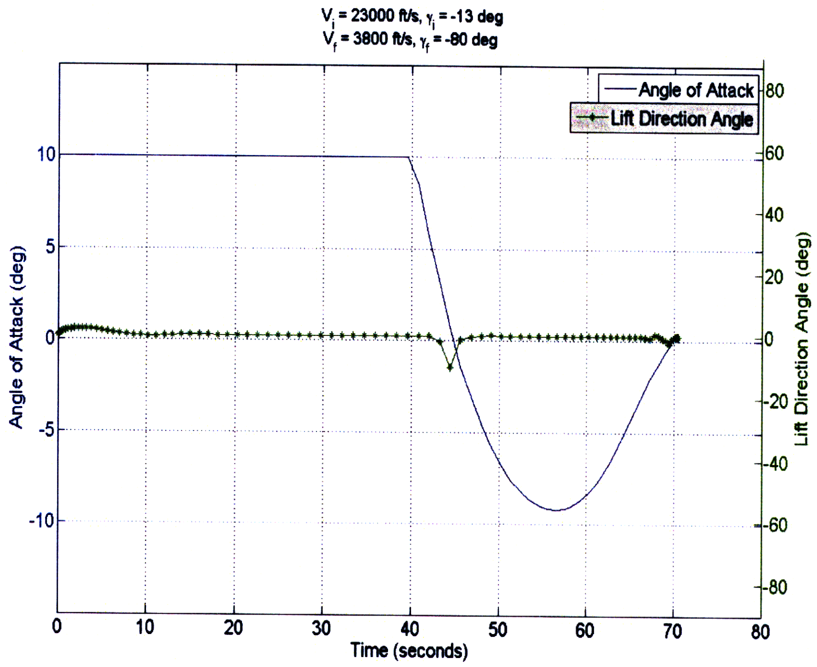

Figure 6-7: *The angle of attack and lift direction angle for Earth penetrator maximum downrange*

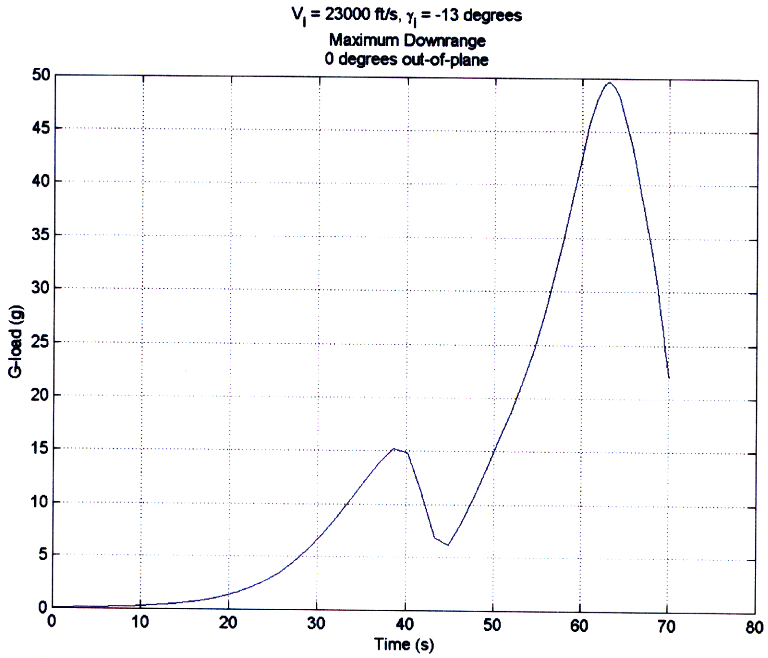

Figure 6-8: *The G-loading for Earth penetrator maximum downrange*

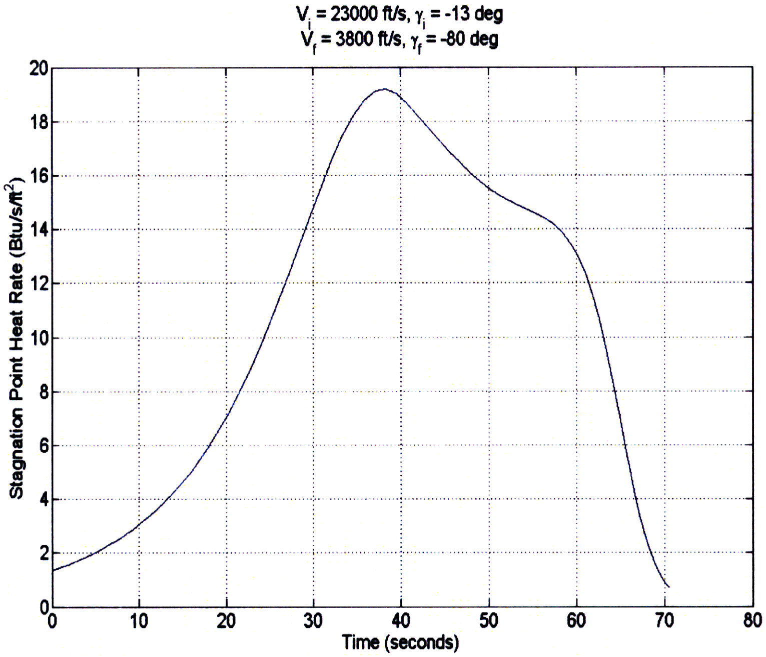

Figure 6-9: *The stagnation point heat rate for Earth penetrator maximum downrange*

6.3 Maximizing Out-of-Plane Motion

Another useful parameter to measure the performance of the vehicle is the maximum out-of-plane angle the vehicle reach, which is a measure of how far crossrange the vehicle can travel. In order to maximize crossrange distance, the vehicle needs to stay aloft for as long as possible, and during this time turn as much as possible. Both require lift, and since the lift available is limited (and is constantly decreasing as the vehicle slows due to drag) the vehicle needs to trade flight time and turn rate. The maximum crossrange occurs when the balance between flight time and turn rate is optimal.

Intuitively, we would expect the vehicle not to pull up (since this would require taking up a large amount of lift that could be used to increase turn rate). We would also expect the vehicle to not pull down, to be able to stay aloft long enough to achieve significant crossrange. Thus we would expect the flight path angle to remain roughly constant except at the end when $\gamma = -80$ degrees.

From Figure 6-12, we see that this is in fact what the vehicle does. γ is constant until the last 15 seconds of flight. Crossrange motion (Figure 6-11) shows a high curvature turn, except at the end when all the available lift is used to turn to $\gamma = -90$ degrees.

Figure 6-13 shows that the lift stays at an angle of almost 90 degrees for most of the flight - in other words, the lift vector is pointed perpendicular to the velocity. Also, the angle of attack is at the maximum $\alpha = -10$ deg, and is therefore generating the maximum lift possible. By generating the maximum lift possible, and pointing it perpendicular to the velocity vector, the vehicle achieves a very high turn rate for most of the trajectory. It is only towards the end, after 42 seconds, that the lift direction deviates from 90 deg and the angle of attack from -10 deg because this is when the vehicle makes its vertical turn to $\gamma = -90$ deg. The lift direction angle and the angle of attack eventually go to 0 at the end to meet the $\alpha = 0$ constraint.

Note that the G-load plot (Figure 6-14) looks similar to the corresponding plot for Maximum Downrange (Figure 6-8), except that there is only one peak because the vehicle does not pull up in this case. Also, the maximum G-loading is still below $55g$s, suggesting that the constrained solution will be the same as the unconstrained solution. Similarly, the maximum stagnation point heat rate stays below the limit of 23 $Btu/s/ft^2$, but is almost exactly at this upper limit. We will see in the next section that the minimum uprange trajectories will change when the path constraints are added. Therefore, the maximum-out-of-plane case represents the edge between the uprange trajectories (which are affected by the path constraints) and the downrange trajectories (which are not affected).

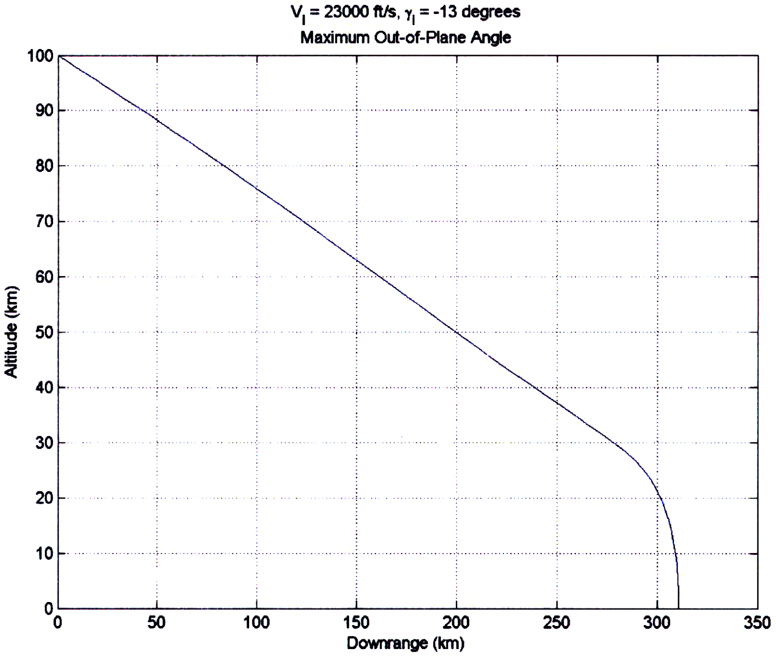

Figure 6-10: *The downrange vs altitude for Earth penetrator maximum out-of-plane angle*

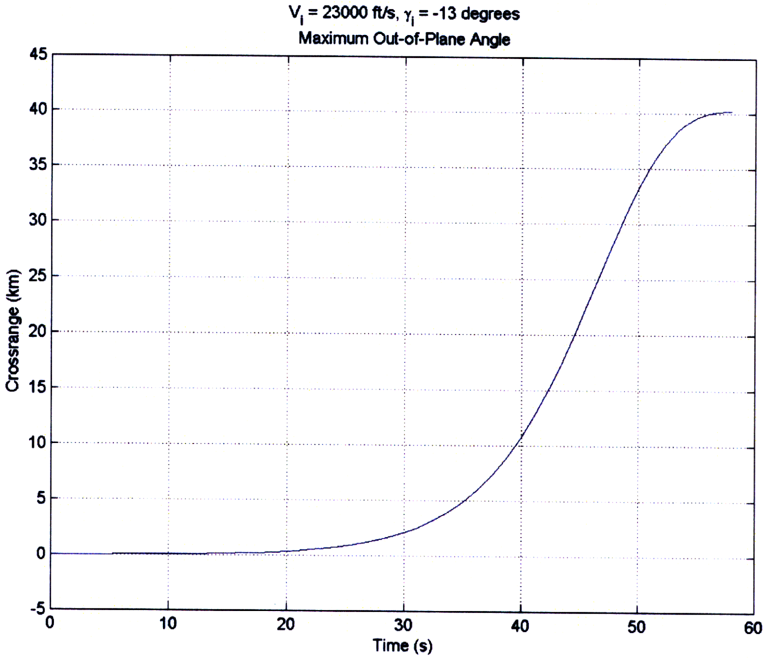

Figure 6-11: *The crossrange history for Earth penetrator maximum out-of-plane angle*

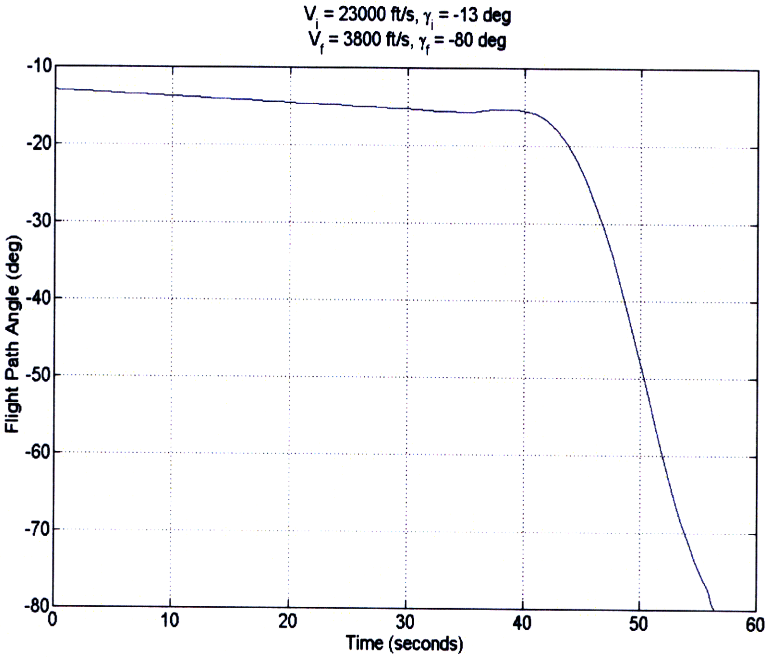

Figure 6-12: *The flight path angle for Earth penetrator maximum out-of-plane angle*

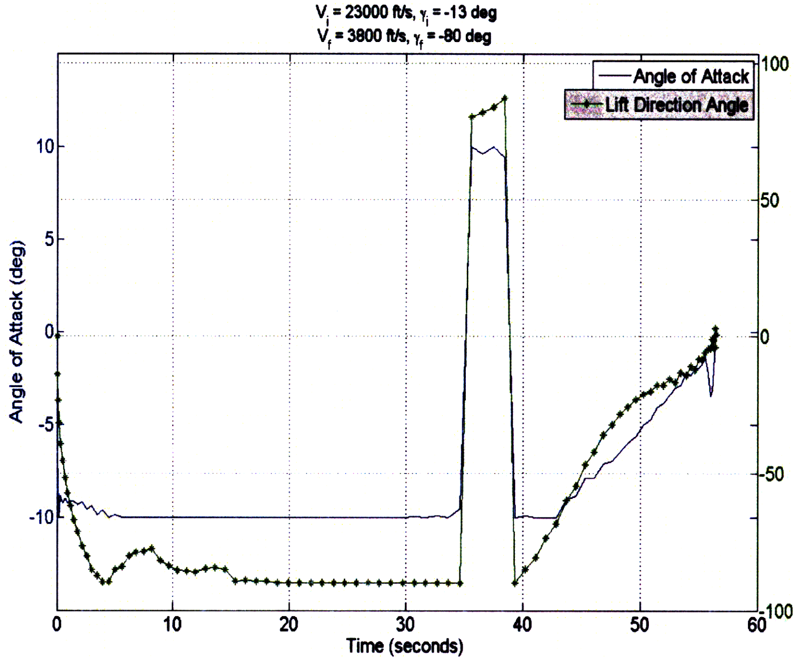

Figure 6-13: *The angle of attack and lift direction angle for Earth penetrator maximum out-of-plane angle*

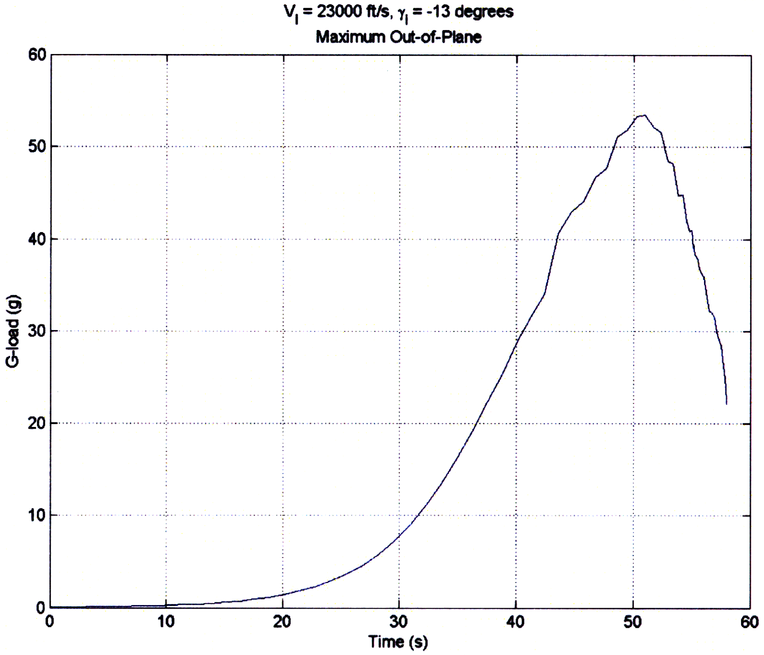

Figure 6-14: *The G-loading for Earth penetrator maximum out-of-plane angle*

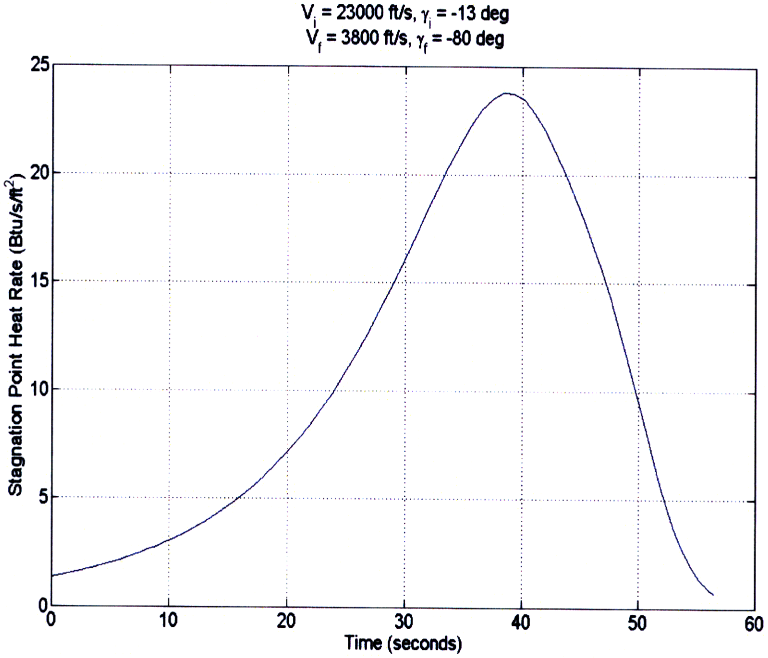

Figure 6-15: *The stagnation point heat rate for Earth penetrator maximum out-of-plane angle*

6.4 Minimizing Downrange

Another parameter used to assess the performance of this vehicle is the minimum downrange achievable, given some initial conditions and the terminal conditions. The main challenge in achieving a minimum downrange is the fact that the vehicle is traveling at a high initial speed (23000 ft/s). Also, the vehicle must spend some time in the atmosphere to lose enough speed and meet the terminal speed condition. The solution for the minimum downrange problem is to thus spend as much time in the atmosphere as needed to achieve the terminal speed, but not more. From Figure 6-16 we can see that the vehicle begins a steep descent almost immediately upon entering the sensible atmosphere. The flight path angle (Figure 6-17) shows that the vehicle chooses a steep trajectory to minimize the downrange distance. However, the vehicle is going much too fast at this point to meet the terminal speed condition of 1160 m/s, and therefore pulls up briefly. This expends enough energy for the vehicle to slow itself down and reach the terminal speed condition.

For the controls, we see that vehicle flies at an angle of attack of $\alpha = -10$ deg for most of the trajectory. The lift direction vector is at $\sigma = 0$ deg, i.e. in the plane of motion. Thus the lift is pointed directly down. Since $\alpha = -10$ deg is the maximum allowed control, the vehicle is accelerating downwards as rapidly as its control authority will allow. The increase in angle of attack to 10 deg for a brief interval between 35 seconds and 40 seconds is primarily to expend energy and slow the vehicle down to the required terminal speed of 3800 ft/s. Towards the end of the trajectory, the angle of attack goes to 0 deg as required by the terminal constraint.

In Figure 6-19, we see that the peak G-loading occurs during the final turn to γ_f =-90 deg, similar to the maximum downrange case (Figure 6-8). However, since the vehicle is going much faster than in the maximum downrange case, the G-load is much higher - in fact, the maximum G-load is over 120gs, more than twice the allowed limit. Therefore, when the G-load constraint is added, the minimum uprange will be much greater.

From Figure 6-20, we see that the peak stagnation point heat rate also occurs during the low-altitude, vertical turn to $\gamma = -90$ deg. The peak heat rate of 30 $Btu/s/ft^2$ is well above the limit of 23 $Btu/s/ft^2$. Therefore, when the stagnation point heat rate limit is added, the minimum uprange can be expected to increase.

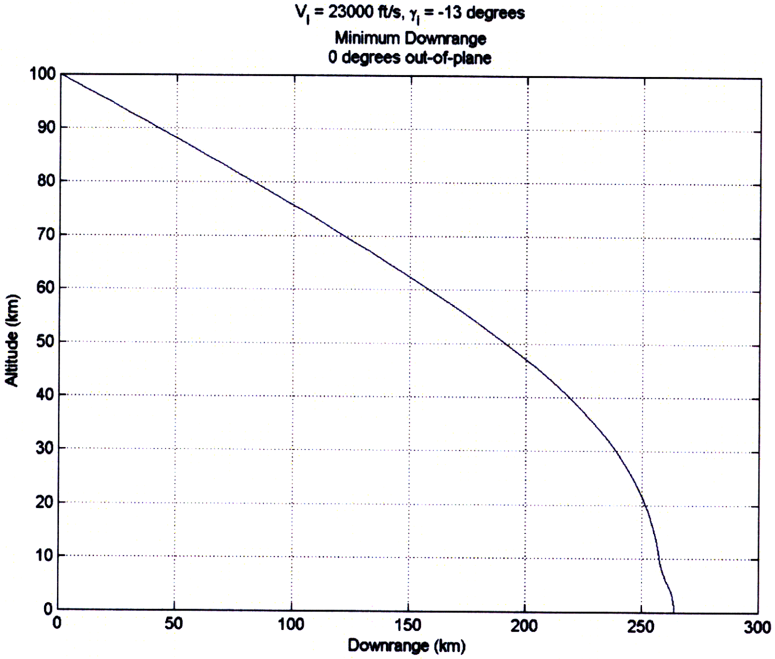

Figure 6-16: *The altitude as a function of downrange for initial conditions* $V_i = 23000$ *ft/s,* $\gamma_i = -13$ *degrees,* $\psi_i = 0$ *with controls optimized to minimize downrange*

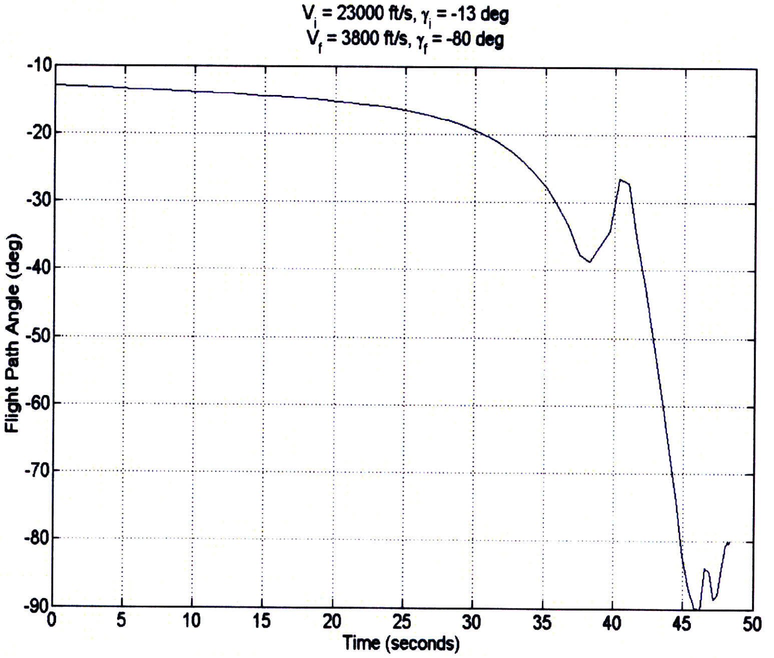

Figure 6-17: *The flight path angle for initial conditions* $V_i = 23000$ *ft/s,* $\gamma_i = -13$ *degrees,* $\psi_i = 0$ *with controls optimized to minimize downrange*

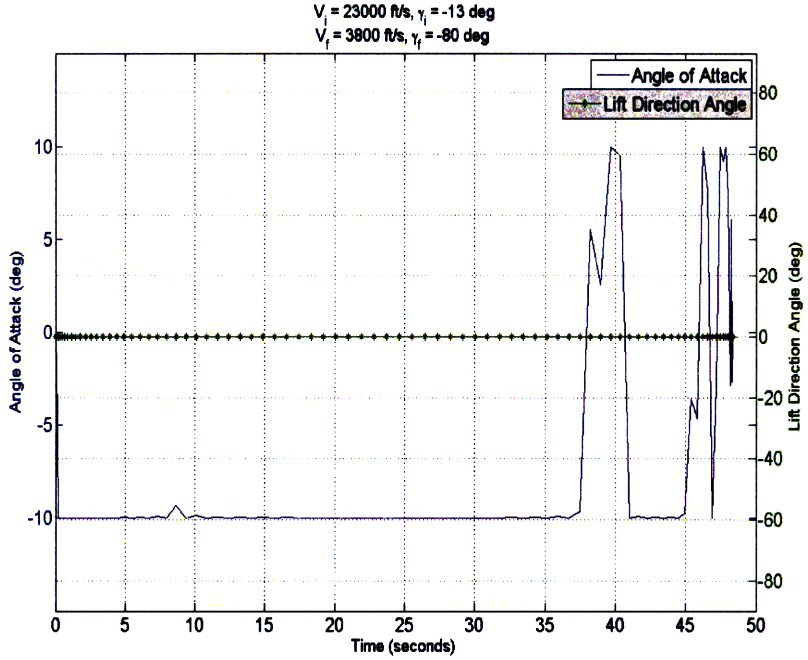

Figure 6-18: *The flight path angle for initial conditions* $V_i = 23000$ *ft/s,* $\gamma_i = -13$ *degrees,* $\psi_i = 0$ *with controls optimized to minimize downrange*

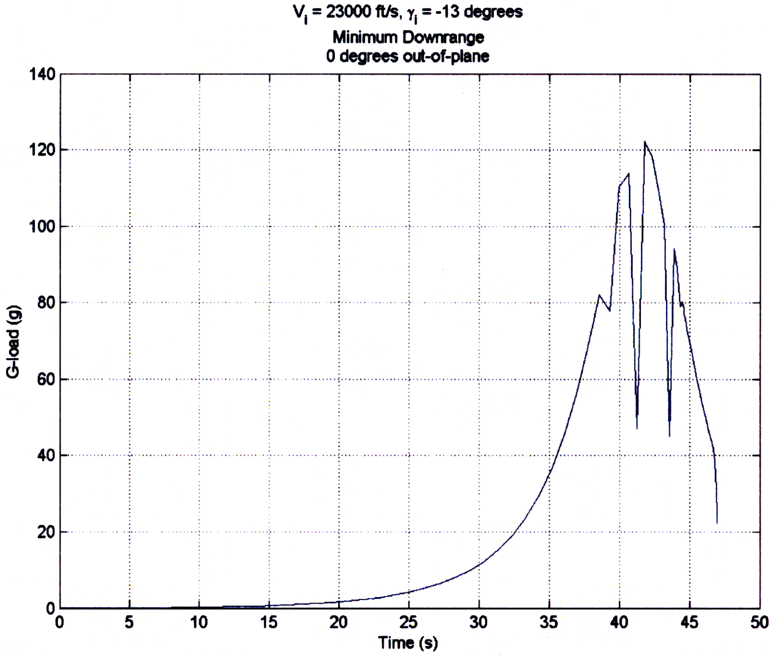

Figure 6-19: *The G-loading experienced by the vehicle for initial conditions* $V_i = 23000$ *ft/s,* $\gamma_i = -13$ *degrees,* $\psi_i = 0$

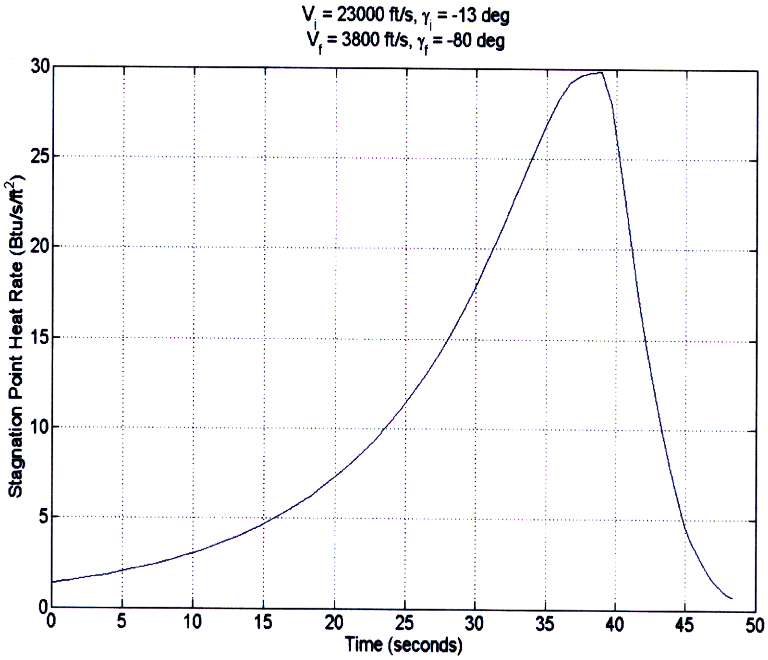

Figure 6-20: *The heat loading experienced by the vehicle for initial conditions* $V_i = 23000$ *ft/s,* $\gamma_i = -13$ *degrees,* $\psi_i = 0$

6.5 Footprint

In the previous sections, we have looked at three of the most important cases in determining a landing footprint - the maximum downrange, the minimum uprange, and the maximum out-of-plane angle. In order to determine the rest of the footprint, we first constrain the terminal point of the trajectories to lie along a line representing a certain out-of-plane angle, and then maximize and minimize the downrange distance. Completing this process, we get the landing footprint shown in Figure 6-21.

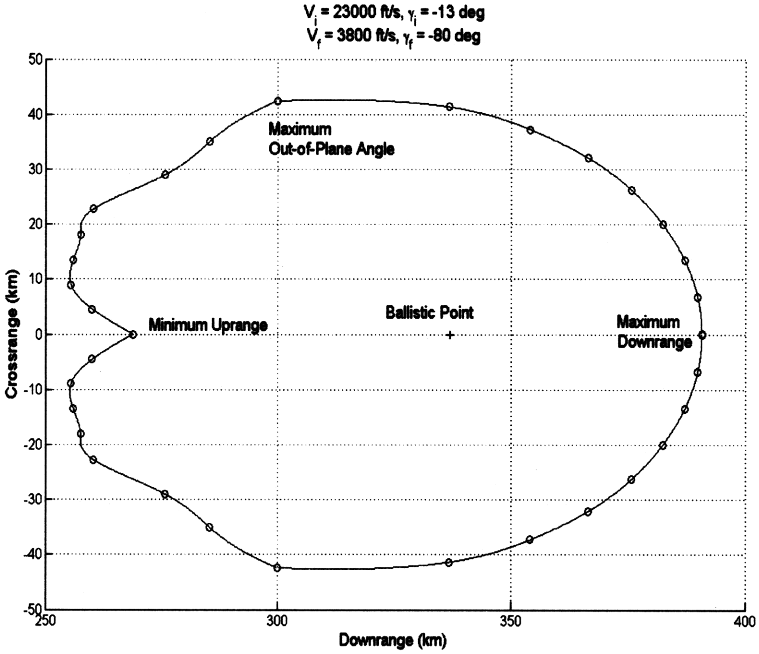

Figure 6-21: *The footprint for initial conditions* $V_i = 23000$ *ft/s,* $\gamma_i = -13$ *degrees,* $\psi_i = 0$ *with no path constraints*

As seen previously, when the vehicle is commanded to maximize downrange, it travels at an angle of attack of $\alpha = 10$ deg, with the lift vector pointed directly up ($\sigma = 0$ deg) for as long as possible. But to travel out-of-plane, the vehicle needs to point its lift vector towards the direction it wishes to turn ($\sigma \neq 0$ deg). Therefore, some of the lift is being used to turn rather than to stay aloft. And the greater the out-of-plane angle, the more the lift that is needed to turn. This means that as the out-of-plane angle is increased, the trajectories are shorter, and the downrange achieved is also shorter. Another way to view this is in terms of energy - as the trajectory is constrained to lie out-of-plane, the vehicle has to expend some of its available energy to turn and reach the specified out-of-plane angle. Hence it has less energy available for traveling downrange, and therefore loses downrange as this angle is increased.

When the vehicle is commanded to minimize uprange, it travels at an angle of attack of $\alpha = -10$ deg, with the lift vector pointed directly down, for as long as possible. But as discussed in the previous paragraph, the vehicle needs to point its lift vector in the direction of turn in order to travel out-of-plane. Therefore, the vehicle cannot lose altitude as fast, resulting in longer trajectories and longer downrange distances.

Thus, as the out-of-plane angle is increased, the minimum uprange distance *increases* while the maximum downrange distance *decreases.* This continues until that out-of-plane angle at which the maximum downrange and minimum uprange are the same. This is the maximum out-of-plane angle. This happens when the lift direction is pointed perpendicular to the velocity ($\sigma = 90$ deg), giving the vehicle its maximum possible turn rate.

In this case, the controls are the angle-of-attack and lift direction angle. Thus we now define "control effort" as the sum of the squares of the angle of attack and lift direction angle, $\alpha^2 + \sigma^2$. This is related to the actual torque (and hence fuel) used by the reaction control system. As discussed before, the vehicle is statically stable and hence requires torque to hold itself at a non-zero angle of attack or to change the direction of its lift. Thus by penalizing a non-zero angle of attack and lift direction vector, we get a measure of how much "control effort" the vehicle is making. Note that to get a full representation of torque and fuel use, we would have to use a 6-DOF model, but for now we use a simpler representation.

Since both maximum downrange and minimum uprange require using significant control effort, there is likely a point in between that requires the minimum control effort. This "minimum control effort" will not be zero, since the vehicle still needs to use some control effort to meet its terminal constraints. Thus the ballistic trajectory would *not* be the minimum-control-effort trajectory since it does not satisfy the terminal constraints. Therefore, if the vehicle were commanded to reach its terminal conditions while minimizing the control (α and σ) used, we reach a certain downrange that is not the same as the ballistic point.

We can extend this idea further by including the out-of-plane angle constraint. For every terminal out-of-plane angle, there is a minimum control-effort trajectory whose terminal point lies in between the corresponding maximum downrange and minimum uprange points for that out-of-plane angle. These minimum-control-effort landing points for all feasible out-of-plane angles are shown in Figure 6-22. Note that the maximum downrange, minimum uprange, and the minimum-control-effort points are all the same at the maximum out-of-plane angle, since there is only one unique trajectory that enables the vehicle to reach this point.

Another point to note is that the landing footprint encloses the ballistic point. However, we have seen previously that the ballistic trajectory does not satisfy all the terminal constraints. This implies that in order to hit the location of the ballistic point, the vehicle would actually have to maneuver. This is seen in Figure 6-23. The vehicle first lofts itself in the upper atmosphere to be able to travel the required downrange distance without losing too much speed. Then, it makes a sharp vertical turn to reach the ground with a flight path angle of $\gamma = -80$ deg.

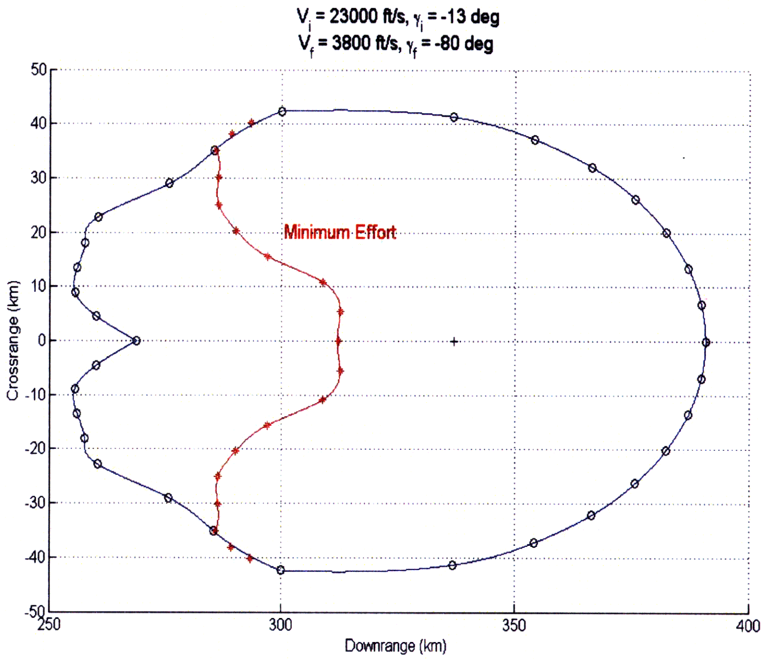

Figure 6-22: *The "minimum effort" line, showing the point inside the footprint that requires the least control effort, for each out-of-plane angle*

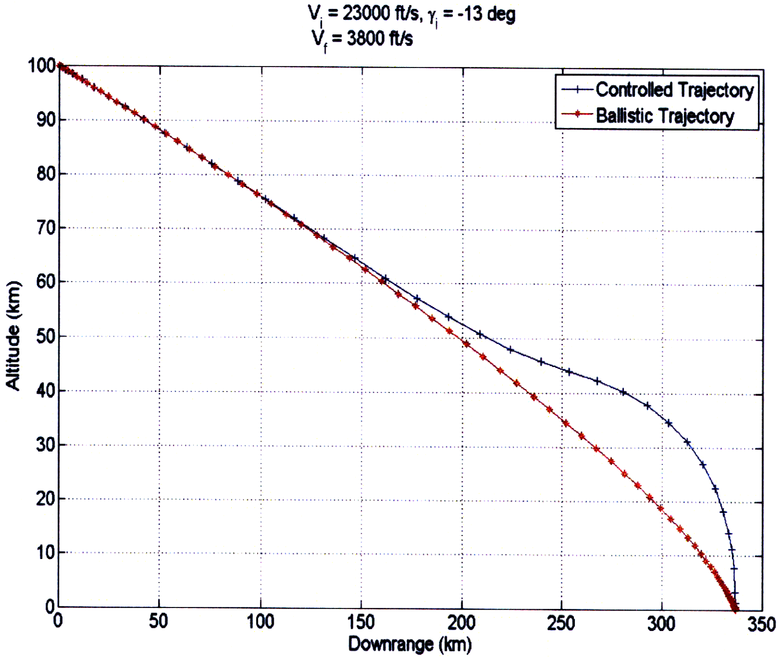

Figure 6-23: *Here we see that the trajectory that the vehicle follows to reach the ballistic point is not the ballistic trajectory, since the ballistic trajectory does not meet the terminal constraints. The vehicle must maneuver to hit a target at the ballistic point*

6.6 Effect of Initial Conditions

Clearly, the size and location of the landing footprint is very dependent on the initial conditions, specifically the speed and flight path angle γ. The footprint presented above is for the initial conditions $V_i = 23000$ ft/s and $\gamma_i = -13$ deg. When the initial speed is greater, the vehicle has more energy, and can expend this energy in maneuvers. Therefore, the size of the footprint should increase. When the initial flight path angle is more shallow (i.e. closer to 0), the size of the footprint stays roughly the same (since the initial energy is the same) but the footprint will move farther downrange, because the vehicle travels farther downrange before it enters the sensible atmosphere. These trends are clearly seen in Figure 6-24 below.

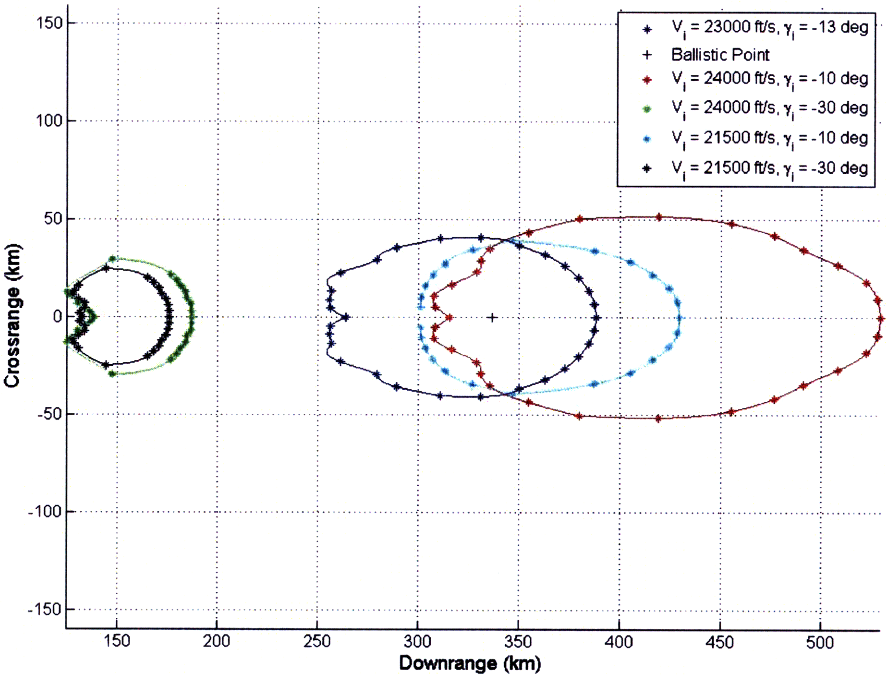

Figure 6-24: *The footprints for four sets of initial conditions with no path constraints*

From the plot, we see that the nominal case $V_i = 23000$ ft/s, $\gamma_i = -13$ deg, has a slightly larger footprint than the $V_i = 21500$ ft/s and $\gamma_i = -10$ deg case, but the footprint for the shallower trajectory is shifted farther downrange. However, the case with $V_i = 24000$ ft/s and $\gamma_i = -10$ deg has a much larger footprint than either of those cases because of its higher initial speed.

The footprints for the two cases with $\gamma = -30$ deg are shifted uprange significantly. They are also much smaller in size than the shallower trajectories. This is because the vehicle is rapidly descending (without traveling as far downrange) and has little time to maneuver. But comparing the two steep cases, we see that between them the case with the higher initial speed has a larger footprint. Overall, the trajectories with $\gamma = -30$ deg have shorter trajectories than those with $\gamma = -10$ deg.

6.7 Effect of Terminal Conditions

The size and shape of the landing footprint depends on not just the initial conditions, but the terminal constraints as well. In the results presented previously, the terminal constraints were $V_f = 3800$ ft/s, $\gamma_f = -80$ deg, with the final heading angle ψ_f unconstrained. In this section, we will see how the footprint changes when γ_f is changed, and when a constraint on ψ_f is introduced.

6.7.1 Flight Path Angle

Figure 6-26 shows the footprints for $\gamma_f = -80$ deg, $\gamma_f = -70$ deg and $\gamma_f = -60$ deg. The figures show that as the final flight path angle increases, i.e. gets farther from $\gamma_f = -80$ deg, the size of the footprint *decreases*. When we look at Figure 6-25, we see that the footprint again shrinks when the terminal flight path angle is changed to $\gamma_f = -90$ deg.

The second effect can be explained by the fact that reaching a terminal flight path angle that is very steep (such as $\gamma_f = -90$ deg) requires energy, in particular during the large vertical turn at the end.

However, reaching a shallow terminal flight path angle requires energy as well. This is because the vehicle would have to turn sharply and come into the lower atmosphere at a relatively steep flight path angle. It must do this because if it enters the lower atmosphere at a shallow flight path angle, it would spend too much time in dense atmosphere and lose too much speed to be able reach the terminal speed of 3800 ft/s. Therefore, the "natural" motion of the vehicle, if the terminal flight path angle were not constrained, would be to come in at a steep γ. When the terminal γ is constrained to be shallower than this "natural" terminal γ, the vehicle has to spend some energy in making the final turn to this shallower γ, an expenditure which would manifest itself as a shorter maximum downrange.

By commanding the vehicle to maximize downrange without a terminal constraint, we find that the "natural" terminal flight path angle is $\gamma_f = -80.7$ deg. Therefore, any constraint on γ_f that is farther away from -80.7 deg will yield a smaller footprint with a smaller maximum downrange. This is the reason why the $\gamma_f = -80$ deg footprint is the largest and has the longest maximum downrange, while all the other footprints ($\gamma_f = -70$ deg, $\gamma_f = -60$ deg, $\gamma_f = -90$ deg) have smaller footprints and shorter maximum downranges.

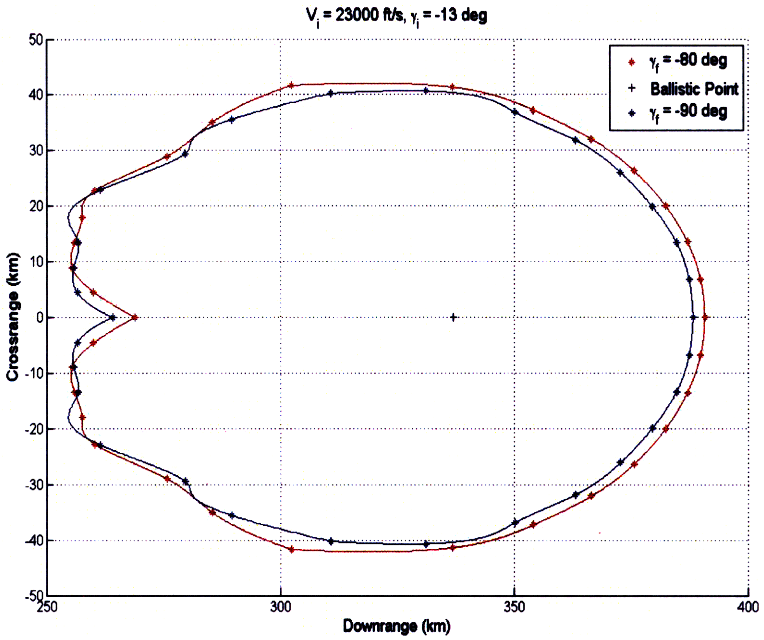

Figure 6-25: *The footprints when the final flight path angle* γ *is changed.*

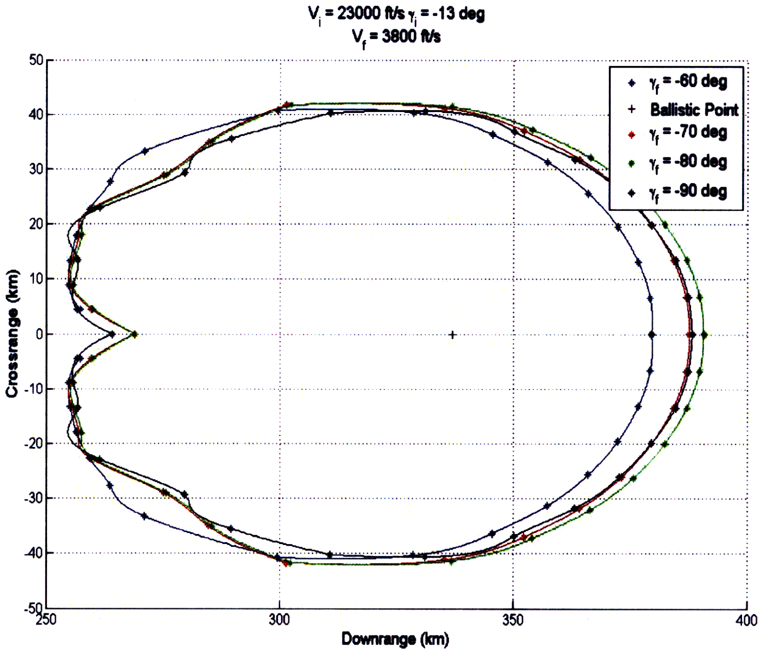

Figure 6-26: *The footprints for the cases* γ_f = *-80 deg (green),* γ_f = *-70 deg (red) and* γ_f = *-60 deg (blue)*

6.7.2 Heading Angle

Next, we look at the effect of adding a heading angle constraint. We constrain the final heading angle to be a specific value: $\psi_f = 0$ deg, $\psi_f = 10$ deg, $\psi_f = 30$ deg, $\psi_f = 60$ deg, and $\psi_f = 90$ deg. From Figure 6-27, we notice first that the crossrange symmetry of the footprints is broken when a non-zero heading angle constraint is added. Only for the $\psi_f = 0$ deg case, the footprint is different from the unconstrained case, but remains symmetric. As ψ_f is varied to be farther away from 0, the footprints become less symmetric. This is clear from Figure 6-28, which shows the crossrange for out-of-plane angles of 5 degrees and -5 degrees with $\psi_f = 90$ deg. Clearly, the vehicle can achieve less crossrange in the -5 degrees case since it needs to turn to a negative heading angle to reach -5 degrees out-of-plane, and then turn to a positive heading angle of 90 degrees at the end. From the same figure, we see that the footprint when the heading angle is unconstrained encloses all the footprints with a heading angle constraint.

Also note in Figure 6-27 that as γ_f is constrained to be non-zero and positive, the most significant loss in footprint area occurs on the minimum uprange, negative crossrange region. This is because the vehicle does not have enough control authority to simultaneously minimize uprange, travel a significant crossrange distance, and then turn in the opposite direction to meet the heading angle constraint.

In general, the farther away the heading angle is from 0, the less the maximum downrange. From Figure 6-29, we see that this is because in the unconstrained case, the natural final heading angle is 0. Therefore the farther from 0 the heading angle, the more the trajectory is forced away from the unconstrained optimal.

Note that in general, for an Earth Penetrator mission, the vehicle will have a terminal velocity vector that is perpendicular to the local terrain. If the terrain were to be viewed as an uneven surface, the normal vector to the surface at the target location would determine both the terminal flight path angle and the terminal heading angle. Therefore, in reality, the vehicle will have both constraints, as was the case in this section.

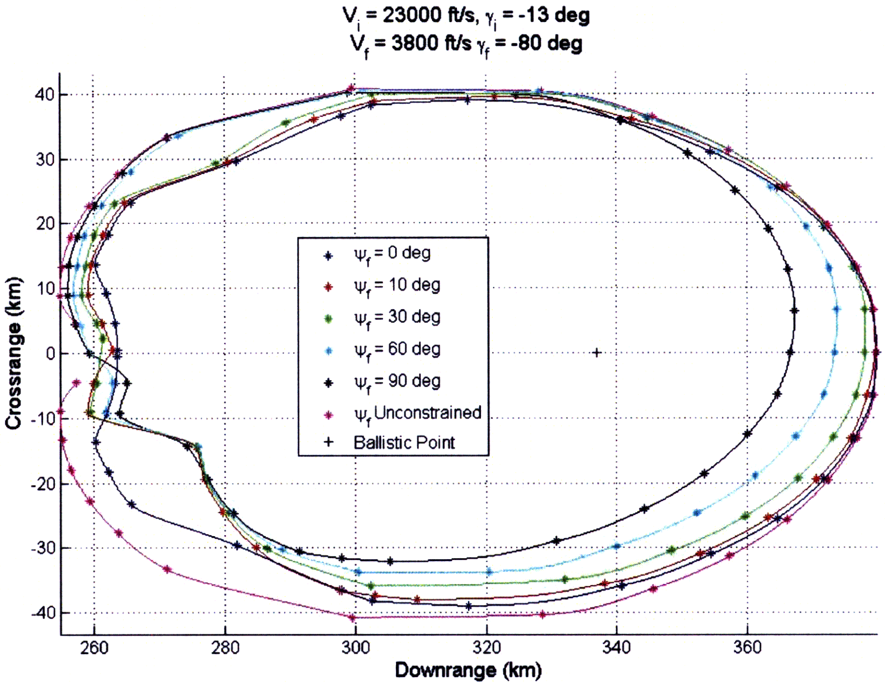

Figure 6-27: *The footprints for various values of final heading angle* ψ_f*. Shown are* $\psi_f = 0$ *deg (blue),* $\psi_f = 10$ *deg (red) and* $\psi_f = 30$ *deg (green)*

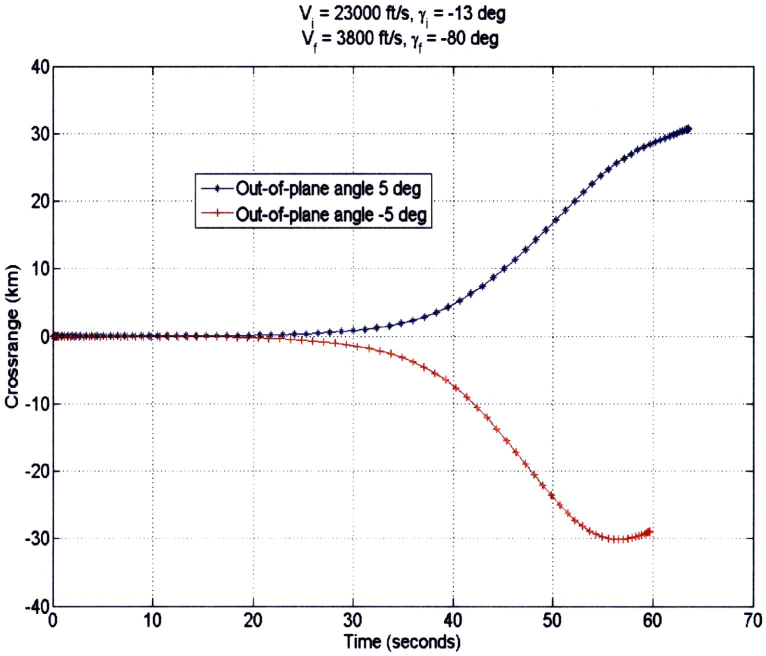

Figure 6-28: *The trajectories for out-of-plane angles 5 deg and -5 deg are not symmetric when a terminal heading angle constraint is added*

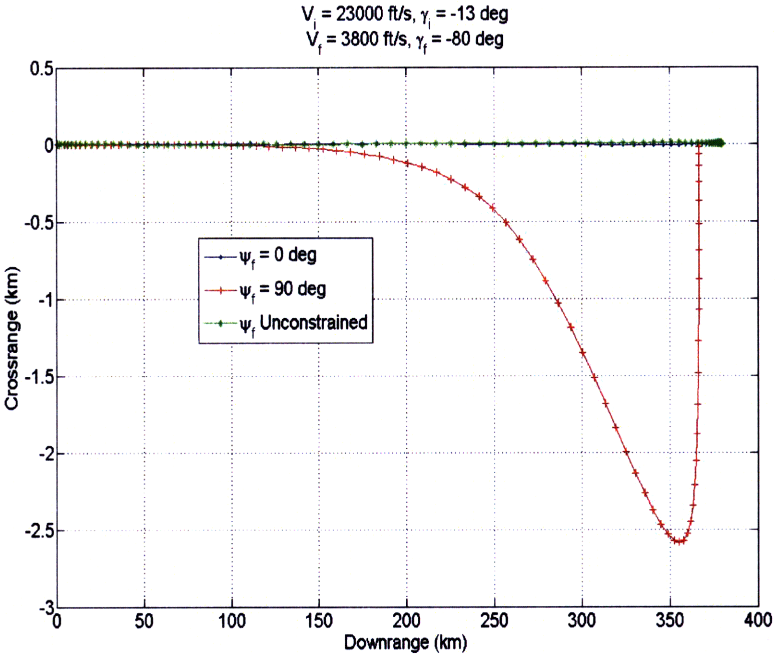

Figure 6-29: *The maximum downrange for* ψ_f = *0 deg (blue),* ψ_f = *90 deg (red) and* ψ_f *Unconstrained (green)*

6.8 Path Constraints

The results presented thus far have assumed that the only restrictions on the vehicle's capabilities come from the control system, i.e. the maximum angle of attack. In reality, this would not be true - the structure of the vehicle, as well as its guidance system would impose limits of their own. Two of the limits considered here are the maximum G-load limit and the maximum stagnation point heating rate limit. The G-load limit comes from the structural strength of the vehicle. The stagnation point heat rate limit comes from the external heat shield of the vehicle and its ability to dissipate the aerodynamic heating of the vehicle.

6.8.1 Maximum G-load

The maximum G-load that the vehicle can sustain is given as $60gs$. As mentioned before, some margin is added in this analysis and the maximum G-load is restricted to be $55gs$. The G-load is essentially the sum of the external forces acting on the vehicle, in this case lift and drag. As we saw in the "Minimum Uprange" case, the G-loading on the vehicle becomes very large ($> 55gs$) when trying to achieve minimum uprange, since large amounts of drag and lift are used to simultaneously slow down the vehicle and turn to $\gamma = -80$ degrees as quickly as possible. Therefore when a G-load constraint is added, the minimum uprange changes significantly.

We see the effect of adding a G-load constraint clearly in Figure 6-31. It shows that the vehicle cannot turn as fast as in the unconstrained case. This is particularly true at altitudes below 20 km, where the density (and hence lift and drag) is high. The vehicle cannot keep turning at this low altitude, because that would induce aerodynamic forces that are greater than the G-load limit. This is also seen in Figure 6-33, which shows how the flight path angle for the G-load constrained case is always shallower than it is for the unconstrained case, since the vehicle is turning slower. This is particularly true in the terminal stages of the trajectory. The result of this slower turn rate is that the vehicle ends up traveling farther downrange - thus the minimum uprange is extended. On the other hand, the maximum downrange and the maximum out-of-plane angles are unaffected, since even the unconstrained optimal trajectories stayed within the G-load limit. The landing footprint for the G-load constrained vehicle is shown in Figure 6-30. As expected, adding a constraint restricts the performance of the vehicle, which is apparent in the smaller landing footprint.

Another interesting feature of the G-load constrained trajectories is the crossrange motion of the vehicle when G-load constraints are added. Recall that in the unconstrained case, minimum uprange was achieved by keeping the angle of attack at $\alpha = -10$ deg, in the plane of motion. This gave the vehicle its maximum turn rate and descent rate allowed by the control limits. However, this also resulted in lift and drag forces that were well above the limit of $55g$s. With this constraint added, the vehicle cannot choose this trajectory anymore. As a result, the vehicle chooses to minimize its downrange motion by traveling in the crossrange direction instead. Crossrange motion allows the vehicle to lose speed without gaining as much downrange.

The G-load plot in Figure 6-34 shows the benefit of the slower turn rate - that the G-loading on the vehicle is now below $55gs$ for the entire trajectory, much lower than in the unconstrained case.

As we have already seen, footprint size depends on the initial conditions. This is especially true when the G-load limit is added, since a fast, steep trajectory is much more likely to have high G-loading than a slow and shallow trajectory. Therefore, upon adding the G-load constraint, the footprint for a slow, shallow trajectory (for instance, with initial conditions $V_i = 21500$ ft/s, $\gamma_i = -10$ deg) should change less than the footprint for a fast, steep trajectory (with initial conditions $V_i = 24000$ ft/s, $\gamma_i = -30$ deg). From Figures 6-35 and 6-36, we see that this is the case - the footprint for the slow and shallow case (Figure 6-35) changes very little when the G-load constraint is added, compared to the fast and steep case (Figure 6-36), where the footprint shrinks to just half the size of the unconstrained footprint.

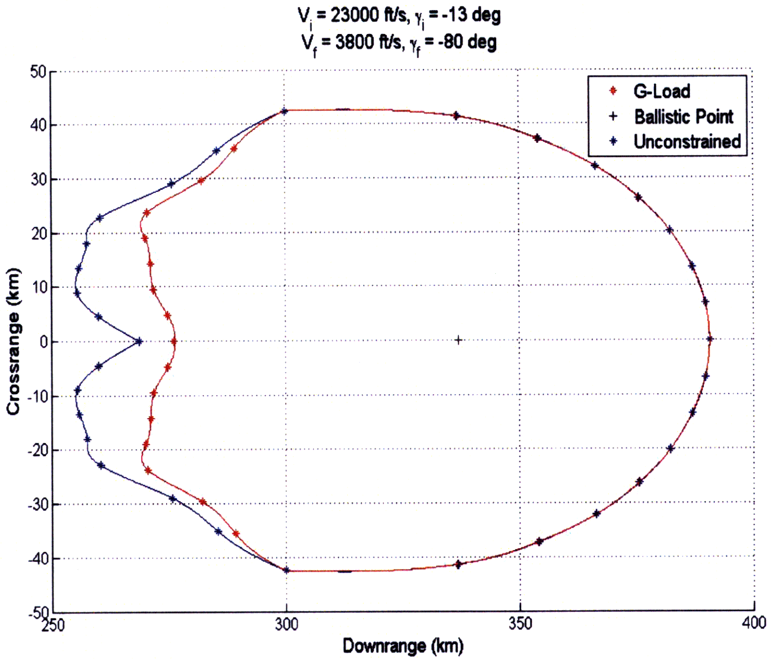

Figure 6-30: *The footprint with no path constraints (blue), and a G-load constraint (red)*

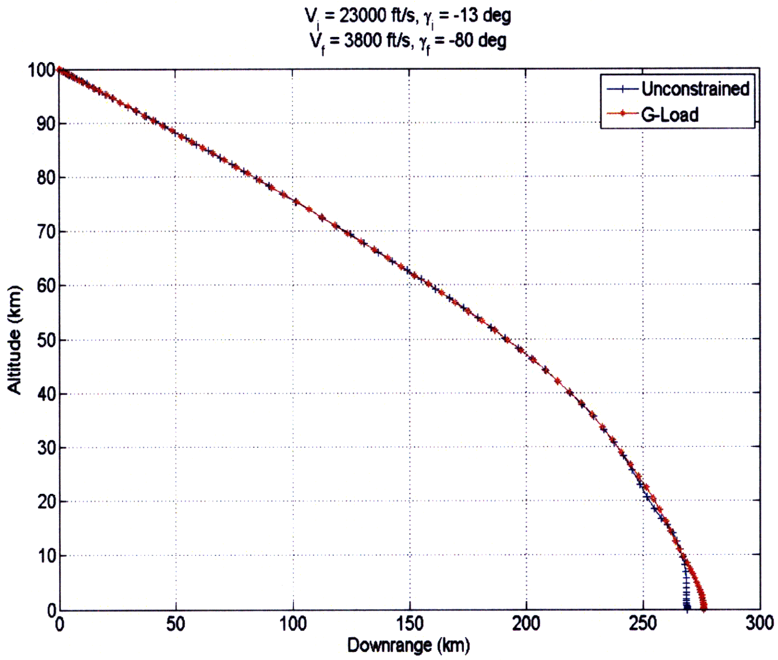

Figure 6-31: *The Altitude vs Downrange for minimum uprange, with no path constraints (blue), and a G-load constraint (red)*

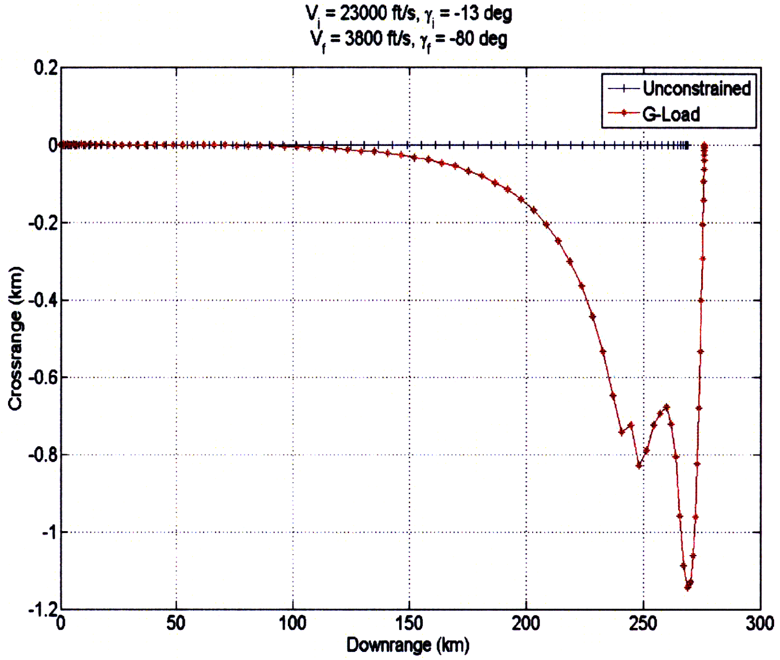

Figure 6-32: *The Crossrange vs Downrange trajectories, with no path constraints (blue), and a G-load constraint (red)*

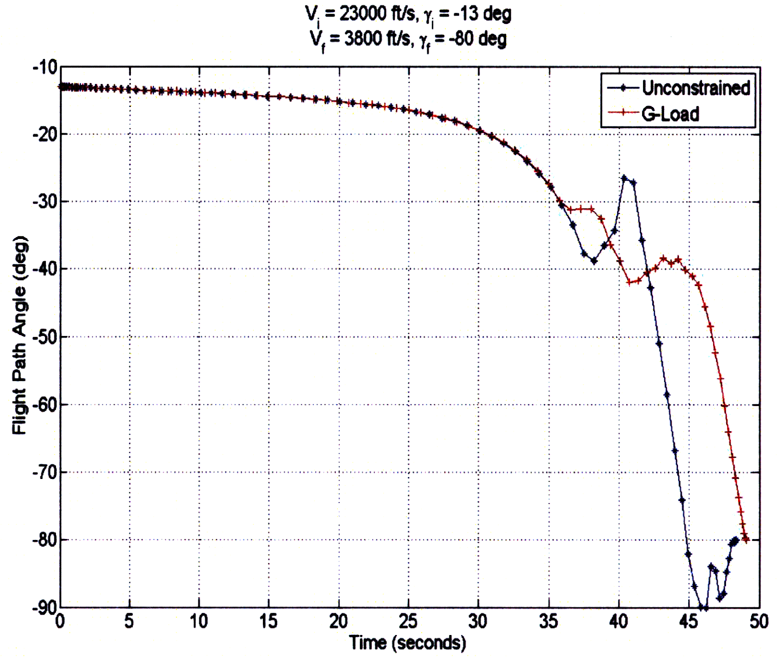

Figure 6-33: *The Flight Path Angle with no path constraints (blue), and a G-load constraint (red)*

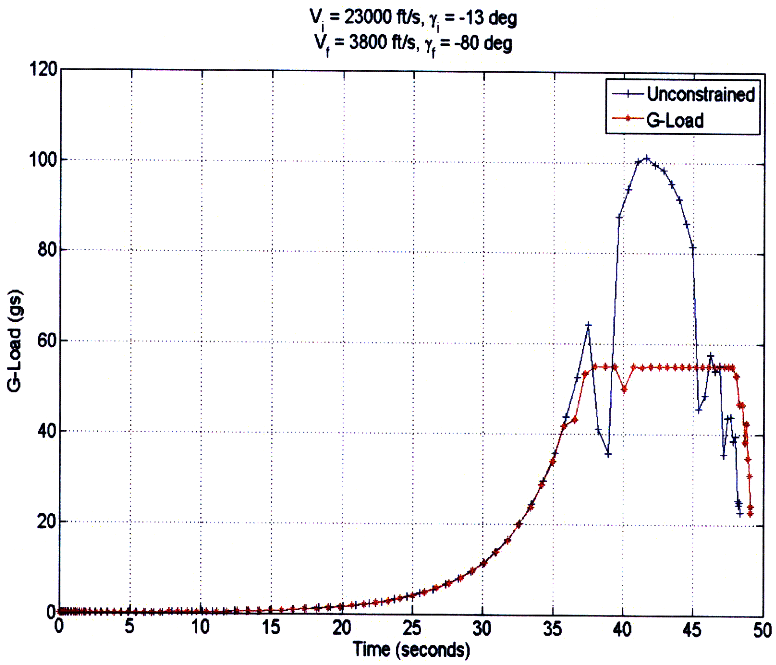

Figure 6-34: *The G-Loading for the minimum uprange trajectory, with no path constraints (blue), and a G-load constraint (red)*

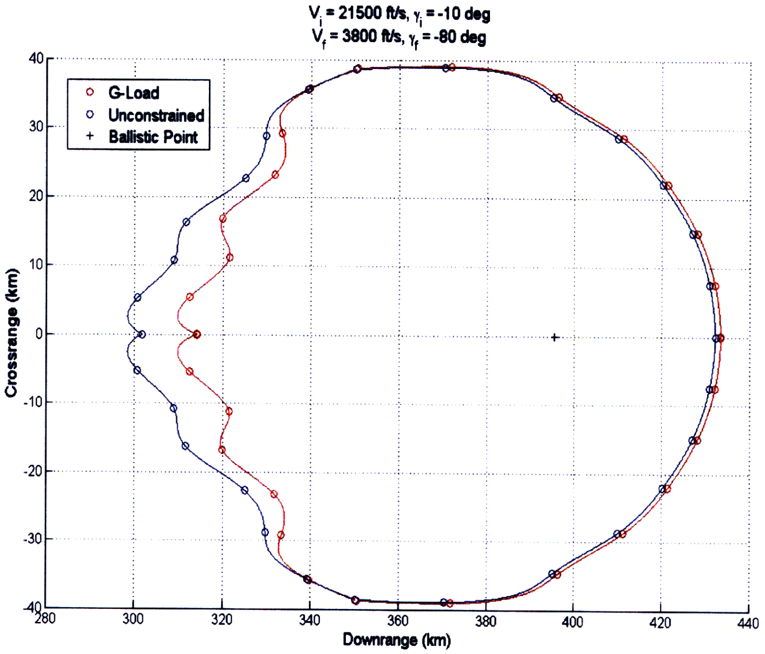

Figure 6-35: *The footprint with no path constraints (blue), only a G-load constraint (red)*

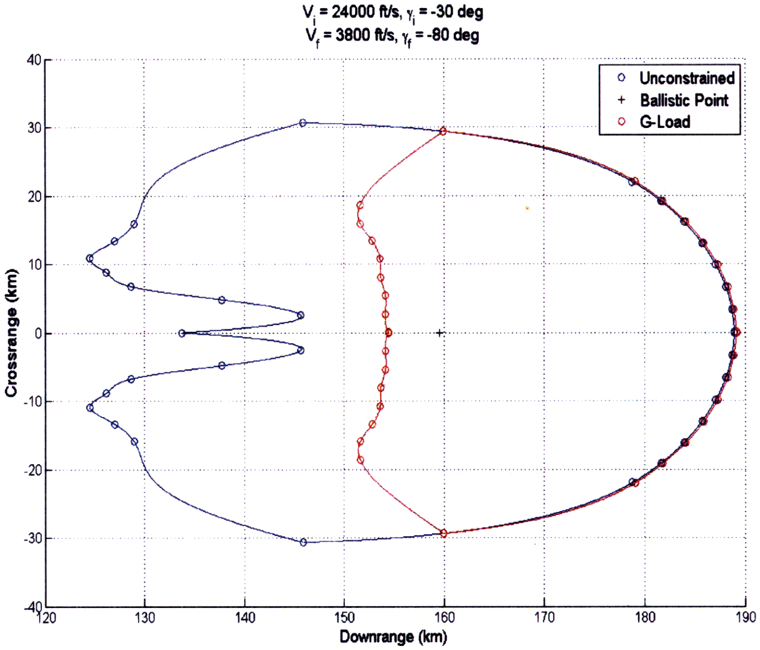

Figure 6-36: *The footprint with no path constraints (blue), only a G-load constraint (red)*

6.8.2 Stagnation Point Heat Rate

As the vehicle enters the atmosphere at high speeds, it experiences drag and loses energy. Most of the energy lost is given up as heat. At the high speeds which are typical of all re-entry vehicles (including the one being studied), this heating can be very significant. The heat shield of the vehicle is usually designed to be able to handle a certain maximum heating rate, beyond which the incoming heat can no longer be dissipated quickly enough to maintain the temperature of the vehicle. The heating rate is typically maximum at the stagnation point of the vehicle. Therefore the stagnation point heat rate will be considered in this section. A stagnation point heat rate of 23 $Btu/s/ft^2$ was used.

The trajectories that are most effected by the heat rate constraint are the minimum uprange trajectories. As we have seen before, the unconstrained minimum uprange trajectories violate the heat rate constraint. Therefore, adding this constraint will force the trajectories to look different. The vehicle would have to lose much of its speed while flying through the upper atmosphere before descending into the lower atmosphere, because the combination of high speed and high density would drive up the heat rate (see heat rate model, Equation 4.4). To do this, the vehicle would have to fly a longer trajectory. The additional downrange gained because of this can be minimized with out-of-plane maneuvers, but some downrange is gained and the size of the footprint shrinks.

On the other hand, the maximum downrange trajectories are not affected by the heat rate constraint, since the heat rate limit was not reached by the unconstrained trajectories.

Both effects are clearly seen in Figure 6-37, which shows the footprints in the unconstrained case, the G-Load constrained case, and the G-Load and heat rate constrained case. With the addition of each new constraint, the size of the footprint shrinks.

Since the stagnation point heat rate depends on the speed, a trajectory with slow speed will not be affected by the heat rate constraint. This is clear from studying Figure 6-38, which shows the landing footprint for initial conditions $V_i = 21500$ ft/s, $\gamma_i = -10$ deg. Even when the stagnation point heat rate constraint is added, the footprint is the same as the unconstrained case. This is because of the slow speed of the trajectory. On the other hand, the G-Load constraint does effect the uprange trajectories, because the vehicle starts at a shallow initial γ (of -10 deg) and needs to turn to get to its terminal γ constraint of -80 deg.

Thus in the shallow but slow trajectories, the G-Load is more constraining.

But as Figure 6-37 and Figure 6-39 show, as the trajectories get faster, the heat rate becomes the more constraining factor - the heat-rate constrained footprint is smaller than (and enclosed by) the G-Load constrained footprint.

However, it is not just the speed that is important - the initial γ also matters. If the vehicle re-enters the atmosphere at a very steep angle, it will not spend enough time in the low-density upper atmosphere to lose significant speed. Thus it will still be going fast when it begins to see the higher densities of the lower atmosphere, and this combination drives up the heat rate. In fact, for very steep initial γs, the trajectory might not even be feasible. This is in fact the case for $\gamma_i = -30$ deg. Both the $V_i = 21500$ ft/s and the $V_i = 24000$ ft/s cases are infeasible when $\gamma_i = -30$ deg. For such a steep γ_i, a feasible trajectory would have to be even slower than 21500 ft/s. Exactly what this "maximum feasible speed" is will be discussed when we introduce the concept of a "reverse footprint" later.

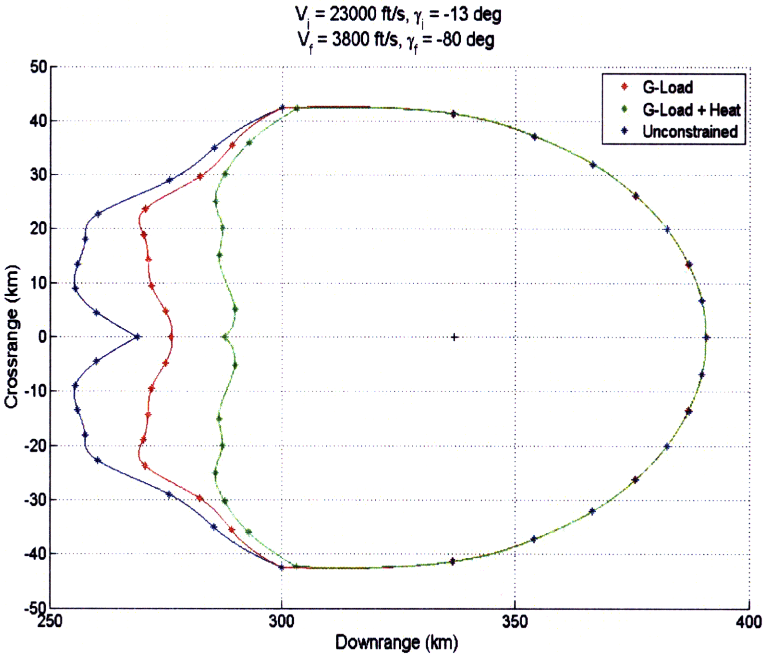

Figure 6-37: *Footprint with path constraints*

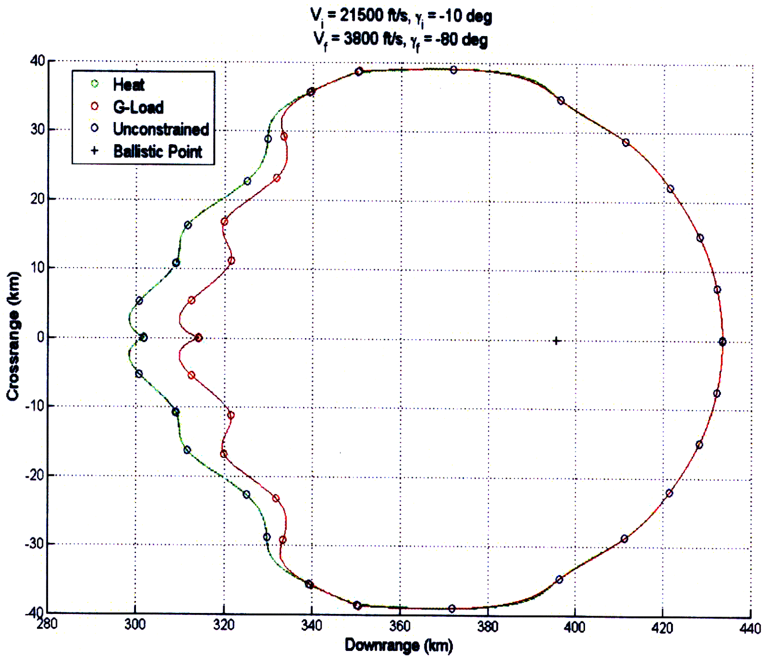

Figure 6-38: *Footprint with path constraints*

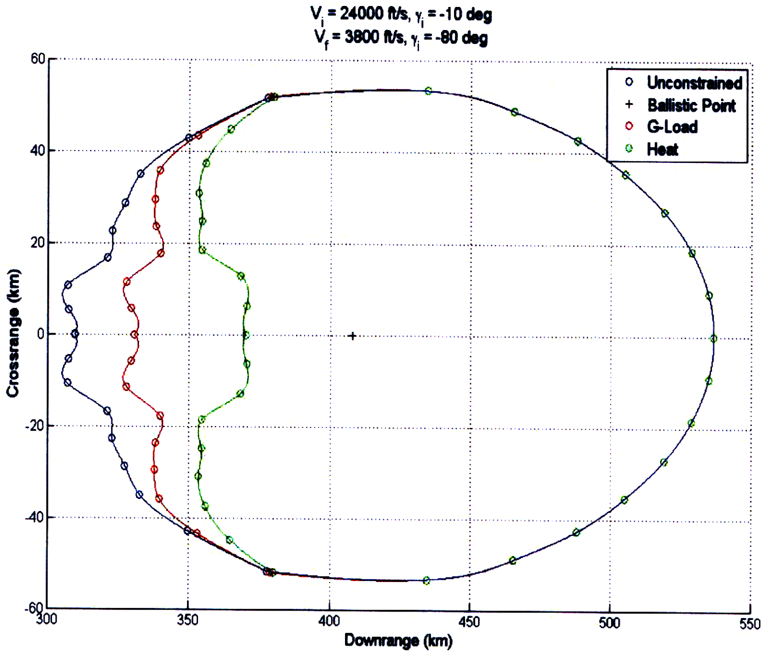

Figure 6-39: *Footprints with path constraints*

Chapter 7

Submunitions

Until now, we have looked at only one of the two missions this re-entry vehicle must perform. The Earth Penetrator mission has relatively difficult terminal conditions, since it must fly at 3800 ft/s (about Mach 3) at very low altitudes, and must achieve a steep terminal flight path angle of approximately -90 deg (the exact condition will depend on the terrain, as we have seen before). Since the vehicle needs most of its energy to maneuver to -90 deg, and needs to retain a lot of its kinetic energy, the amount of energy available for other maneuvers is very limited. If these constraints could be relaxed, the vehicle would have more energy to maneuver and thus a bigger footprint.

For the Submunitions mission, the terminal speed is constrained to be 1300 ft/s and the terminal flight path angle 0 deg, at an altitude of 3 km. Therefore the terminal speed for the Submunitions case is a factor of 3 lower than for the Earth Penetrator case. Similarly, it is easier to reach a flight path angle of 0 deg from initial flight path angles of -10 and -13 deg, than it is to reach -90 deg. Therefore, we can expect that the landing footprint for the Submunitions case is going to be bigger than the landing footprint for the Earth Penetrator case.

Figure 7-1 shows the footprint for the Submunitions case with initial conditions $V_i = 21500$ ft/s and $\gamma = -10$ degrees. The maximum downrange is more than 1600 km. This is clearly much greater than the Earth Penetrator case. We examine how the vehicle achieves such a large footprint by examining the three special cases: maximum downrange, minimum uprange, and maximum out-of-plane angle.

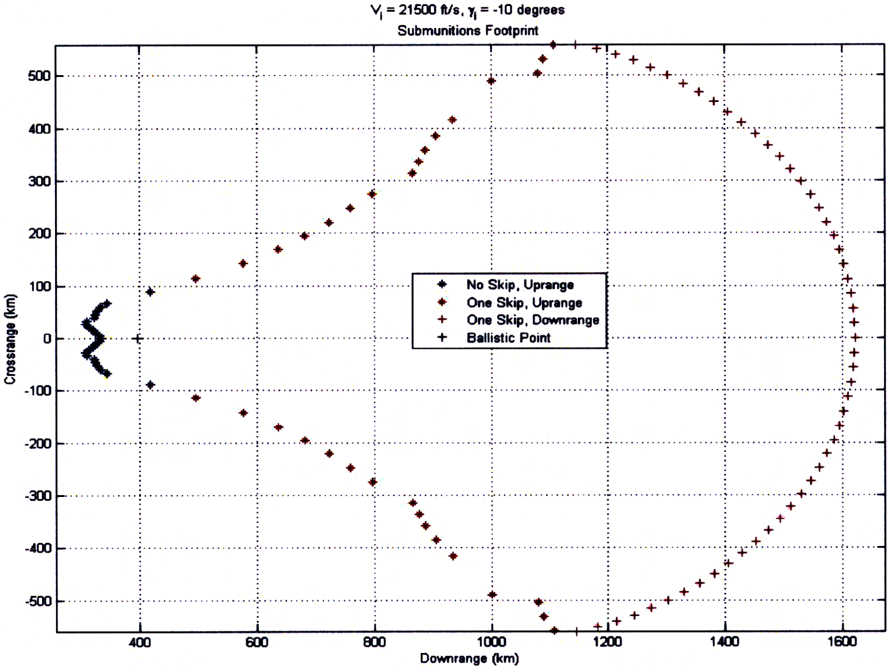

Figure 7-1: *The footprint for a submunitions mission with initial conditions* $V_i = 21500$ *ft/s and* $\gamma = -10$ *degrees*

7.1 Maximum Downrange

We see how the vehicle can travel more than 1600 km by looking at the trajectory for the maximum downrange case, shown in Figure 7-2. The vehicle achieves the large downrange distance by "skipping" - upon re-entry, the vehicle uses its lift to accelerate upwards and gain an upwards velocity. This velocity carries it out of the atmosphere again, where it flies along a ballistic, parabolic trajectory. As we can see in Figure 7-4, the speed stays almost constant during this portion of the trajectory because there is very little drag at high altitudes. At the same time, the vehicle gains about 1000 km downrange during this portion. Therefore, by skipping, the vehicle has essentially gained 1000 km downrange distance for negligible loss of energy. The vehicle then re-enters the atmosphere, but since some energy was lost in the first skip, it no longer has enough energy to take another skip. Therefore it now descends into the lower atmosphere and maneuvers with whatever energy it has left to meet its terminal altitude, speed and flight path angle conditions.

An important thing to note is that if the vehicle had enough energy left after its first skip, it could potentially skip a second time. As the initial speed V_i is increased, this could - and in fact does - happen. We discuss this in detail in another section.

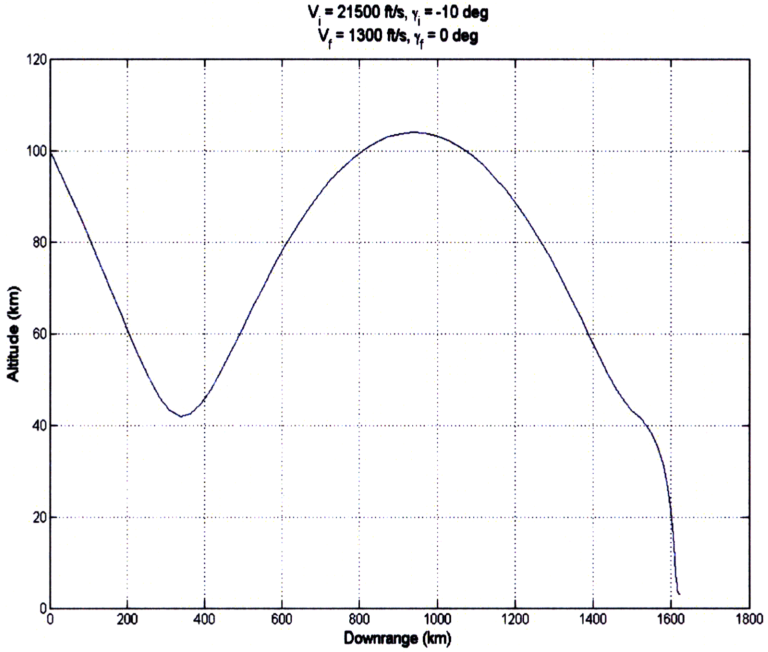

Figure 7-2: *A submunitions trajectory with a skip*

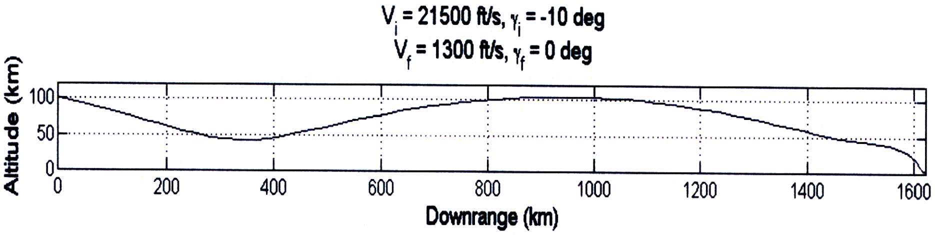

Figure 7-3: *A scaled representation of the maximum downrange trajectory showing the large downrange distance acquired by skipping*

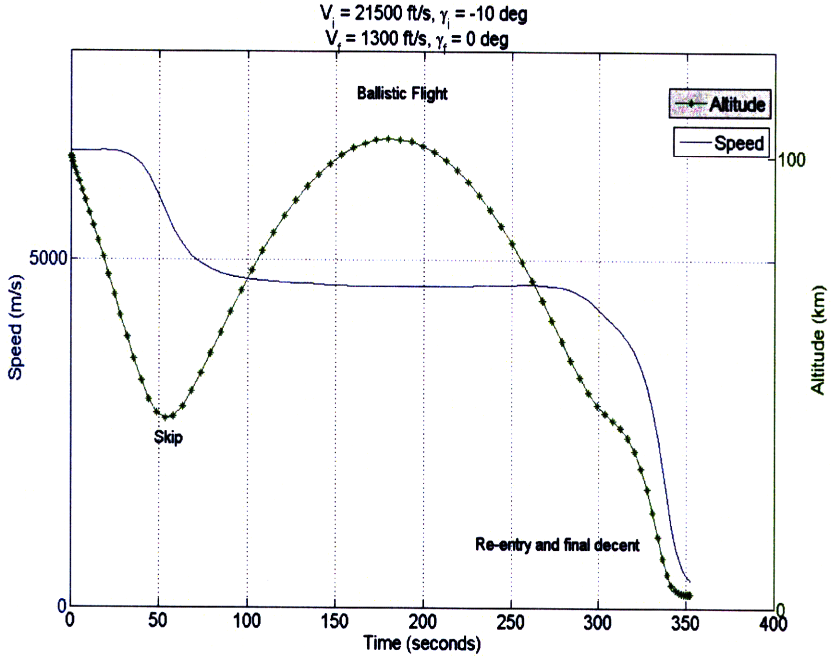

Figure 7-4: *The speed and altitude for a submunitions trajectory*

7.2 Maximum Out-of-plane Angle

As we see in Figure 7-1, the vehicle now has the ability to travel more than 500 km crossrange. This ability comes from the fact that the vehicle can simultaneously turn and skip. The vehicle cannot maneuver at the top of its skip trajectory because the atmosphere is too thin at high altitudes to permit any significant control authority. However, at the bottom of the skip, when the vehicle is at low altitudes and in relatively dense atmosphere, the vehicle has enough control authority to change its direction of travel. Thus the vehicle uses its available lift to simultaneously accelerate upwards and turn to change its heading. The low-drag, ballistic part of the trajectory now takes it not only far downrange, but crossrange as well. This is seen in Figure 7-5, where the groundtrack shows that the vehicle travels at constant heading during both the initial descent and during the ballistic part of the skip trajectory. It is only during the relatively brief period it spends in the lower atmosphere that the vehicle turns to point itself in a direction that will allow it to travel long crossrange distances.

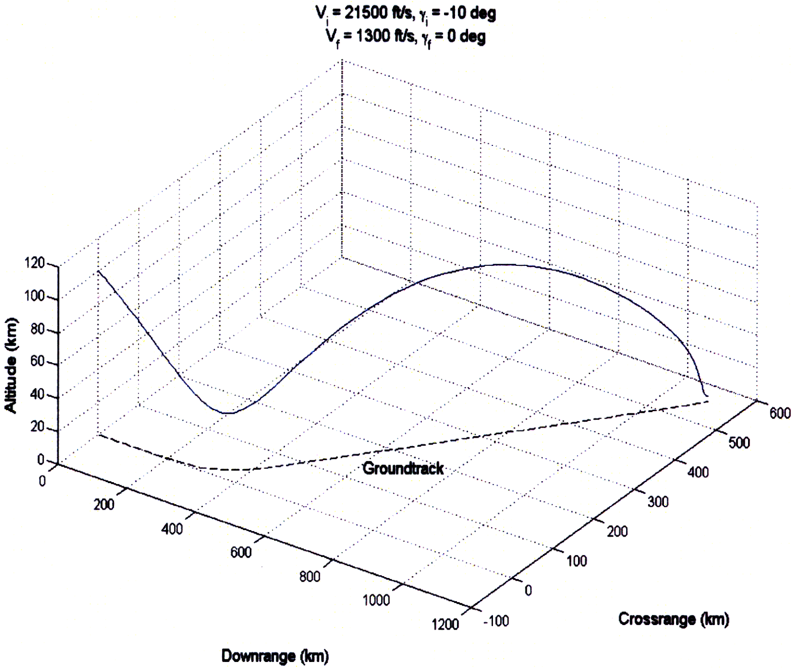

Figure 7-5: *The maximum out-of-plane trajectory for a submunitions mission with initial conditions* $V_i = 21500$ *ft/s and* $\gamma = -10$ *degrees*

7.3 Minimum Uprange

Since the vehicle must lose much more energy in the submunitions case than in the Earth-penetrator case, the vehicle cannot hit targets that are very close - it simply cannot lose enough speed fast enough to meet the terminal speed constraint. As a result, the minimum uprange is now longer - and as we see in Figure 7-1, it is about 300 km. The vehicle achieves these upranges by flying directly into the lower atmosphere (without lofting or skipping) and descending to altitudes *below* the terminal altitude of 3 km (see Figure 7-6. At these low altitudes, the atmospheric density (and therefore the drag) are much higher, allowing the vehicle to slow down quickly without accumulating much downrange. The reason why the vehicle does not descend even lower into the atmosphere (and therefore lose speed even faster) is because of the G-load constraint. Given the vehicle's high speed, had it descended any farther down, the drag force would have exceeded the limit set on the maximum G-load. From Figure 7-7, we see that the vehicle descends as far into the atmosphere as its maximum G-load limit will permit - hence the long plateau at the maximum of 55gs, coinciding with the time spent flying at low altitudes. Towards the end, the vehicle climbs back up to the 3 km altitude that the Submunitions deployment mission requires.

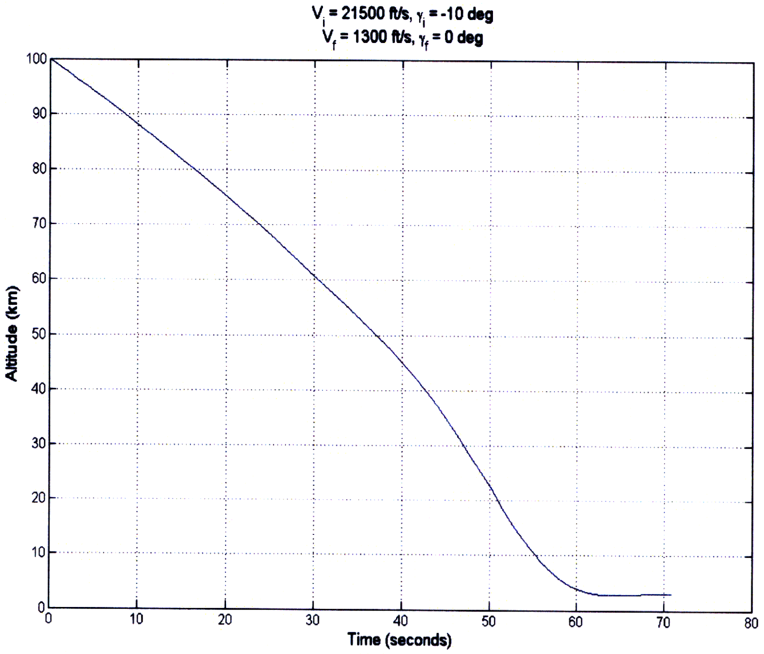

Figure 7-6: *The minimum uprange trajectory for a submunitions mission*

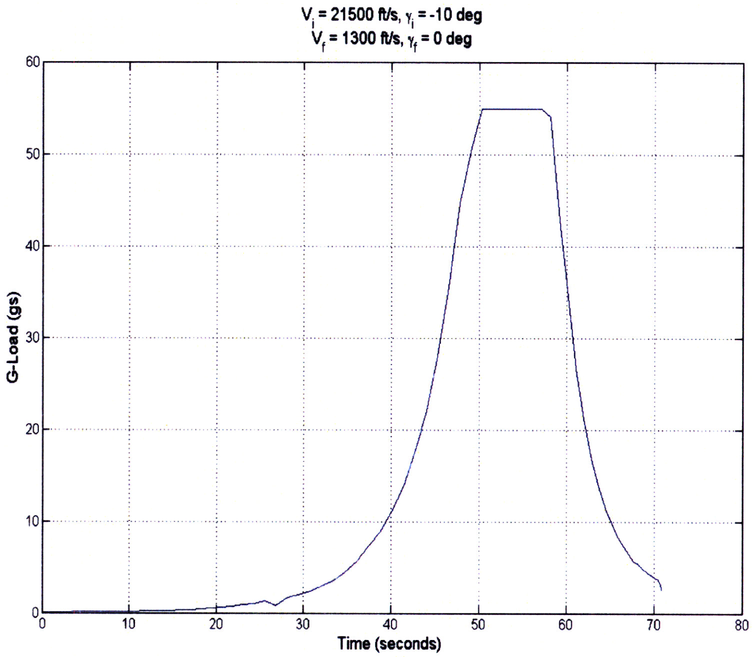

Figure 7-7: *The G-Loading for the submunitions minimum uprange trajectory*

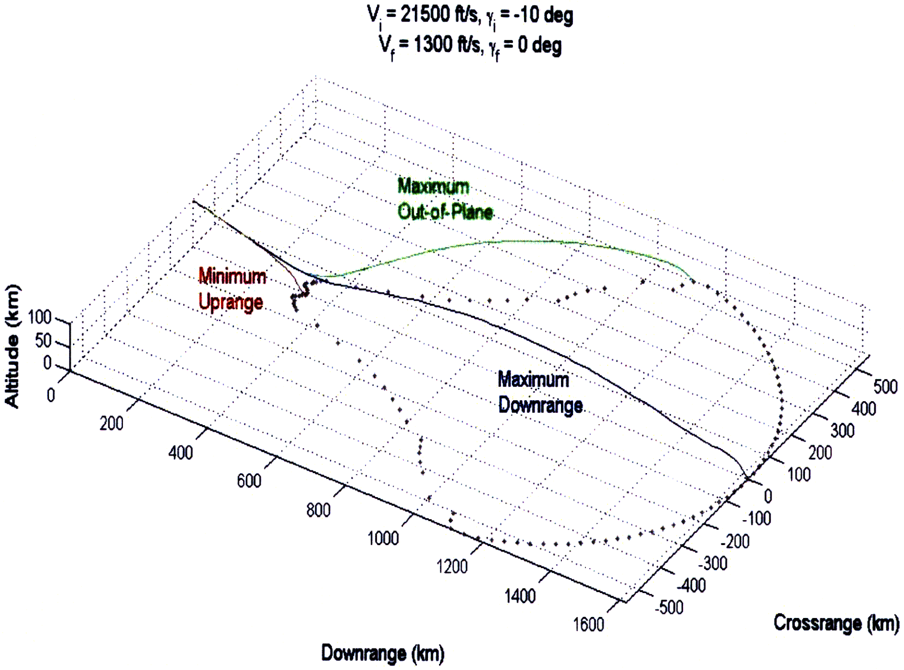

Figure 7-8: *The maximum downrange, minimum uprange and maximum out-of-plane trajectories shown on a scaled plot of the landing footprint*

7.4 Double Skip Trajectories

As we have mentioned previously, if the vehicle starts with enough initial energy (faster speed, for instance) the vehicle might be able to skip not just once but twice. We saw in the previous case that with an initial speed of $V_i = 21500$ ft/s and an initial altitude of 100 km, the vehicle does *not* have the energy for two skips. However, when we increase the speed - to 24000 ft/s, for instance - we see that the vehicle can skip twice and go much farther downrange. This is seen in the footprint shown in Figure 7-9.

The footprint shown below has three distinct regions. The first is the one-skip region (shown in blue). If the vehicle were constrained to have $\gamma \leq 0$ at all times, there will be no skips - and the resulting footprint would be much smaller. This is the region labeled "No skip". Note that the maximum downrange in this case is less than 800 km. This footprint is characteristically not very different from the Earth-Penetrator footprint.

When the restriction on the the flight path angle is removed, the vehicle can now skip. Since the initial energy is great enough to permit two skips, the vehicle can actually travel much farther and reach locations that would not be reached with just one skip. This "two skips" region (marked in green) extends down to more than 2400 km downrange. The "one skip" region, in between the "no skip" region and the "two skips" region, is the region that can be reached with just one skip (marked in red). Note that the "one skip" and the "two skips" regions overlap, since there is a large region that can be reached with either one skip or two. This is seen in Figure 7-10, where the same location (14 degrees out-of-plane, maximum downrange) is reached either by following a single-skip trajectory or a two-skip trajectory.

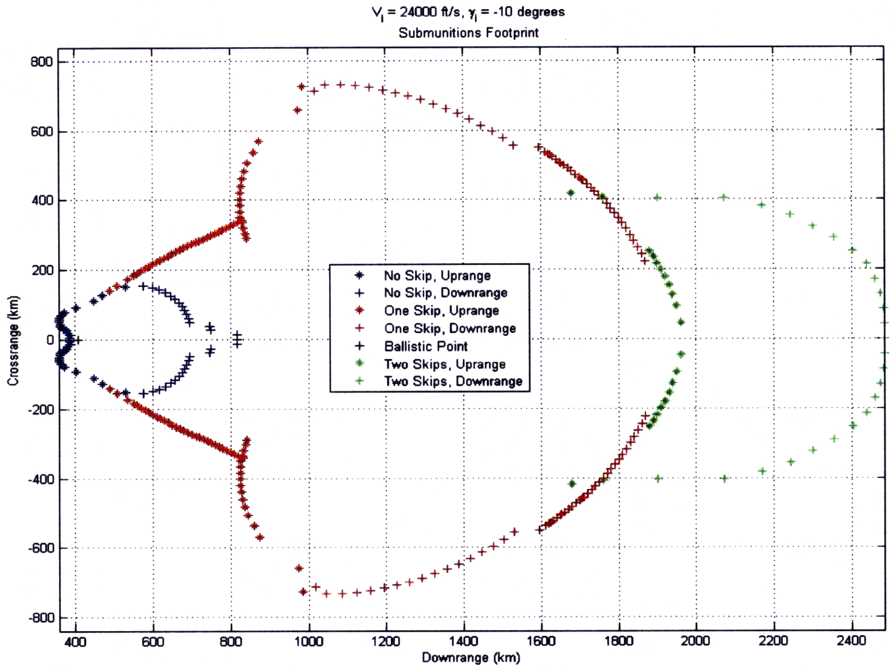

Figure 7-9: *The footprint for a submunitions trajectory with initial conditions* $V_i = 24000$ *ft/s and* $\gamma = -10$ *degrees*

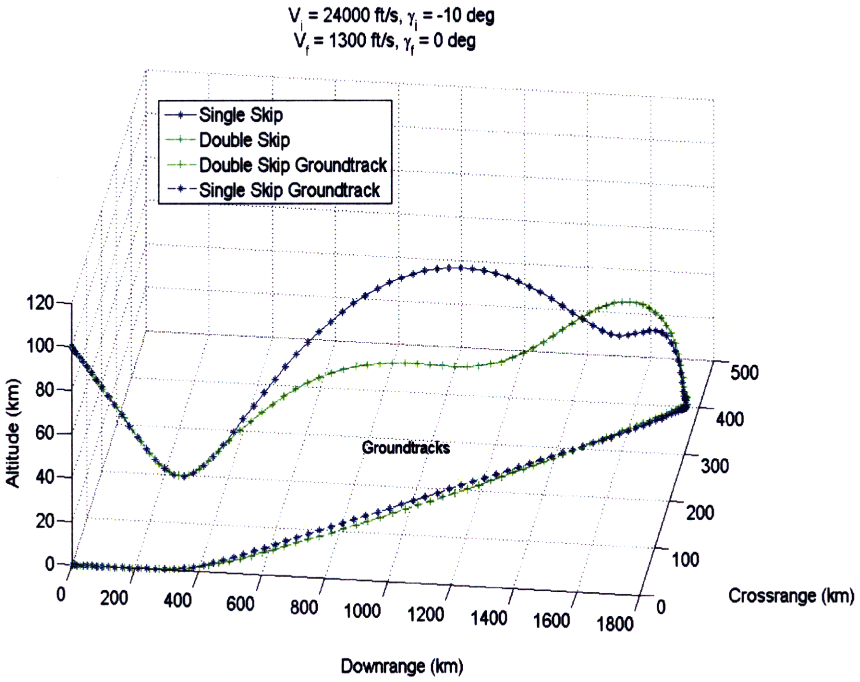

Figure 7-10: *The footprint for a submunitions trajectory with initial conditions* $V_i = 24000$ *ft/s and* $\gamma = -10$ *degrees*

To understand how the trajectories change as downrange is increased and out-of-plane angle is increased, we look at the following four cases. These cases were chosen to be at those locations where the footprint in Figure 7-9 seems to change significantly.

- **Cases 1A** and **1B**, as shown in Figure 7-11, are chosen to be on either side of the point where the footprint shows a "cusp".
- **Cases 2A** and **2B** are chosen to be on either size of the point at which the single-skip portion of the footprint (red) coincides with the double-skip portion (green).
- **Cases 3A** and **3B** are chosen to be on either side of the location where single-skip trajectories transition into double-skip trajectories.
- **Case 4A** and **4B** are chosen to be on either side of the location where no-skip trajectories transition into single-skip trajectories.

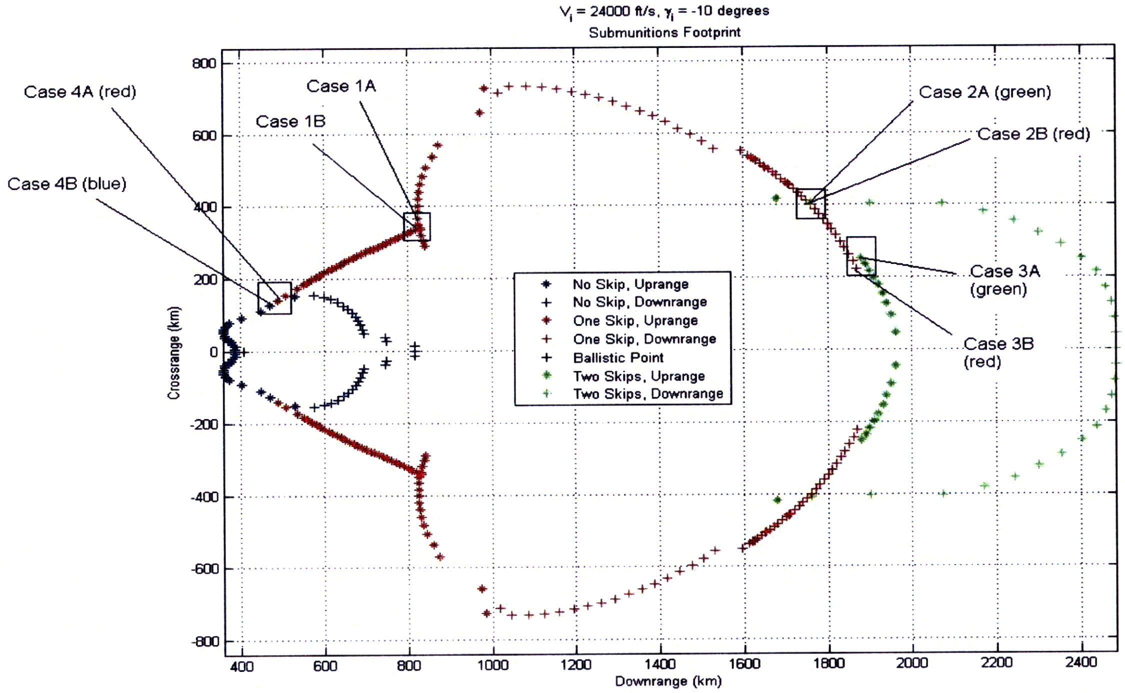

Figure 7-11: *The footprint for a submunitions trajectory with initial conditions* $V_i = 24000$ *ft/s and* $\gamma = -10$ *degrees*

7.4.1 Case 1

As shown in Figure 7-11, Case 1 is the point where the footprint shows an abrupt change in slope. We see that this happens between trajectories that are approximately 20 degrees out-of-plane and 21 degrees out-of-plane. The footprint changes in this region because 20 degrees out-of-plane can be reached without a skip, while 21 degrees out-of-plane can be reached only by skipping. This is seen in Figure 7-12, which shows that the 20 deg out-of-plane trajectory has no skip while 21 deg out-of-plane does have a skip. This results in a 300 km downrange gap between the 20 deg out-of-plane case (the maximum out-of-plane for the no-skip footprint) and the 21 deg out-of-plane case (with a skip). However, points in between these locations can be reached too - in these cases, the vehicle "skips" (i.e. $\gamma > 0$ at some interval), but uses less energy in skipping, and therefore travels less distance downrange than the 21 deg out-of-plane skip. This is seen in Figure 7-13, where the transition from 20 deg out-of-plane to 21 deg out-of-plane occurs as the skip distances gradually increase. The transition is also seen in Figure 7-14, which the transition from no-skip behavior to one-skip behavior. The trajectories begin with a very slight "skip". The trajectory is classified as a "skip" because $\gamma > 0$ at some point in the trajectory, but in reality the "skip" does not add much downrange. As the magnitude of this skip gets greater, and the downrange gained gets longer, we see the transition to "full" skipping behavior seen in Figure 7-13. Since this transition happens within a difference of 1 degree out-of-plane, the transition seems abrupt and results in the "cusp" in the footprint.

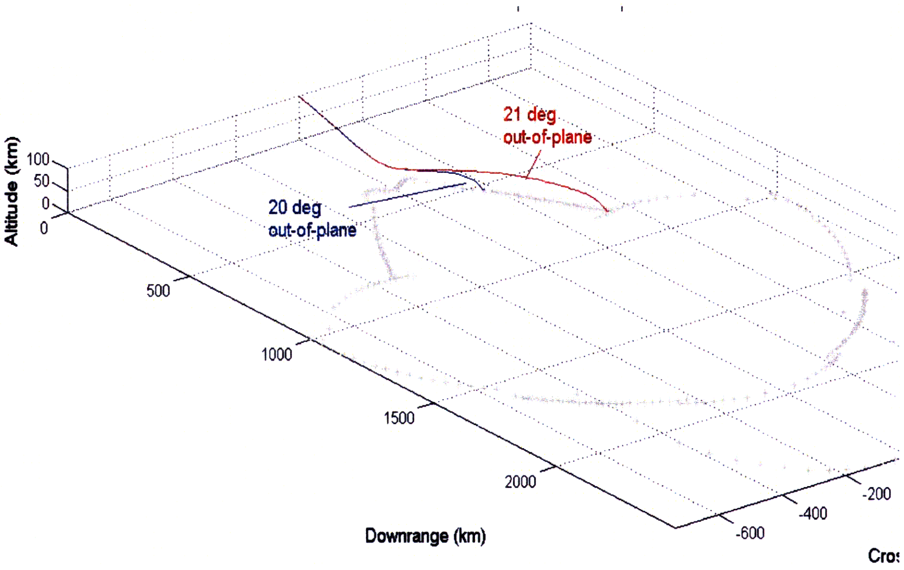

Figure 7-12: *The downrange and altitude for trajectories on either side of the uprange "cusp", showing that the trajectories show no significant change in general behavior*

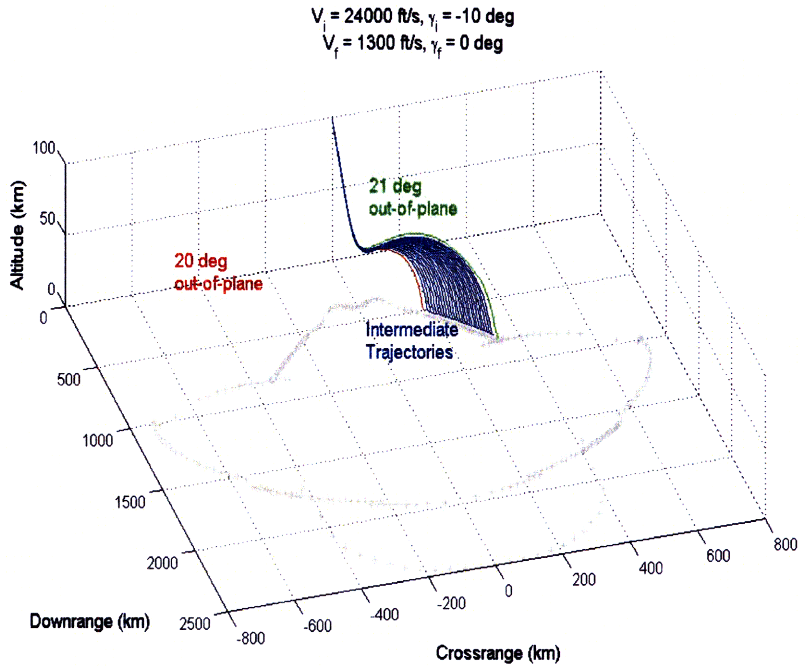

Figure 7-13: *The transition from 20 deg to 21 deg out-of-plane, which shows the transition from trajectories with no skips to those with a skip. The altitude axis on this plot has been exaggerated to show the skips clearly*

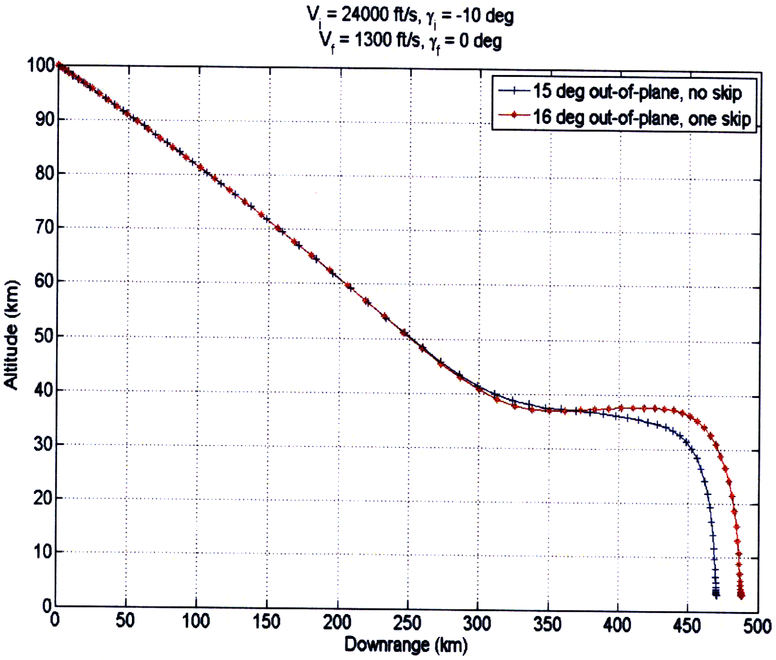

Figure 7-14: *The downrange and altitude on either side of the transition from skipping to non-skipping behavior (Cases 4A and 4B)*

7.4.2 Case 2

The next case we look at is a case we have seen previously, where the "one skip" region and the "two skips" regions intersect. As seen in Figure 7-10, the intersection occurs because there are some locations on the ground which can be reached with a single skip as well as a double skip. This is seen clearly again in Figure 7-15 which shows the one of the intersection between the one-skip footprint and two-skips footprints. This change in behavior explains the second "cusp" in the footprint in Figure 7-9.

Note that the vehicle manages a second skip by not skipping as much on the first skip - i.e. it saves some of its energy during the first skip so that it may take a second skip. Also, since the vehicle has already lost some energy on the first skip, it does not have as much energy to maneuver after this skip - hence the area of the "two skips" region is much smaller than the area of the "one skip" region. If the vehicle had even more energy, the second skip region would grow larger, and it is likely that a third skip would also be possible. This case is not examined in this work, but we will see that when the spherical shape of the Earth is accounted for, the "two skips" area increases dramatically. This is because the surface of the Earth is curving away from underneath the vehicle, thus decreasing the effort required to travel downrange. This case is investigated later.

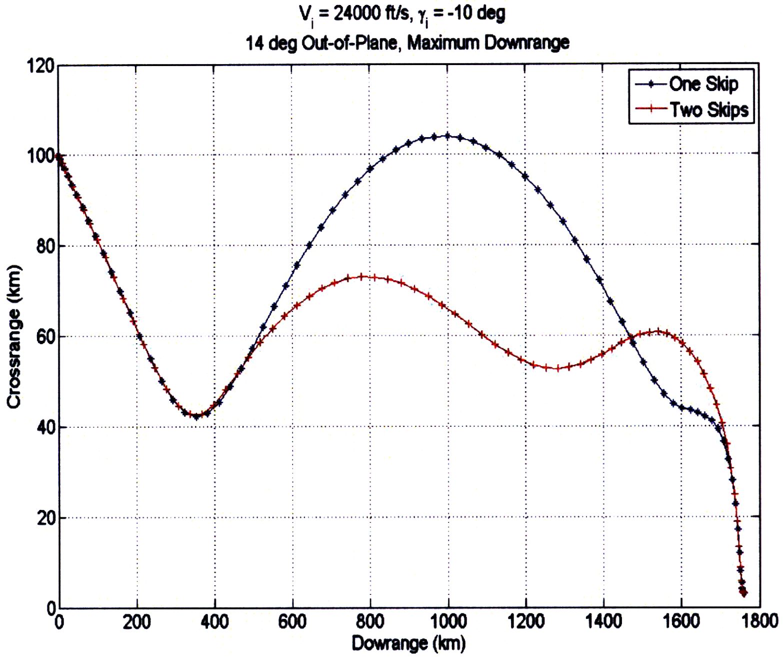

Figure 7-15: *The downrange and altitude for trajectories for Cases 2A and 2B. This shows that there are some points which can be reached by trajectories that have different characteristics*

7.4.3 Case 3

Next, we look again at the case where the one-skip trajectory region and the two-skip trajectory region merge, but this time we look at the trajectories with small out-of-plane angles. In Figure 7-16, we see that the transition from one-skip trajectories to two-skip trajectories is continuous. The trajectories look very similar, but one is classified as one-skip because it crosses the $\gamma = 0$ threshold only once, while the other does so twice. However, the second crossover across the $\gamma = 0$ threshold is very brief - i.e. the magnitude of the second skip is very small. As the downrange distance targeted becomes greater, the vehicle spends less energy on the first skip and more on the second skip, as seen in Figure 7-17. Thus the transition from the one-skip region to the two-skip region is continuous.

Comparing Figures 7-16 and 7-15, we see that the difference between the one-skip and two-skip trajectories is greater for larger out-of-plane angles. This is seen more clearly in Figure 7-18. This is because the vehicle has to spend some energy to turn to its out-of-plane angle. Therefore, after one large skip, the vehicle no longer has the energy to make a second skip. The only way the vehicle can make a second skip is by reducing the energy spent on the first skip. On the other hand, if the vehicle spends very little energy in turning (for a small out-of-plane angle), the vehicle can afford to take a large first skip, followed by a small second skip. The vehicle *could* also take a small initial skip, and then a larger second skip and get to the same location. If the objective were to minimize the maximum G-load, this is most likely the trajectory the vehicle would choose. If the objective were to minimize the time, for instance, the vehicle would take a large first skip, travel at high altitudes (with low drag) and get to its target faster. This shows a basic principle that in optimal control, the problem does not have a unique solution, but varies for different objective functions.

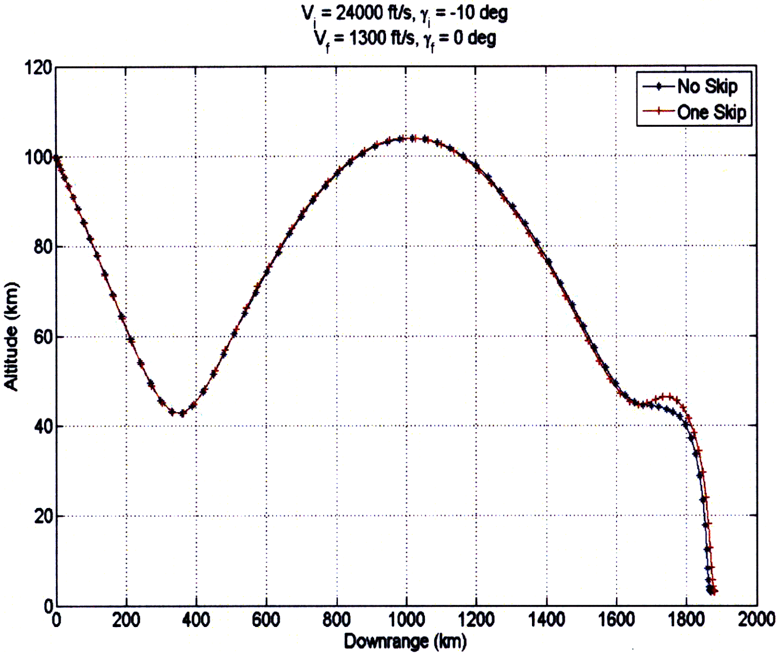

Figure 7-16: *The downrange and altitude for two trajectories on either side of the transition from single-skip behavior to two-skips behavior (Cases 3A and 3B)*

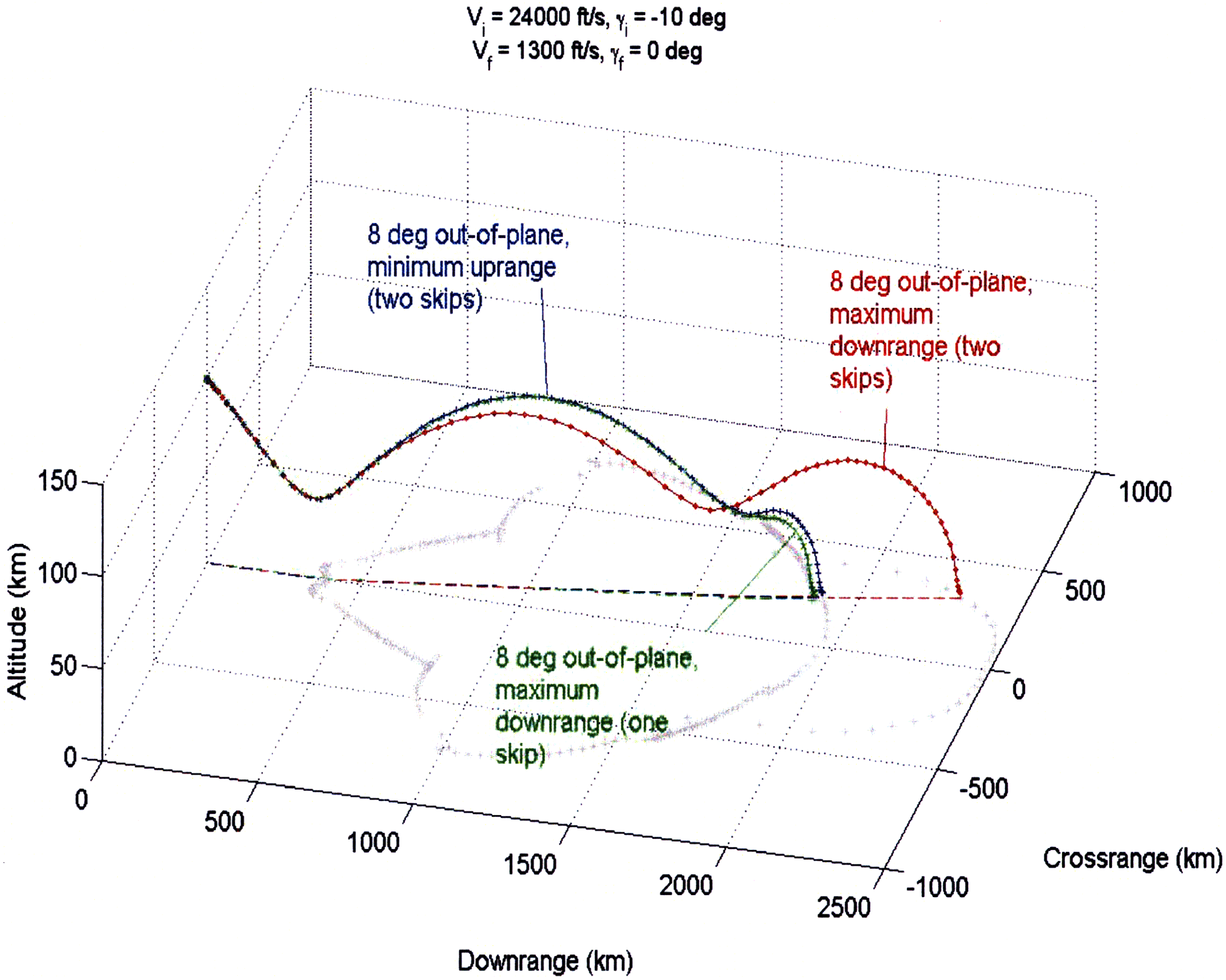

Figure 7-17: *The transition from one-skip trajectories to two-skip trajectories for smaller out-of-plane angles*

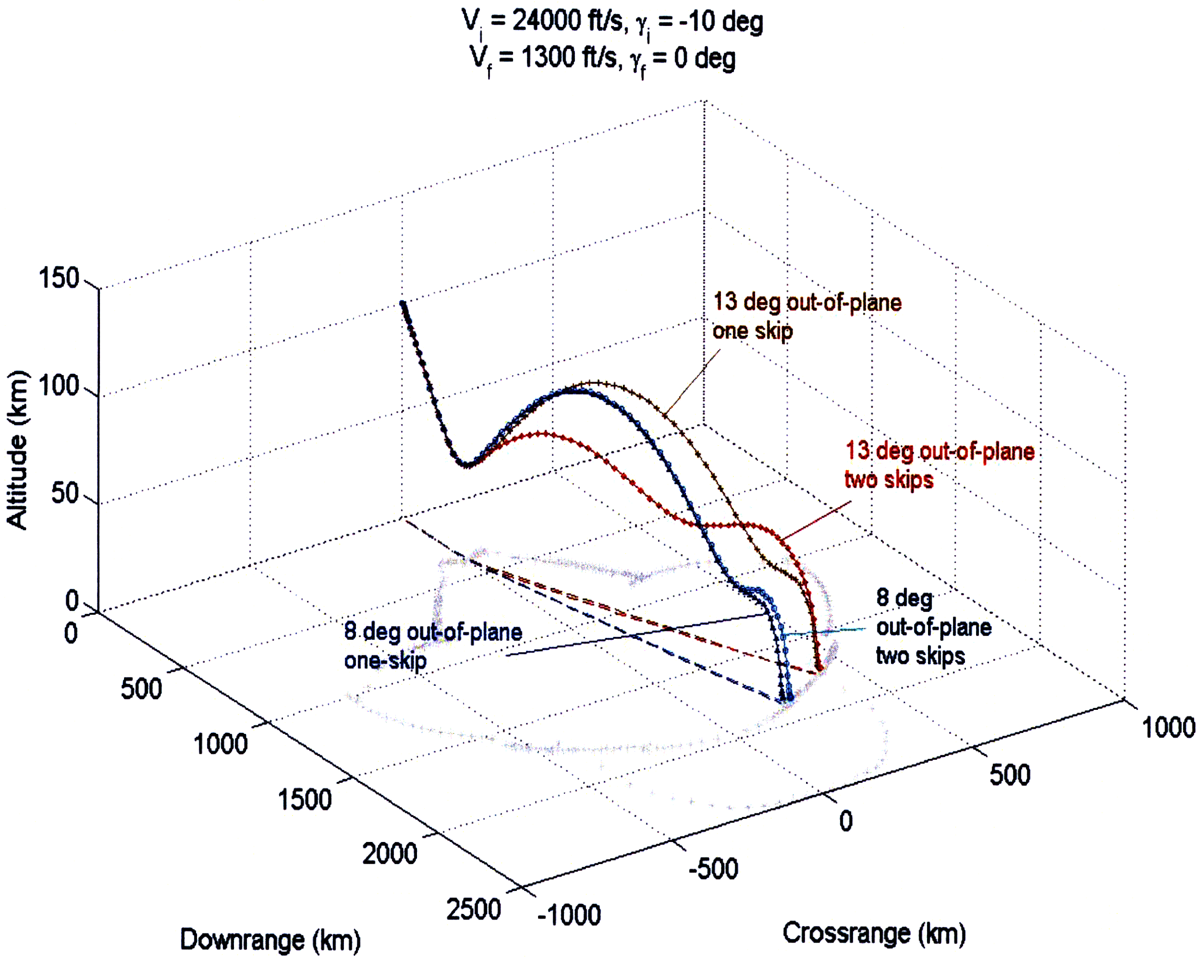

Figure 7-18: *The difference between one-skip and two-skip trajectories grows as the out-of-plane angle is increased*

Chapter 8

Reverse Footprint

Until now, we have addressed the forward problem, which may be phrased as follows: Given a set of initial conditions, what are the sets of terminal conditions that can be reached. We now try to solve the reverse problem - for a given set of terminal conditions, what are the set of initial conditions from which those terminal conditions can be achieved.

First, we view the forward problem in a slightly more general way. In the forward problem, both the initial and terminal conditions are described by six states - three for terminal position and three for terminal velocity. The initial conditions are all fixed, and the terminal angle of attack is constrained to be 0. What we would like to know is the set of all terminal conditions that can be reached from the given set of initial conditions, with final angle of attack $\alpha_f = 0$. This set of terminal conditions can therefore be seen as a 6-dimensional subspace, giving all positions and velocities that can be achieved from the initial conditions. However, to make the problem more tractable, and to accomplish the stated missions, we fixed four of these states - the altitude (set to 0 for the Earth penetrator, 3 km for the Submunitions), the speed (3800 ft/s and 1300 ft/s), the flight path angle (unconstrained, -90, -80, -70, -60 deg and 0 deg) and the heading angle (unconstrained, 0 deg, 15 deg, 30 deg, 60 deg, 90 deg). Therefore, the 6-dimensional subspace was reduced to a 2-dimensional subspace in downrange and crossrange, which is exactly what we had previously called the "landing footprint".

For the reverse problem, we again have the same six states (position, velocity) at the initial and terminal conditions. However, this time the terminal conditions are fixed, and we would like to find the set of all initial conditions from which these terminal conditions can be met. Therefore, there is another 6-dimensional subspace at the initial time which gives all possible positions and velocities from which the given terminal conditions could be achieved. Again, the problem is made more tractable by fixing some of these initial conditions - in particular, the downrange (set to 0), altitude (at 100 km), crossrange (whose initial value is set to 0 km), and heading angle (set to 0 deg). This leaves us with a 2-dimensional subspace (a 2-dimensional slice of the 6-dimensional subspace) in speed and flight path angle that gives us all initial speeds and initial flight path angles (for the chosen initial downrange, altitude, crossrange and heading angle) from which the given terminal conditions can be met. This 2-dimensional subspace is what will be called the "reverse footprint" throughout this work.

Let us next look at the physical reasons why the reverse footprint is a closed space and not unbounded. We look at the case where the target is 350 km downrange from piercepoint. First, assume that the initial speed is also fixed. Thus the only state allowed to vary is the initial flight path angle. If the vehicle were to come in at a very shallow flight path angle, it would "overshoot" the target - it simply would not have the control authority (essentially lift) to turn and reach the target. Thus there is an upper limit on the flight path angle. On the other hand, if it came in too steep, the vehicle would "undershoot" the target - it would not have the control authority (lift) to loft itself enough and reach the target while simultaneously meeting its terminal conditions. Thus there is also a lower bound on the flight path angle. Both these cases are shown in Figure 8-1.

Now assume that the flight path angle is fixed, and the initial speed is allowed to vary. If the vehicle were starting at a very low speed, it would not have the energy to reach the target with the required terminal speed. Thus there is a lower bound on the initial speed. If the vehicle were traveling very fast, it might not be able to lose enough speed before reaching its target, and would thus overshoot the terminal speed requirement. Thus there is an upper bound on the initial speed. Furthermore, the G-loading and Stagnation point heat rate constraints could constrain this maximum speed even more. But ignoring these path constraints for now, we see in Figure 8-2 that the terminal conditions alone are enough to bound the minimum and maximum speed for a fixed initial flight path angle.

Since we now know that for every fixed initial flight path angle there is a minimum and maximum initial speed, and there is a minimum allowed initial flight path angle and maximum allowed initial flight path angle, we can trace out the "reverse footprint" of the vehicle for fixed terminal conditions. We allow the flight path angle γ_i to vary from the minimum to the maximum, and for every γ we find the maximum and minimum initial speeds. Taken together, these maxima and minima give us the reverse footprint. This is seen in Figure 8-3, for a target whose location is fixed at 350 km downrange from piercepoint (where the vehicle is initially at 100 km altitude).

In Figure 8-3, we see that we get a certain reverse footprint (outlined in green) when we ignore the stagnation point heating and the G-load constraints. When we add in the stagnation point heat rate limit, we see that the high initial speeds are no longer feasible - and we know this to be physically true, since fast trajectories encounter much greater heat rates than slow ones. Then when we add the G-load constraint, we see that some of the fast and shallow trajectories get cut. This is because if the vehicle started by traveling fast and shallow, it would have to execute a very high-g turn to be able to reach its target. When a G-load constraint is imposed, these high-g turns become infeasible, and thus these initial conditions no longer lie within the reverse footprint.

The reverse footprint presented in Figure 8-3 is the footprint for a target located 350 km downrange. However, if this target were farther out, the footprint would change. Specifically, some of the shallower γs would be feasible, while some of the steep γs would not be feasible. Also, some of the faster trajectories would become feasible and some of the slower ones would no longer be feasible. But the same process as described in the previous paragraph can be repeated for different target downrange distances, and the reverse footprint calculated in the same way. If all these 2-dimensional reverse footprints were "stacked up", we would get a 3-dimensional "reverse footprint", with downrange distance to target as the third dimension. When this is done, we get Figure 8-4.

Note that varying the downrange distance to the target is exactly the same as fixing the target and then changing the initial downrange, because the atmospheric model being used is independent of the downrange position. Thus Figure 8-4 is essentially a 3-dimensional slice of the complete 6-dimensional subspace of feasible initial conditions, with downrange, speed and flight path angle allowed to vary and altitude, crossrange and heading angle kept fixed.

In Figure 8-5, we look at the 3-dimensional reverse footprint down the initial speed axis. We see that for any given downrange distance, there is a wide range of initial speeds from which the target can be reached - either with a fast, steep trajectory or a slow, shallow trajectory. If flight time to target is desired to be short, a fast trajectory could be chosen. If heat rate or G-loading is to be minimized (to avoid encountering plasma, for instance) a slower trajectory could be chosen. If the objective were to ensure that the target can be reached with a wide margin for initial deployment error, an initial condition that is in the middle of the reverse footprint could be chosen. As discussed before, what we see here is that an optimal control problem has many solutions, and different objectives give different solutions.

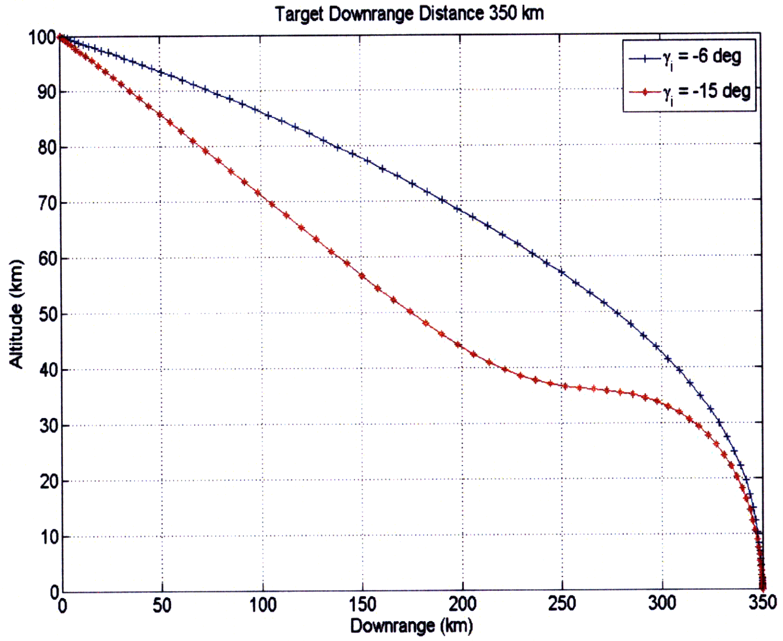

Figure 8-1: *The minimum and maximum initial flight path angles for a fixed initial speed*

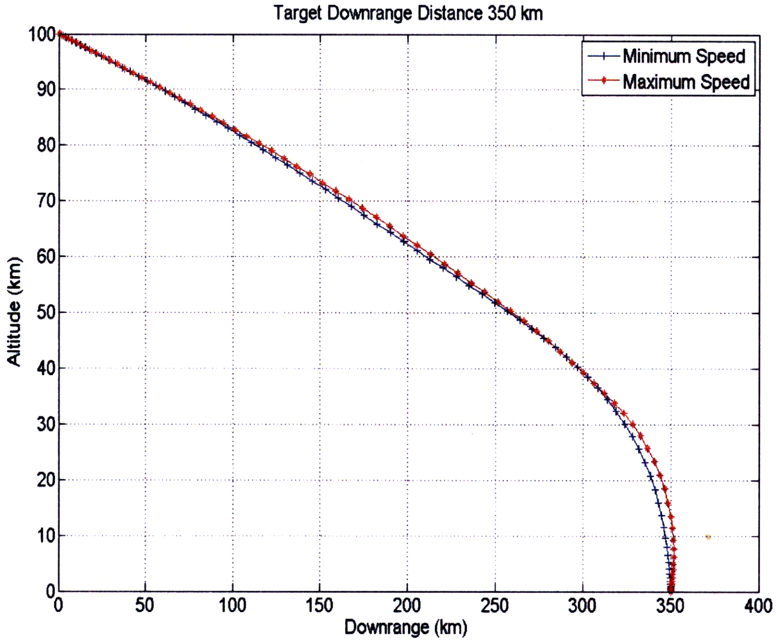

Figure 8-2: *The minimum and maximum initial speeds for a fixed initial flight path angle*

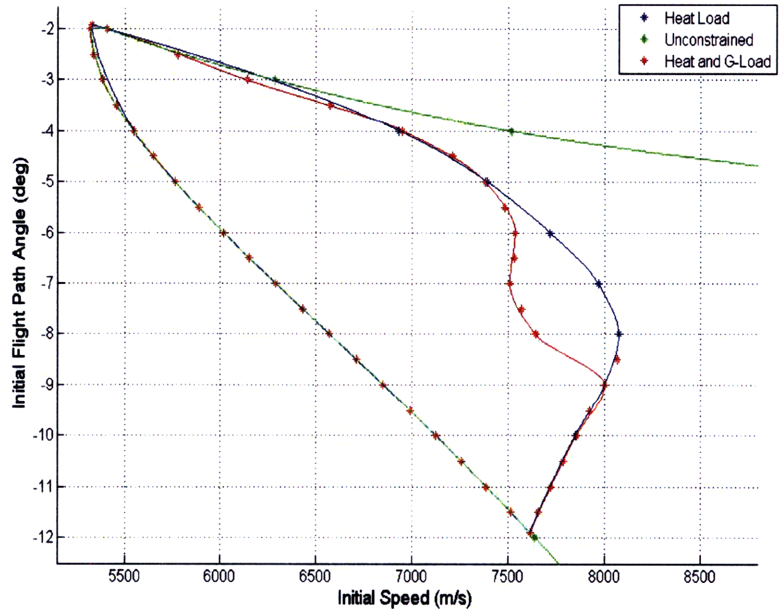

Figure 8-3: *The reverse footprint for a target located 350 km downrange*

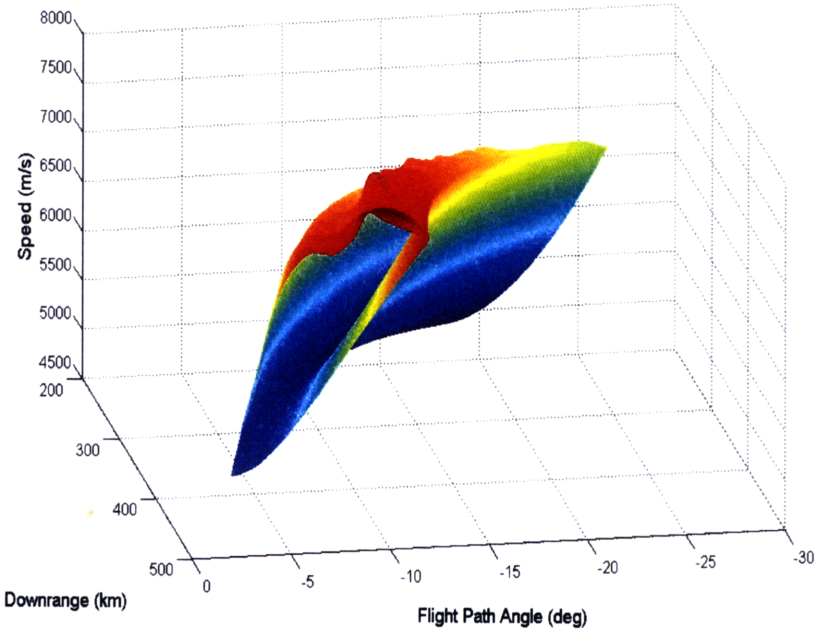

Figure 8-4: *The 3-dimensional "reverse footprint", the set of initial downrange distances, speeds, and flight path angles from which a given target can be reached*

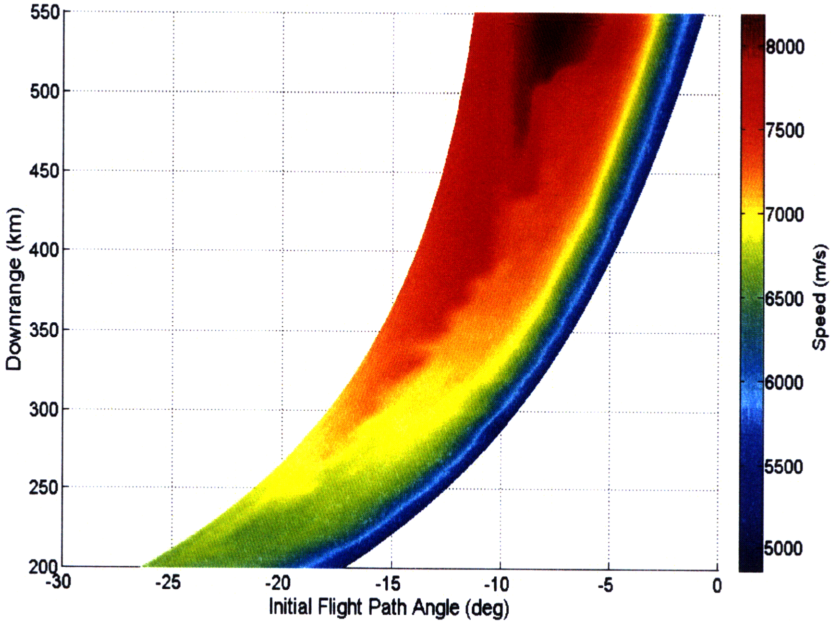

Figure 8-5: *A view of the 3-dimensional reverse footprint looking down the speed axis*

Chapter 9

Refinements

Until now, we have used a very simplified model for calculating trajectories. We have assumed that the curvature of the Earth can be ignored, and we have assumed that the aerodynamics of the vehicle can be approximated using an analytical function. In reality, the curvature of the Earth is non-zero, and the Earth and the atmosphere rotate with respect to inertial space. Furthermore, the analytical functions chosen are approximations and have errors in them - while they capture the most important non-linear behavior at hypersonic speeds, they are not exact. In this chapter we look at improvements that can be made to the models and their impact on the final trajectory.

9.1 Spherical Earth

All the results we have seen were for the flat Earth model presented in Equations 3.4. However, as we have seen, the downrange distance traveled in some of the cases is very large - over 2000 km. The longer the downrange distance traveled, the more important the curvature of the Earth. In fact, it can quickly be shown that for a 2000 km downrange distance, the surface of the Earth drops below the tangent plane by more than 292 km. Thus the curvature of the Earth is important in these cases.

Figure 9-1 shows the transition from a flat Earth model to a spherical Earth model. The flat Earth model is the same as the spherical Earth model, if we let the radius of the Earth $R_e \rightarrow \infty$. As the radius is decreased from a very large value to the actual radius of the Earth, the trajectories change. In Figure 9-1, we see the maximum downrange trajectories for the Submunitions case with initial conditions V_i = 24000 ft/s, $\gamma_i = -10$ deg. As the radius of the Earth is reduced from a very large value (the flat Earth case) to the actual radius 6378.1 km, the maximum downrange distance gets longer, until finally we see that the maximum downrange for the spherical Earth model is 1000 km longer than for the flat Earth model. This downrange extension occurs since the surface is essentially "falling away" from under the vehicle as it travels downrange - enabling it to use less lift (and therefore see less drag) to stay aloft. Thus more of the energy available can be used to travel downrange, instead of simply trying to stay aloft.

Repeating the entire footprint computation for the spherical Earth model, we see in Figure 9-2 that the footprint now looks very different. We again have the same three regions as before - no-skip, single-skip and double-skip. The no-skip and single-skip regions look similar to the ones in the flat Earth case, but go somewhat farther downrange. However, the double-skip region is now much bigger than in the flat Earth case. As we saw in Figure 9-1, this is because the curvature of the Earth helps the vehicle extend its range, and this effect is greater as the downrange distances become longer and comparable to the radius of the Earth.

Notice that if the initial speed were $V_i = 7.9$ km/s and $\gamma_i = 0$ deg, the flat Earth model would give a finite downrange distance, while the spherical Earth model would correctly give a downrange distance of infinity, since the vehicle will be in orbit at that velocity. Thus as the downrange distances considered become greater, the curvature of the Earth cannot be ignored - hence the large difference between the flat Earth footprint and spherical Earth footprint in Figure 9-2. Clearly, the spherical Earth footprint is more physically correct than the flat Earth footprint.

Figure 9-3 shows the footprint for the Earth penetrator case with the spherical Earth model. Compared to the flat Earth model footprint, the spherical Earth model footprint travels farther downrange for the same reasons as given before. Also for the same reasons, the minimum uprange also moves farther downrange - thus the entire footprint shifts downrange. The difference is about 40 km, much smaller than for the submunitions case. Since the downranges are much shorter, and curvature of the Earth is a less important factor. Nonetheless, this difference cannot be ignored and makes a noticeable difference in footprint shape and location. The flat Earth model was used because it is a simpler model and hence takes less computational time to converge to a solution. Furthermore, the solution to the flat Earth model can be used as an initial guess with which to initialize the solution to the full spherical Earth model. Also, the general behavior of the trajectories is captured very well in the flat Earth model. But to be more physically realistic, all cases considered for the rest of this work use a spherical Earth model.

Finally, Figure 9-4 shows that because of the vehicle's skipping ability, the submunitions footprint covers very large regions of the world. Thus the vehicle has very long ranges and can maneuver over significant distances.

With the trajectories now traveling over 3500 km downrange, the flight times are also long. The maximum downrange trajectory has a total duration of 719 seconds, which is more than 10 minutes. During this time interval, the Earth will have rotated almost 3 degrees, which corresponds to a displacement of 333 km at the surface of the Earth. Until now, none of the models have accounted for a rotating Earth, but clearly the rotation is an important effect, at least for the long trajectories. Therefore, the next step in refining the model will be to add in the rotation of the Earth.

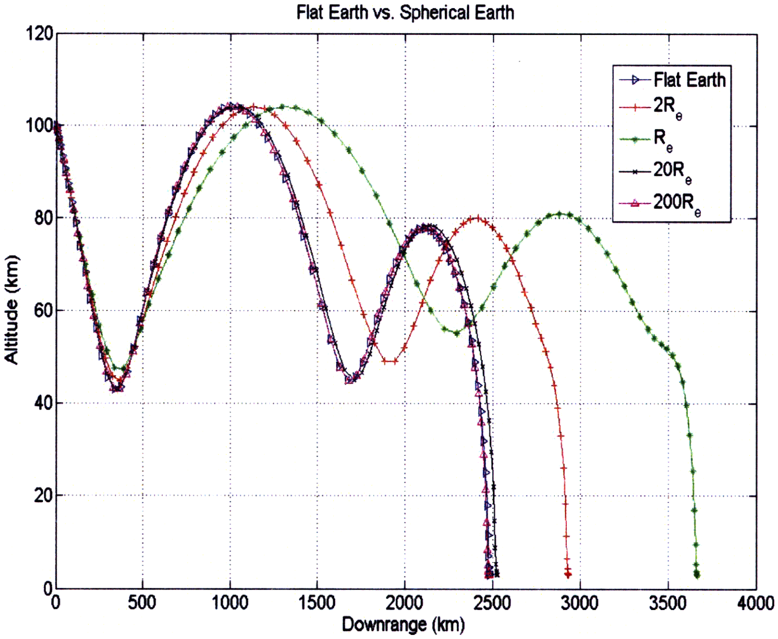

Figure 9-1: *The transition from a flat Earth to a spherical Earth, as the modeled radius of curvature is increased*

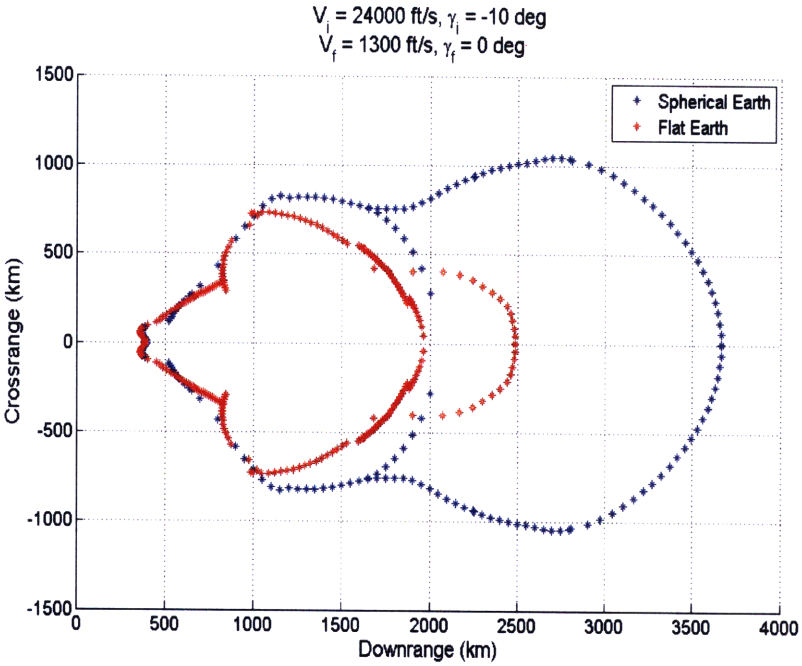

Figure 9-2: *The footprint for the submunitions case with a spherical Earth model*

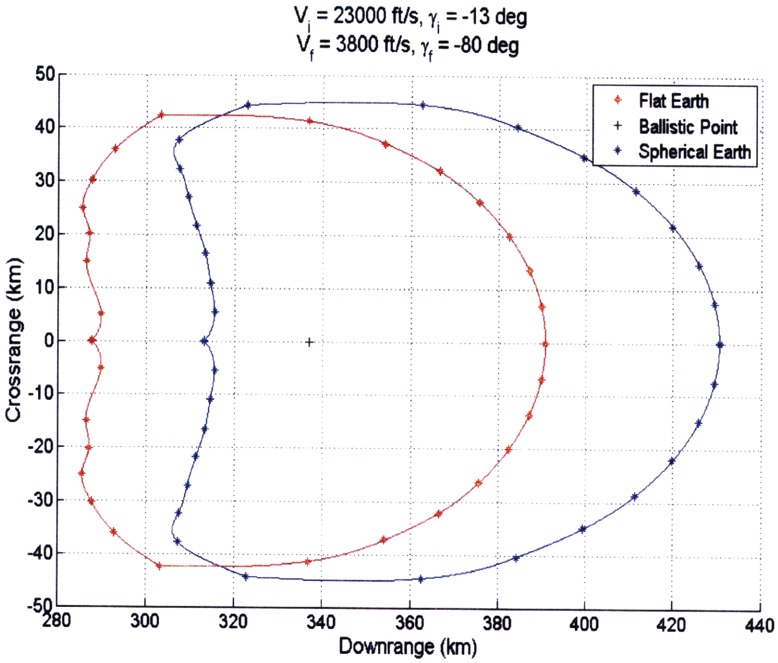

Figure 9-3: *The footprint for the Earth penetrator case with a spherical Earth model*

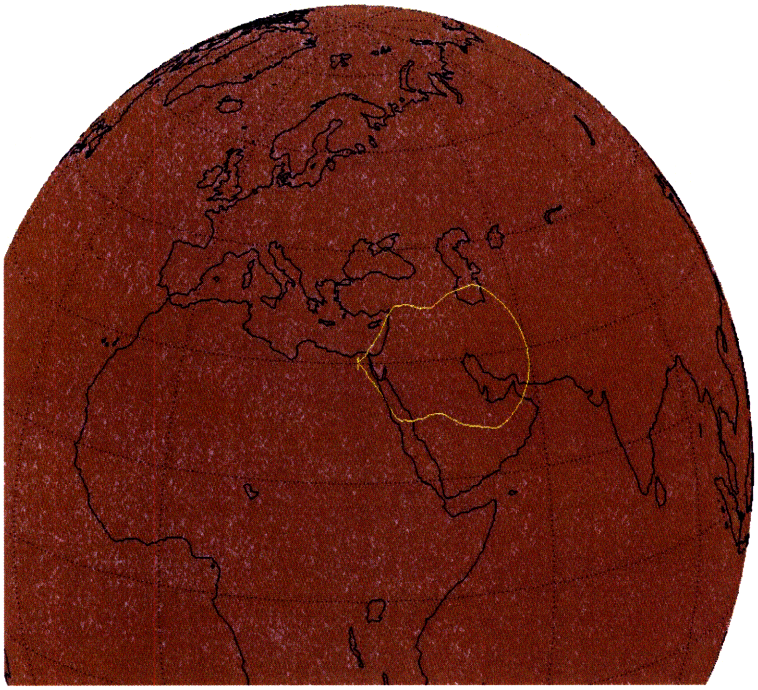

Figure 9-4: *The re-entry vehicle can cover large parts of the world because of its skipping capability*

9.2 Rotating Earth

As described at the end of the previous section, some of the trajectories (especially the downrange trajectories in the submunitions case) travel very long downrange distances and have flight times that are longer than 10 minutes. For such long-duration trajectories, accounting for the rotation of the Earth is important.

If the Earth were fixed in inertial space, and using an exponential atmosphere, a flight East would be exactly the same as a flight west. However, the Earth does rotate from West to East, and the atmosphere rotates with it. Thus a vehicle flying West would be flying against the motion of the atmosphere - essentially running into a "head-wind" relative to the inertial frame. This would cause the vehicle to lose downrange when flying West. Note that in the absence of the atmosphere, a West-flying trajectory would actually *gain* downrange. But in this case the aerodynamic forces dominate the dynamics of the vehicle, and so the effect of the moving atmosphere is more important.

Figure 9-5 shows two trajectories - one is the maximum crossrange trajectory in the Westwards direction, and another is the maximum crossrange trajectory in the Eastwards direction. The vehicle begins at 0 deg latitude and 0 deg longitude and heading North. The maximum crossrange in the Westwards direction is about 54 km shorter than in the Eastwards direction. The Westwards trajectory also travels about 30 km less downrange. This is because of the effect of the atmosphere discussed above. However, as trajectory flight times become short, the rotation of the Earth is less significant.

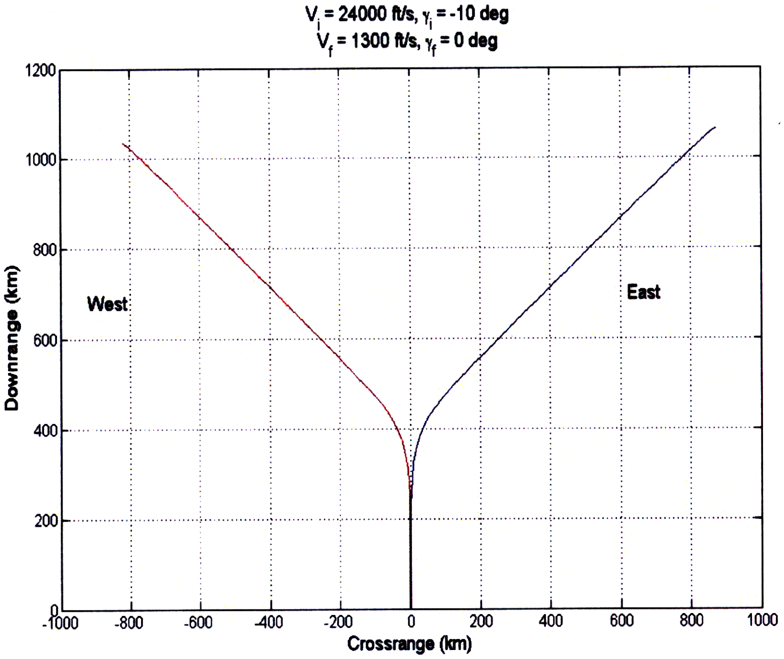

Figure 9-5: *When the rotation of the Earth and the atmosphere is accounted for, the vehicle's Westwards and Eastwards trajectories are no longer the same*

9.3 Refined Vehicle Model

The aerodynamic model used for the vehicle has a big impact on the computed trajectories. Therefore, getting an accurate aerodynamic model is essential. Since aerodynamic data (such as C_N, C_X and C_P as functions of α and Mach number) are obtained experimentally (or through CFD simulations), these models are usually in the form of 2-dimensional aerodynamic tables. The models presented in Equations 4.2 and used throughout this work are analytical function fits to these tables. Such function fits make computation much easier. They allow for calculation of partial derivatives and ensure that these partial derivatives are continuous. Also, computation times are much faster when analytical functions are available because these functions have better smoothness conditions. However, since they are fits, they are essentially approximations. If the table data were used directly with interpolation (cubic interpolation for ensure smoothness of derivatives), this fit error is greatly reduced and the computed aerodynamic forces are slightly different than for the analytical fit. This means that the trajectories computed when using table-lookup will be different from those computed using the analytical fit.

The actual aerodynamic tables for this vehicle were obtained from Textron Systems Inc. [23]. Using these tables, new trajectories were computed and compared with those calculated using the analytical fit, and shown in Figure 9-6. In this case the target was fixed at 350 km downrange, and the Earth penetrator trajectory from initial conditions $V_i = 23000$ ft/s and $\gamma_i = -13$ deg was computed. Figure 9-6 shows that the trajectories are similar. In Figure 9-7, we see that the maximum downrange that can be achieved with the table-lookup is in fact slightly greater than for the analytical fit.

The advantage in computing the analytical fit-based trajectory first is that the computation times are much faster. Since DIDO and pseudospectral methods in general require an initial guess for the solution, using the analytical fit-based trajectory as an initial guess greatly reduces the computation time required for the table-lookup trajectory, which otherwise would be slow because it involves cubic interpolation between data points.

Next, we look at the difference between the table-lookup model and the analytical fit models through another approach. We first calculate the controls using an analytical fit model in DIDO, and then propagate these controls in the table-lookup model. Figure 9-8 shows the results. The propagated trajectory deviates from the analytical fit-based trajectory. The error in the downrange is about 10 km, but the propagated trajectory also ends at an altitude of about 1 km. But even more important is the error in the terminal conditions, specifically flight path angle as shown in Figure 9-9. The propagated trajectory reaches a terminal flight path angle of only -65 deg, when the targeted flight path angle is -80 deg. Thus the controls computed using the analytical fit-based model cannot simply be used with the table-lookup model. New controls need to be computed. However, as discussed before, these computations are made much faster if the analytical fit-based trajectories are used as a starting point. Also, the analytical fit to the data can be improved using more sophisticated methods. The analytical fit tends to be better in some parts of the table than in others, so by using different functions in different regions of the table data instead of one single function for the entire table the error can be reduced.

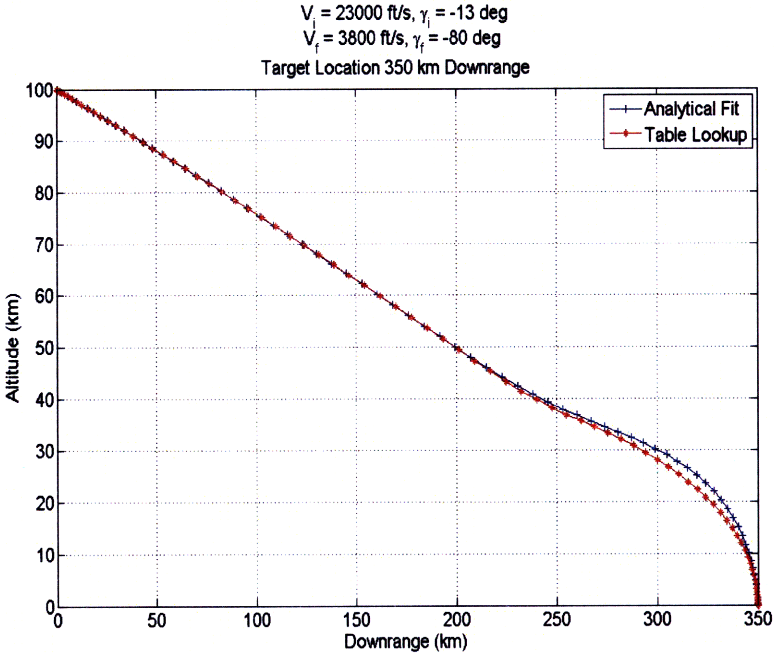

Figure 9-6: *The analytical fit-based trajectory and the table lookup-based trajectory*

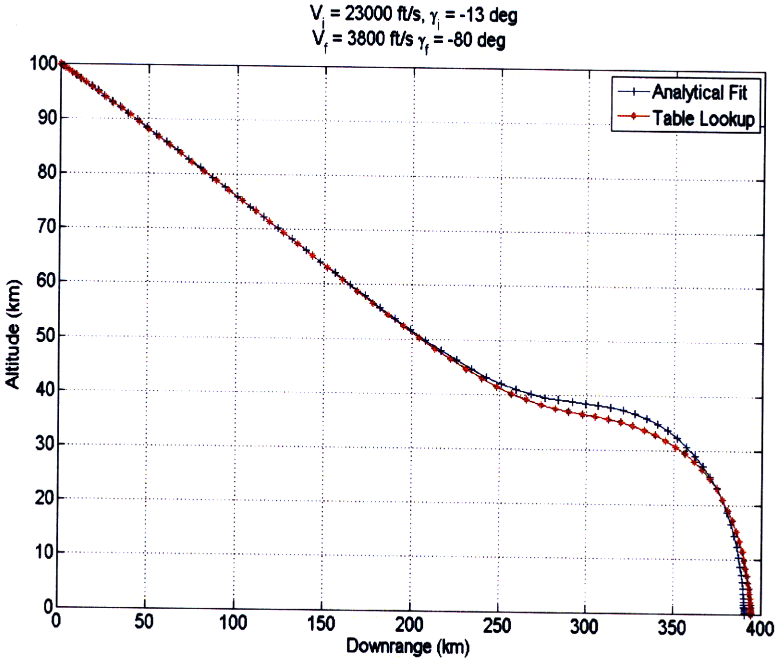

Figure 9-7: *The analytical fit-based trajectory and the table lookup-based trajectory for the maximum downrange*

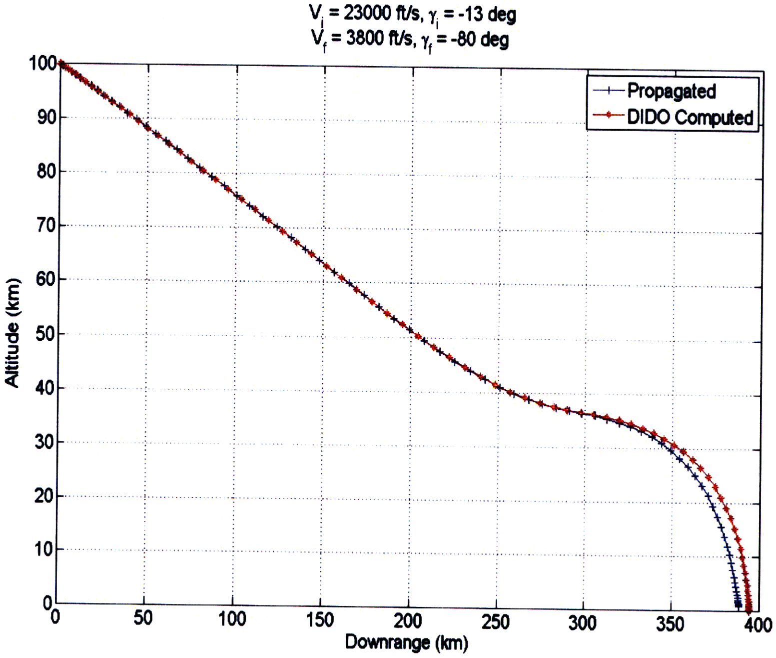

Figure 9-8: *The trajectory using controls computed by DIDO propagated using table-lookup*

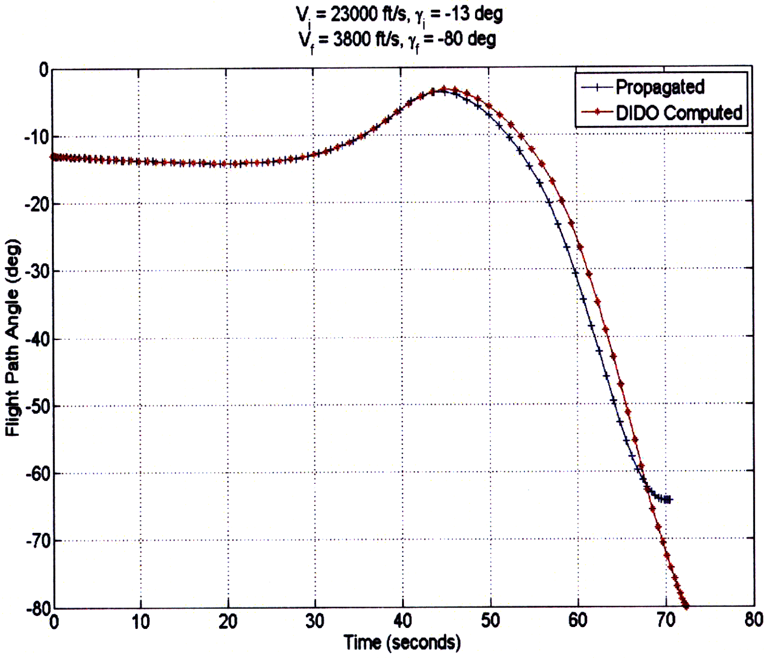

Figure 9-9: *The flight path angle history using controls computed by DIDO propagated using table-lookup*

9.4 Reverse Footprints for Skip Trajectories

We had seen previously that it is possible to create a "reverse footprint" in speed and flight path angle for a fixed target location and terminal conditions. This was done for the Earth penetrator case with the flat Earth model when the trajectories had no skips. However, the same analysis can be performed on the submunitions trajectories with the spherical Earth model. Since these trajectories have skips, the analysis is somewhat more involved.

First, we pick a target location. In this case, we chose 3500 km downrange and 0 km crossrange, since this point can be reached only by two skips as shown in Figure 9-2. The terminal altitude, speed and flight path angle are the same as those used for all submunitions trajectories (3 km, 1300 ft/s and 0 deg respectively). Doing so, we get the reverse footprint shown below in Figure 9-10.

We see clearly that traveling 3500 km downrange requires a lot of initial energy - the entire reverse footprint lies above 20000 ft/s, so any trajectory that starts at a lower initial speed will not reach 3500 km downrange. Furthermore, the steeper the initial flight path angle, the faster the minimum speed required, because the vehicle enters the atmosphere sooner (and hence travels less distance during the ballistic portion of its trajectory) and thus needs greater initial energy to reach the same downrange distance. While there is a region between flight path angles -6 deg and 0 deg where a large range of initial speeds are feasible, realistically it is very unlikely that the booster will be able to achieve such high speeds and shallow flight path angles. In fact, the highest initial speed considered reasonable for the Textron vehicle is 24000 ft/s at -10 deg flight path angle. From Figure 9-10, we see that this point is very close to the lower edge of the reverse footprint. Thus if the vehicle were to be deployed with even a slightly lower initial speed, it would be unable to reach its target.

This sensitivity to initial conditions is largely due to the skipping behavior of the trajectories. If the vehicle were going too slow to be able to take a skip, it would immediately lose much of its downrange capability. Thus it is important to quantify the conditions under which the vehicle can skip, and how wide a margin is available. This analysis is done next.

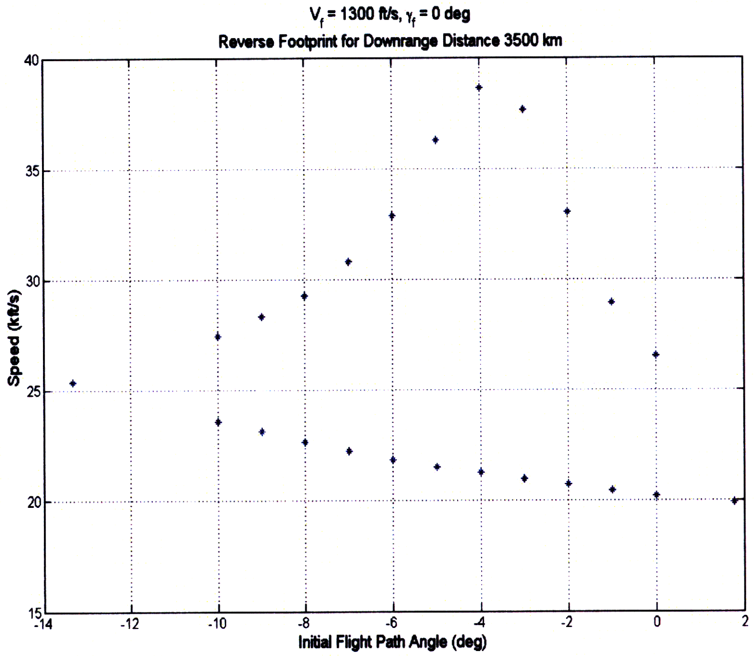

Figure 9-10: *The reverse footprint for the Submunitions case*

9.4.1 Skip Trajectory Robustness

Many of the trajectories presented in this work, particularly for the Submunitions mission, rely on skipping behavior to travel thousands of kilometers downrange, and similarly large distances crossrange. But the robustness of these trajectories needs to be investigated further. For instance, if the vehicle were to encounter a slightly denser atmosphere than had been planned for, the drag will be slightly greater, resulting in loss of more speed than accounted for. If enough speed is lost, then the vehicle might lose the ability to skip and thus immediately lose most of its long downrange capability. This has been partly addressed in the discussion about reverse footprints, but the range of conditions at the skip point (defined as when $\gamma = 0$) that would still permit skipping needs to be computed - essentially a "reverse footprint" at the skip point. If this range is very small, then the skip trajectories will not be robust and might become infeasible in the presence of any disturbance. Therefore it is important that the robustness of the skip trajectories be determined.

As mentioned in the discussion about reverse footprints, the full range of conditions at the first skip that are required to reach this point would be defined in terms of ranges of altitude, downrange, crossrange, speed and heading angle (since at a skip $\gamma = 0$). Thus the full range of acceptable conditions at the first skip would be a 5-dimensional subspace. However, to make the problem more tractable, we first look at only the in-plane case, thus setting crossrange and heading angle to 0. We now have only a 3-dimensional subspace in altitude, downrange and speed. We simplify the problem further by requiring that the skip take place at a certain fixed downrange distance. Thus we now have a 2-dimensional subspace in altitude and speed that determines the range of conditions (given the restrictions imposed on the downrange, heading angle and crossrange).

However, the entire range of altitude and speed is not accessible from the initial conditions at piercepoint. In fact, given the initial conditions, as well as a fixed downrange distance at which the first skip must occur (defined by $\gamma = 0$ deg), there is a feasible region - analogous to the "forward footprint" discussed before - in altitude, speed, crossrange and heading angle. Since we are setting crossrange and heading angle to 0, this feasible region is also a subspace in 2-dimensional space (consisting of speed and altitude).

Thus with the given initial conditions, we have a "forward footprint" (in altitude and speed) at the first skip. Similarly, given the terminal conditions, we have a "reverse footprint" (also in altitude and speed) at the first skip. For the vehicle to satisfy both the initial and terminal conditions, it must lie on both the "forward footprint" as well as the "reverse footprint".

These two footprints are shown in Figure 9-11. The vehicle starts at $V_i = 24000$ ft/s and $\gamma_i = -10$ deg, and the first skip is fixed to be at a downrange distance of 390 km. Thus the forward footprint (in blue) shows all the speeds and altitudes the vehicle can achieve with "terminal conditions" being downrange of 390 km and flight path angle $\gamma = 0$ deg. Also shown (in red) is the reverse footprint for terminal conditions $V_f = 1300$ ft/s, $\gamma_f = 0$ deg at downrange 3500 km, with "initial conditions" being a downrange distance of 390 km and $\gamma = 0$ deg. The region where these two footprints intersect is the region from which reaching a target 3500 km downrange is feasible.

Another way to interpret these footprints is to look at the forward footprint (blue) and see that the vehicle could be anywhere inside that footprint (with the given initial conditions). However, it *must* be in the small region where the forward footprint intersects with the reverse footprint to be able to reach 3500 km downrange. Clearly, this region is small. Any disturbance that pushes the vehicle out of this region will put the 3500 km downrange target out of reach. Such analysis of the robustness of the skip trajectories provides valuable insight for designing a guidance system that would allow the vehicle to achieve the terminal conditions and reach its target.

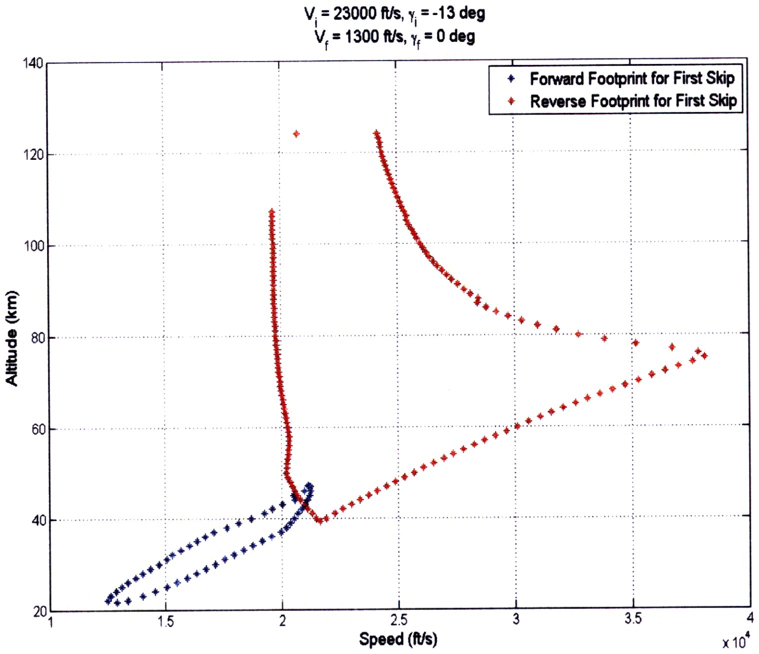

Figure 9-11: *The forward footprint at the first skip from the initial conditions, the reverse footprint at the first skip from the terminal conditions, and the feasible region for the first skip (the intersection between the two footprints)*

THIS PAGE INTENTIONALLY LEFT BLANK

Chapter 10

Vehicle Properties

Until now, we have assumed a certain vehicle configuration - the aerodynamic properties, the mass and the inertia have all been held constant. However, as we vary each of these parameters, the dynamics of the vehicle change. Two of the parameters that we will look at are the mass and the aerodynamics. First we will look at the effect of reducing the mass of the vehicle, while keeping the aerodynamic characteristics the same - which closely approximates what would happen if the mass of the vehicle were to be reduced while retaining its external shape. and we will see that the reduced-mass vehicle can travel much smaller distances. Next we will increase the lift-to-drag ratio (L/D) and see that this makes the vehicle much more maneuverable.

10.1 Effect of Varying Mass

We look at the case where the vehicle's mass is reduced from 1100 lbs to 200 lbs. We retain the same vehicle aerodynamics as shown in Tables 4.1, 4.2 and 4.3. This implies that although the mass of the vehicle has changed, its shape is still the same. Since the tables are non-dimensionalized, this can be viewed as a scaled reduction in size of the vehicle. Clearly this is a simplification, because in general changing the size of the vehicle could change the aerodynamics. Furthermore, the G-loading and stagnation point heat rate limits are still the same. In reality as the mass is decreased, it is more likely that these limits become tighter because lower mass implies a smaller heat shield and a lighter structure. However, in this section we focus only on the effect of changing the mass and keep all other parameters the same.

Since the vehicle is much lighter, but the aerodynamic forces are the same, the acceleration caused by these forces will be much greater. Since the vehicle can only decelerate (it has no thrust) this means that the lighter vehicle will slow down much faster and thus will not be able to travel as far as a heavy vehicle. This is shown most clearly in Figure 10-1, where the maximum downrange for the submunitions case is 3000 km shorter for the 200 lbs vehicle. Clearly, the vehicle can no longer skip because it loses most of its initial speed in the very first entry into the atmosphere.

Next we look at the Earth penetrator case, which is more demanding than the submunitions case because of the high terminal speed. It turns out that the 200 lbs vehicle loses so much speed immediately upon re-entry that the vehicle cannot meet the 3800 ft/s terminal speed constraint. In fact, the minimum mass which the vehicle needs to meet this constraint (with initial conditions $V_i = 23000$ ft/s, $\gamma_i = -13$ deg) can be computed using the same optimization techniques as used before, but with the mass being the cost function. This shows us that the minimum mass required is 550 lbs. Again in this case as well, we see that the vehicle loses significant downrange because of its reduced mass.

Next, we look at the more realistic case where a 200 lbs vehicle is released from its boost vehicle with initial conditions $V_i = 16000$ ft/s and $\gamma_i = -37.2$ deg. Since the initial speed is even lower, the 200 lbs vehicle is no longer feasible even for the submunitions mission - therefore we first compute the minimum mass required for this vehicle, and from Figure 10-4 we see that the minimum mass is 276.8 lbs. We raise the mass to be 322 lbs (above the minimum mass) and then compute the forward footprint of the vehicle from the given initial conditions. As seen in Figure 10-3, the vehicle can travel less than 145 km downrange and 15 km crossrange. The lower initial energy, together with a lower initial mass, together greatly reduce the footprint when compared to a heavier vehicle.

In some cases, the boost vehicle might not be able to launch a vehicle that is heavier than 200 lbs, and might not have the capability to reach speeds faster than 16000 ft/s. In these cases, in order to be able to cover a larger area with the re-entry vehicle's footprint, we would need to enhance some other property of the vehicle. In the next section, we will see how increasing the lift-to-drag ratio (L/D) enables us to do that.

Another thing to note is that *reducing* the mass *reduces* the distance traveled. This is the opposite of powered vehicles. For powered vehicles, lower mass means greater acceleration for a given expenditure of energy. However, since there is no expenditure of energy and there is only deceleration, lower mass means greater deceleration and hence shorter distance traveled.

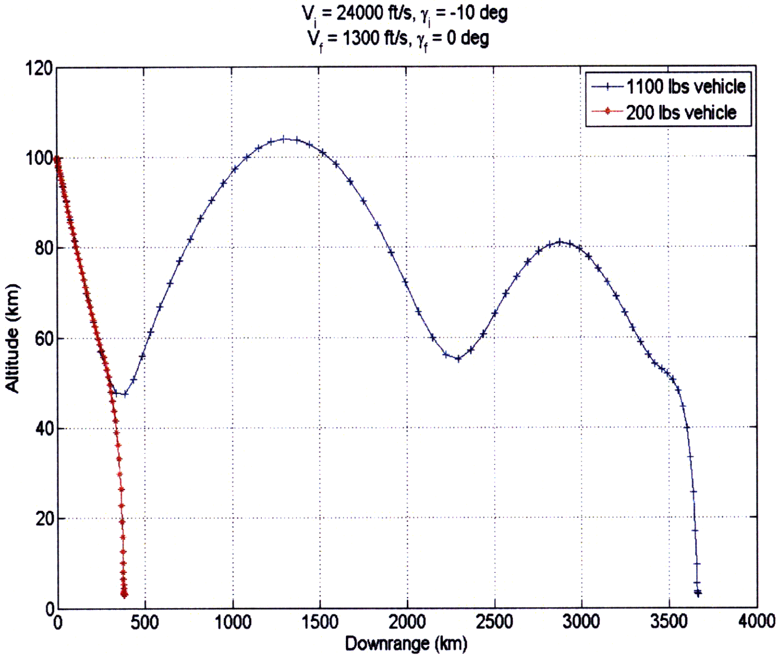

Figure 10-1: *Loss in downrange distance when the mass of the vehicle is reduced*

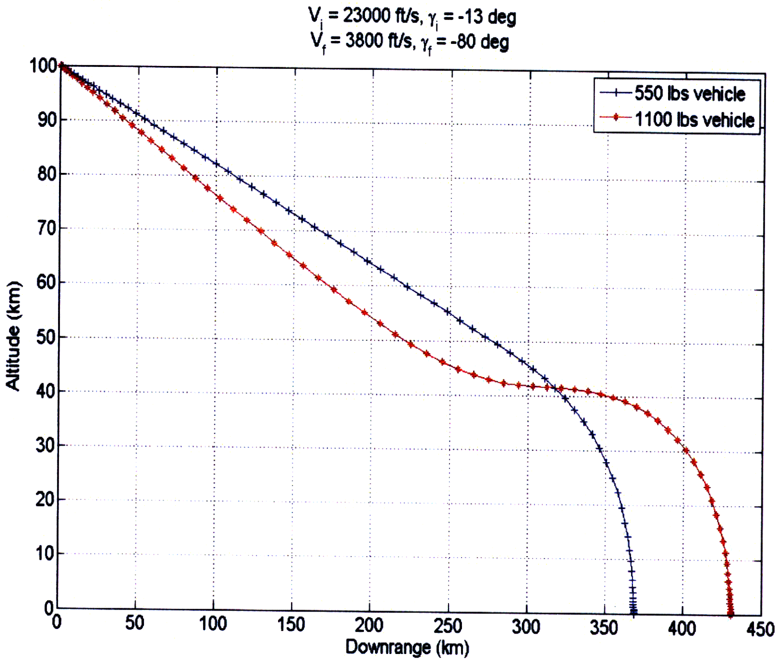

Figure 10-2: *The minimum mass required to satisfy the Earth penetrator mission with given initial conditions*

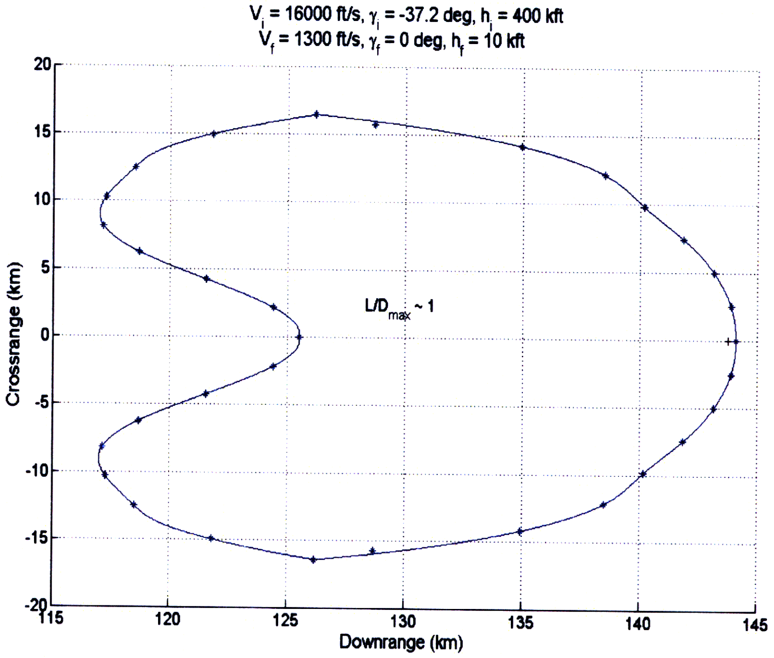

Figure 10-3: *The landing footprint for a 322 lbs vehicle with given initial conditions*

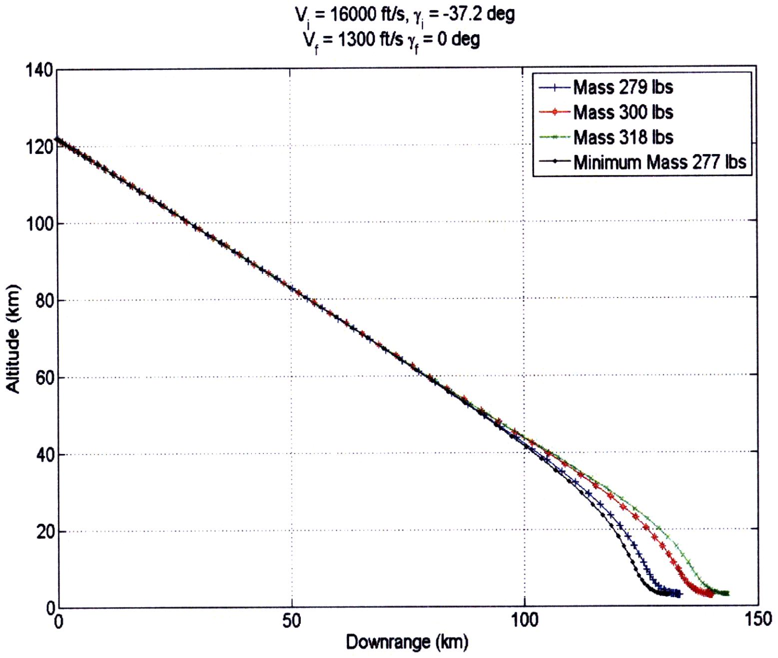

Figure 10-4: *The minimum mass required to achieve the submunitions mission with the given initial conditions*

10.2 Effect of Varying Lift-to-Drag Ratio

For vehicles traveling through the atmosphere, the lift-to-drag ratio is a key parameter. Even in powered flight (for aircraft, for instance) L/D determines some very key performance measures, such as range. As we will see in this section, this is true for re-entry vehicles as well. Greater L/D means that the vehicle can apply more lift (and hence maneuver) while facing less drag (and hence losing less energy during those maneuvers).

For the vehicle being considered, L/D is a variable quantity that depends on the angle of attack and Mach number. Therefore, a useful way of summarizing the L/D is to look at the maximum L/D, $(L/D)_{max}$. For the vehicle considered until now, $(L/D)_{max} \approx 1$.

We now increase $(L/D)_{max}$ such that $(L/D)_{max} \approx 2$. We do this by increasing the normal lift coefficient C_N by a factor of two (for the small α being used here, $\alpha < 10$ deg, we have $C_N \approx C_L$). We then compute the footprint for the same initial conditions as used in Figure 10-3. This footprint is shown in Figure 10-5.

Comparing the two footprints in Figures 10-3 and 10-5, we see that the footprint for the $(L/D)_{max} \approx 2$ vehicle is much bigger than for the $(L/D)_{max} \approx 1$ vehicle. In fact, even with a low mass of 200 lbs, we get as much as 1600 km maximum downrange distance. Similarly, we get about 1000 km crossrange. The footprint also has two regions - a "one skip" region and a "two skip region". From Figure 10-6, we see that vehicle achieves both maximum downrange and maximum crossrange by skipping twice. This is in contrast to the $(L/D)_{max} \approx 1$ vehicle, which could travel barely 150 km downrange and could not skip at all. This correlation between the maximum L/D and footprint size is also observed by Vinh [9], despite making an equilibrium glide assumption. Thus it is accurate to say that high L/D translates into better vehicle performance.

Even more impressive is the maximum-out-of-plane angle that this vehicle can achieve. The vehicle can travel as far as 145 deg out-of-plane. The vehicle actually ends up 100 km *behind* piercepoint, and does this by taking a backwards skip after re-entering the atmosphere. It achieves this by simultaneously turning and skipping. This is shown in Figure 10-7. The vehicle also stays under its G-load and stagnation point heat rate limits. While it is important to keep in mind that if an actual 200 lbs vehicle were to be built the heat rate and G-load limits would most likely be much tighter, the relatively slow initial speed ensures that the heat rate and G-loading stay small. Thus by having a high-L/D vehicle and starting at relatively slow speeds, the maneuvering capability can be significantly enhanced. This would be important in the cases where evasion maneuvers are necessary.

Also note in Figure 10-8 that the changing the mass of the vehicle does not effect the maximum downrange trajectories much when $(L/D)_{max} \approx 2$. This is because the minimum mass required to achieve the submunitions mission when $(L/D)_{max} \approx 2$ is much lower than 200 lbs. As the mass is reduced to be closer to the minimum, the trajectories begin to change the footprint begins to rapidly shrink, as we saw in the previous $(L/D)_{max} \approx 1$ case.

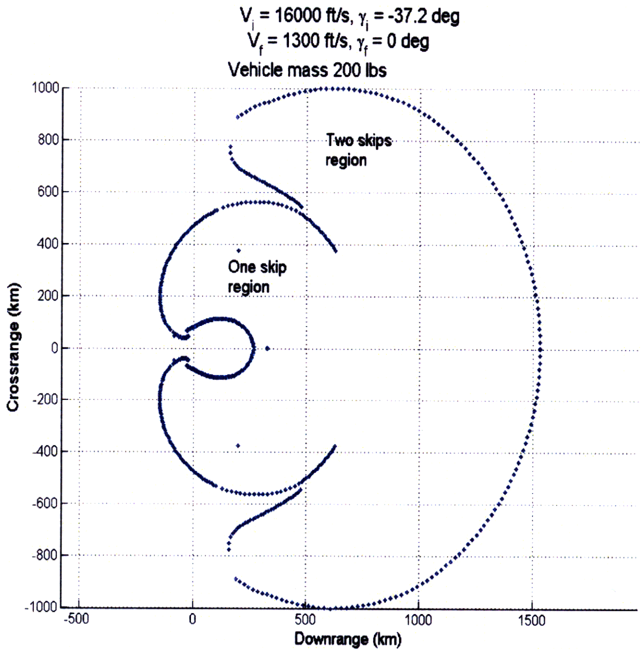

Figure 10-5: *The footprint for the vehicle with* $(L/D)_{max} \approx 2$

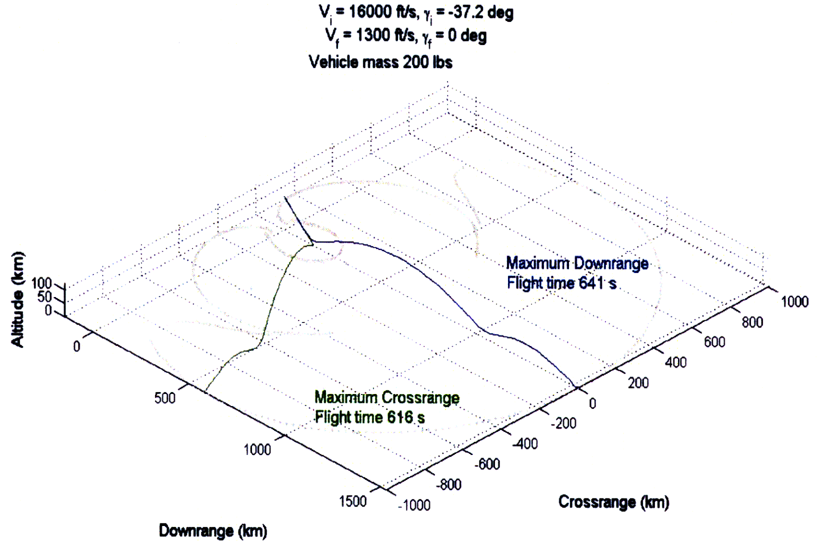

Figure 10-6: *The maximum downrange and crossrange trajectories with* $(L/D)_{max} \approx 2$

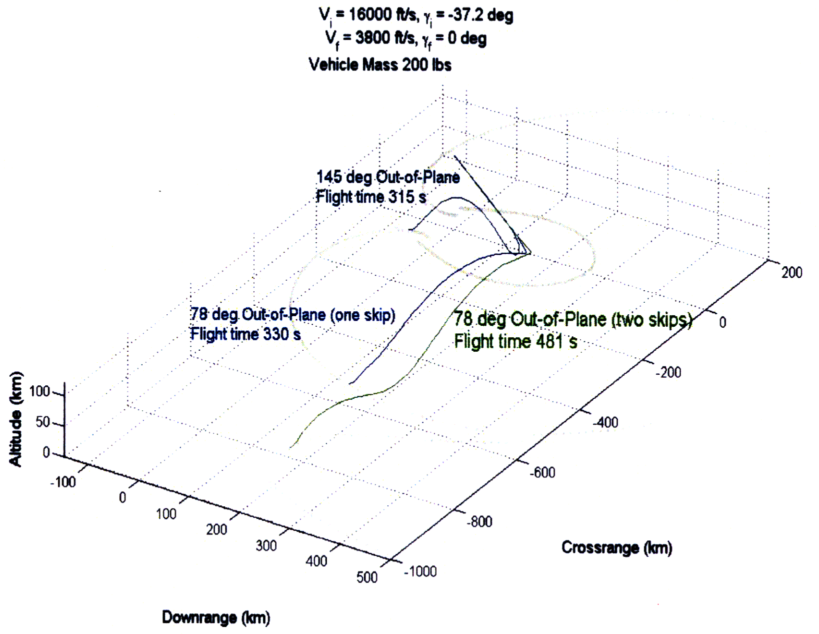

Figure 10-7: *The maximum out-of-plane angle trajectories, as well as the one-skip and two-skip trajectories with* $(L/D)_{max} \approx 2$

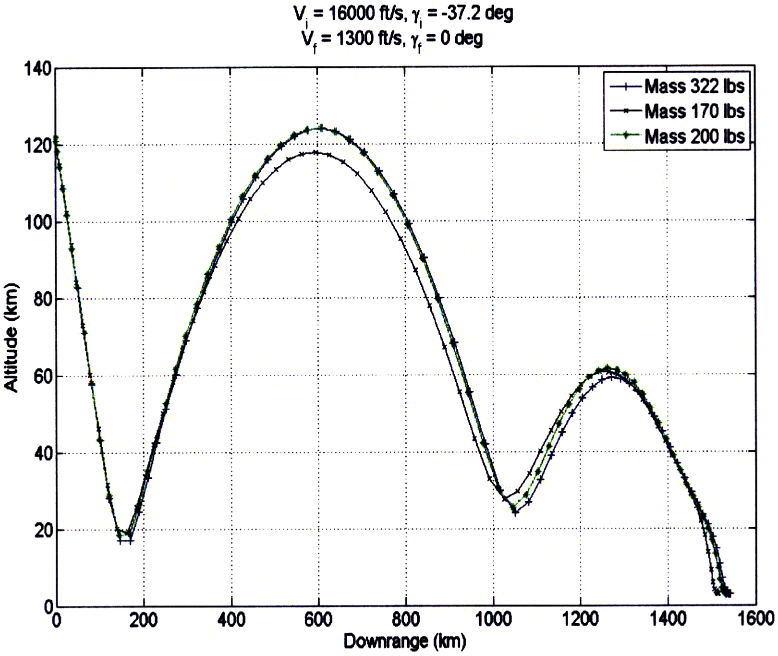

Figure 10-8: *The maximum downrange trajectories for* $(L/D)_{max} \approx 2$ *for varying masses*

10.3 Effect of Varying Response Time

Another important parameter that affects the performance of the vehicle is the control system response time. The response time is the time it takes for a control command to be translated into a change in the actual state of the vehicle. For instance, the angle of attack α is a physical quantity that is part of the state of the vehicle. However, the vehicle does not have the ability to change the angle of attack instantaneously, because this would require the vehicle to be able to achieve arbitrarily high angular speeds. In reality, this time-delay between issuing a commanded angle of attack α_C, and the actual α achieving that value is finite.

As we have seen previously (Equations 3.1), the delay is modeled as a quadratic delay with parameters ω and ζ which are described in Equations (4.5). For a second-order system, the time-delay between input and output can be written as the rise time, given as

$$T_r = \frac{\pi - \tan^{-1}\left(\frac{\sqrt{1-\zeta^2}}{\zeta}\right)}{\omega\sqrt{1-\zeta^2}}$$

Thus the time delay can be increased either by increasing the damping ζ or by decreasing the frequency ω. In Equation (4.5), we see that increasing the inertia decreases the frequency, which in turn increases the rise time. This physically makes sense because bodies with more inertia respond slower to torque inputs, and the vehicle ultimately uses reaction-control thrusters to change its angle of attack. Therefore, in order to increase the response time, we increase the inertia, or increase the damping, or both. In the plots to follow, we increase both the inertia as well as the damping.

In Figure 10-9, we see that the maximum downrange trajectory is shorter and the minimum uprange trajectory is longer - in both cases, a loss in performance. However, what is most surprising is the fact the loss is only about 5 km in the minimum uprange case, and much smaller in the maximum downrange case. The reasons for this can be seen in Figure 10-10, which shows the actual angle of attack and the commanded angle of attack for the maximum downrange. Two cases are shown - one with the nominal damping and inertia, and another with 10 times the damping and 10 times the inertia. The high-inertia and high-damping case shows that there is a very noticeable delay between the commanded

α_C and the actual α. However, what is important is that the *actual* α still follows almost exactly the same profile as the actual α in the nominal inertia case. Thus the solver chooses the controls α_C in the high-inertia and high-damping case such that the actual α is still the same as in the nominal case. The solver is able to accomplish this because the model is deterministic - i.e. by knowing the model, the solver can predict exactly what the actual α needs to be to achieve maximum downrange, and also knows exactly what α_C command it needs to issue in order to achieve this α. Thus having a longer response time only changes the α_C needed to achieve the optimal α.

If the model were not deterministic and the future α and other states could not be predicted exactly, the higher inertia would greatly reduce the vehicle's ability to compensate for errors during flight, and would therefore adversely affect its performance. Furthermore, even with the deterministic model, there is a maximum inertia that the vehicle can have. If the vehicle had infinite inertia, for instance, the controls would have no effect on the state of the vehicle - the vehicle would not be able to maneuver to reach its terminal conditions and the problem would clearly be infeasible. Thus there is a finite maximum inertia beyond which the boundary conditions can no longer be reached. Inertias of up to 50 times the nominal were tried, and the even at these unrealistically high inertias, the problem was still feasible. Even higher inertias were not explored because they are completely unrealistic.

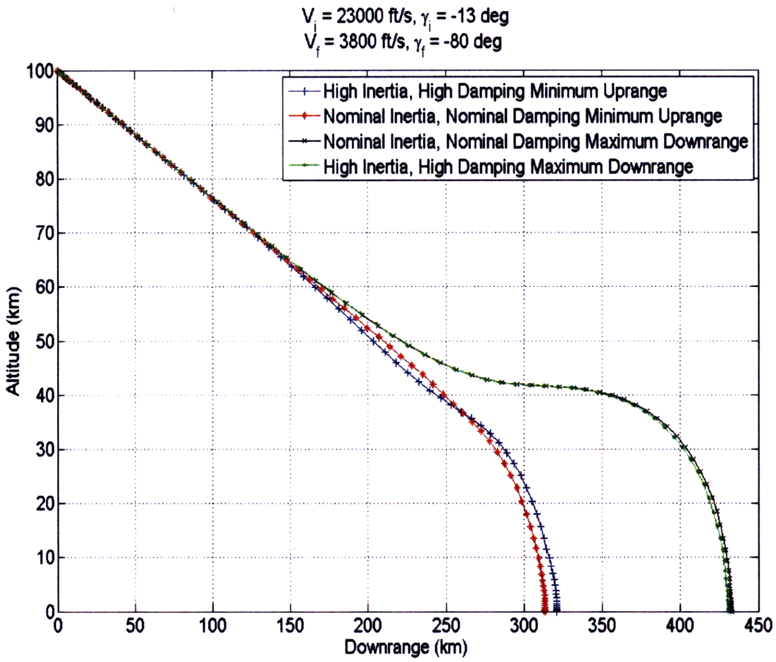

Figure 10-9: *The variations in maximum downrange and minimum uprange due to longer response time*

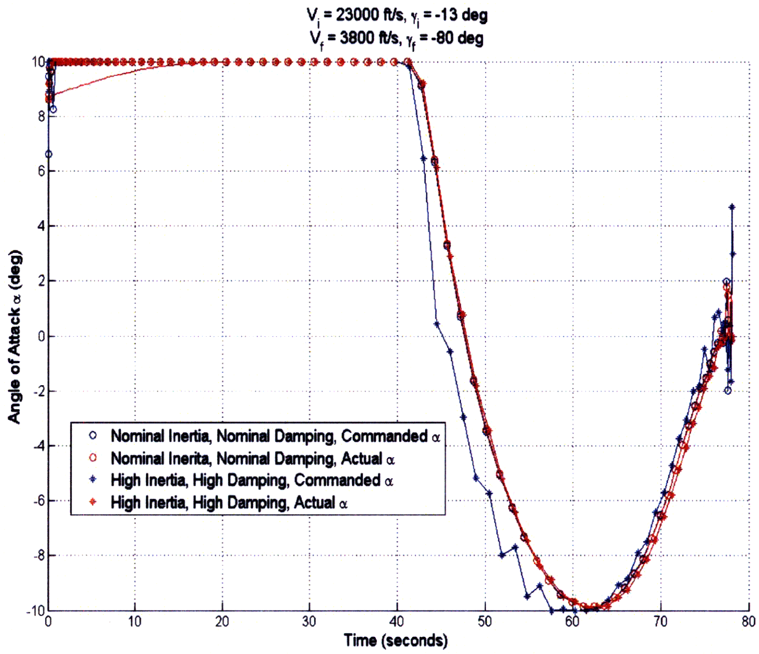

Figure 10-10: *The variations in angle of attack due to longer response time*

Chapter 11

Conclusions and Future Work

In this work, we have presented a method for computing optimal trajectories for a re-entry vehicle with non-linear dynamics. The vehicle was modeled as a 3-DOF system with a quadratic lag between the commanded control and the actual control (thus making the system effectively 4-DOF). The aerodynamics forces on the vehicle were modeled as non-linear functions of the angle-of-attack and the speed. The models were chosen to capture important transonic behavior, such as the large shift in the location of the center of pressure, and the large increase in drag, in the vicinity of Mach 1. With these models, the vehicle was shown to be capable of satisfying two different types of missions, the Earth penetrator mission and the Submunitions deployment mission. The vehicle's capability to re-target to a different location upon receiving an in-flight target update was characterized in the form of a "landing footprint". The effect of various constraints, such as the stagnation point heat rate, the maximum G-loading, and the terminal conditions (flight path angle, heading angle) was investigated. The effect of initial conditions on the vehicle's landing footprint was also investigated. Then, the vehicle's ability to reach a target from various initial (deployment) conditions was characterized in the form of a "reverse footprint". The trajectories that the vehicle follows to reach extremal points such as the maximum downrange and maximum out-of-plane angle were closely analyzed, and it was seen that in the Submunitions mission, the vehicle is capable of skipping to travel as far as 3500 km downrange. The robustness of these skip trajectories was analyzed, and the conditions under which a skip could be "missed" were quantified. The effect of various vehicle parameters, specifically the mass, the maximum L/D and the response time was also studied.

11.1 High-Fidelity Modeling

All the trajectories designed here are based on standard models for the atmosphere (exponential atmosphere), gravity (central-body force) and vehicle aerodynamics. However, each one of these models has some error in it. For instance, the atmospheric density in reality is not exponential, and has variations on a seasonal and even daily basis. Models such as GRAM-99 account for these variations. Using such models is entirely possible within the framework discussed here, but was not done because of limits on computational capability. Although GRAM-99 models exist ready for use, including them in the solution would drive up computation times while adding little to the mission planning. Also, the gravitational field of the Earth is actually not purely spherical, but has J2 and other higher-order terms. These have to be accounted for in order to make the model more accurate.

Although a simple model was used for the aerodynamic forces as functions of angle of attack and speed, the reality is that the aerodynamic forces will deviate from this model. For instance, if the vehicle were rolling, the flow around the vehicle would induce a lift force in the lateral direction (in the same way that flow around a rotating cylinder induces lift). Such interactions between the air flow and the motion of the vehicle are not accounted for in the models used here, but could be included in a more high-fidelity model.

11.2 6-DOF Model

All the models studied in this work have been either 3-DOF or 4-DOF, and essentially use the angle of attack and the lift direction vector as controls. The models are made more realistic by adding the quadratic lag between the commanded control and the actual control. However, there are still some details that are not accounted for and which can be in a full 6-DOF model that includes the attitude dynamics of the vehicle.

One example is in the angle of attack limit. Since the vehicle is statically stable, it will tend to come back to zero angle of attack when perturbed. To hold the angle of attack at a non-zero value, a continuous torque would have to be applied by the reaction control system to counter the restoring moment. The greater the angle of attack, the greater this restoring moment and the more control torque required. Thus the maximum control torque available would act as an upper bound on the angle-of-attack achieved. However, since the restoring moment is an aerodynamic moment, it is also proportional to the speed and atmospheric density. The maximum control torque, on the other hand, is likely to be constant. Thus the maximum angle of attack would be smaller at high speeds and high densities, and higher at low speeds and low densities. In all models used here, the maximum angle-of-attack has been simply bounded to be 10 deg. But this is in fact not true - at low speeds higher angles-of-attack could be achieved. Modeling the full attitude dynamics of the system with the control torques as the controls would account for such details and improve the fidelity of the mission planner.

Thus while the basic behavior of the trajectories might not change significantly, a 6-DOF model would give insights into the relation between the control system on the actual vehicle (the reaction control system), the attitude dynamics, and the overall trajectory design.

11.3 Error Analysis

Even if the fidelity of the models used is greatly improved, there will still be sources of noise that cause errors in the computed trajectory. The sources of noise are primarily from the environment, the navigation system, and the control system.

Noise in the environment arises from the fact that the atmosphere is very complex and varies constantly. Although models such as GRAM-99 are very accurate, they cannot exactly predict conditions on a particular day and time. Some of these conditions are phenomena like local winds which cannot be modeled easily. All these factors contribute to some error between the anticipated atmospheric conditions and the actual atmospheric conditions, even if a reasonably high-fidelity model is used. Such effects would have to be accounted for by allowing for stochastic terms in the models used.

Noise in the navigation essentially means that the vehicle thinks it is in a certain state (the navigated state) when in fact the actual state could be slightly different. Since the control commands can be issued on the basis of the navigated state, it is important to account for noise in the navigated state. Noise in the control system corresponds to the fact that the actual control achieved might not be exactly the same as the commanded control, due to noise within the control system itself. Note that the noise in the navigated state and the control system is not expected to be significant for a well-designed vehicle, it is an additional factor that must be considered.

This would particularly be true because as the vehicle re-enters the atmosphere at high speeds, the air around it turns into plasma and prevents the vehicle from receiving GPS signals. During this plasma blackout time, the vehicle must rely entirely on its on-board inertial navigation system, which has significantly more noise and error than the GPS-based navigation. Thus the effect of noise in the navigation must be considered. Another approach would be to design trajectories that minimize the time spent in plasma blackout, or if possible, design trajectories that have no GPS plasma blackout at all.

The effect of adding noise (either to the environment or to the navigation and control systems) would be to effectively reduce the footprint. For instance, the maximum downrange trajectories computed in the noiseless case would realistically no longer be feasible since the vehicle has to spend some energy in compensating for the errors in its trajectory. Since we would have an expectation of how much noise there is, we would have an expectation of how much effort needs to be spent in compensating - and we would have an expectation how much downrange would be lost. This expected maximum downrange would then have a confidence interval around it - downranges that are longer than the maximum downrange will have a low confidence level, while shorter downranges would have a higher confidence level. Extending the same idea to minimum uprange and maximum out-of-plane angle, we see that the the 99% confidence level footprint, for instance, would be smaller than the 90% confidence level footprint. Such footprint analysis in the presence of noise would also tell us about the robustness of the trajectories chosen. Therefore the uncertainity analysis would be essential to understanding the system better.

11.4 Guidance

Closely related to the issue of sensitivity to noise is the question of guidance. While the trajectories presented here are optimal reference trajectories, addition of noise makes it essential to have a guidance law. Several guidance schemes already exist in the literature

([11], [19], [10]). The guidance law used would have to ensure that the critical terminal conditions are met, and would most likely have to interface with a 6-DOF model since some conditions (such as the zero terminal angle-of-attack condition) involve the attitude dynamics.

The issue of dealing with moving targets has been addressed through the concept of a landing footprint - as long as the moving target remains within the footprint, the vehicle will be capable of reaching it. However, it is the guidance scheme that would have to ensure that the vehicle can actually hit that moving target. Some guidance laws exist in the literature to deal with moving targets (e.g. [10]), but an alternative would be to recompute the optimal trajectory to the target in real-time as new target information is obtained. Note that this would require the optimization software to run in real-time and generate very accurate solutions.

Other factors to consider would be the sensitivity of the vehicle's guidance law to a longer control system response time. It was seen in the previous chapter that having a longer response time without noise meant that the control response could be predicted and the control commands planned ahead of time to account for this. In the presence of noise, this is no longer possible. The longer the response time becomes, the harder it is for the guidance system to remove noise disturbances. Thus the sensitivity to the response time will be much greater. But as discussed in the previous section, the methods presented here can be used to determine a nominal footprint and a confidence interval about that nominal footprint - and the sensitivity of that footprint and confidence interval to control system delays can be analyzed using the tools and ideas presented here.

The guidance law should also be capable of tracking skip trajectories, which can be sensitive to disturbances. This sensitivity, and a method to quantify the sensitivity, was discussed in the Skip Trajectory Robustness section.

Thus the work presented here provides a tool for trajectory design and a strong starting point from which to begin addressing the problem of trajectory optimization for maneuverable re-entry vehicles in greater detail.

THIS PAGE INTENTIONALLY LEFT BLANK

Bibliography

[1] Kimberly A. Clarke, *Performance Optimization Study of a Common Aero Vehicle using a Legendre Pseudospectral Method*, Masters Thesis, MIT Department of Aeronautics and Astronautics, May 2003.

[2] Alisa M. Hawkins, *Constrained Trajectory Optimization for a Soft Lunar Landing from a Parking Orbit*, Masters Thesis, MIT Department of Aeronautics and Astronautics, June 2005.

[3] A. D. Ngo, D. B. Doman, *Footprint Determination for Reusable Launch Vehicles Experiencing Control Effector Failures.* AIAA Guidance, Navigation and Control Conference and Exhibit, 5-8 August 2002, Monterey CA. AIAA Paper 2002-4775.

[4] K. P. Bollino, I. M. Ross, *Optimal Nonlinear Feedback Guidance for Reentry Vehicles.* AIAA Guidance, Navigation and Control Conference and Exhibit, 21-24 August 2006, Keystone, CO. AIAA Paper 2006-6074.

[5] P. J. Shaffer, I. M. Ross, *Optimal Trajectory Reconfiguration and Retargeting for a Reusable Launch Vehicle.* AIAA Guidance, Navigation and Control Conference and Exhibit, 15-18 August 2005, San Francisco, CA. AIAA Paper 2005-6148.

[6] K. D. Mease, D. T. Chen, P. Teufel, H. Schonenberger, *Reduced-Order Entry Trajectory Planning for Acceleration Guidance.* Journal of Guidance, Control and Dynamics, V. 25 No. 2, March-April 2002.

[7] A. Saraf, J. A. Leavitt, K. D. Mease, *Landing Footprint Computation for Entry Vehicles.* AIAA Guidance, Navigation and Control Conference and Exhibit, 16-19 August 2004, Providence RI. AIAA Paper 2004-4774

[8] Sarah Bairstow, *Reentry Guidance with Extended Range Capability for low L/D Spacecraft*, Masters Thesis, MIT Department of Aeronautics and Astronautics, February 2006.

[9] N. X. Vinh, *Optimal Trajectories in Atmospheric Flight.* Elsevier Scientific Publishing Company, 1981.

[10] T. Takehira, N. X. Vinh, P. T. Kabamba, *Analytical Solution of Missile Terminal Guidance.* Journal of Guidance, Control and Dynamics, V. 21 No. 2 p 342-348, March-April 1998.

[11] J. C. Harpold, C. A. Graves Jr. *Shuttle Entry Guidance*, The Journal of the Astronautical Sciences, Vol. XXVII, No. 3, p 239-268, July-September 1979.

[12] M. C. Jackson, T. M. Straube, T. J. Fill, T. M. Barrows, S. Nemeth, *Onboard Determination of Vehicle Glide Capability for the Shuttle Abort Flight Manager (SAFM)*, IEEE Aerospace and Electronic Systems Society, Core Technologies for Space Systems Conference, Colorado Springs, Nov. 2002.

[13] T. Barrows, *Shuttle Orbiter Phugoid Motion.* Charles Stark Draper Laboratory Internal Memorandum GBB3-01-0172, February 28, 2001.

[14] T. C. Lin, S. McKeel, L. Sproul, T. Shivananda, B. L. Reeves, J. Kealos, P. Fote and N. Thyon, *A Novel Approach for Trajectory Shaping Reentry Vehicle Designs.* AIAA Paper A2000-0636, 2000.

[15] I. M. Ross, *Users Manual for DIDO (Ver. PR 1β): A MATLAB Application Package for Solving Optimal Control Problems*, Naval Postgraduate School Technical Report 04-01.0, February 2004.

[16] T. Lianghui, Y. Jianping, L. Jianjun, Y. Xiaokui, *Reentry Skipping Trajectory Optimization Using Direct Parameter Optimization Method.* AIAA Astrodynamics Specialist Conference and Exhibit, 21-24 August, Keystone CO. AIAA paper 2006-6030.

[17] P. Lu, D. B. Doman, J. D. Schierman, *Adaptive Terminal Guidance for Hypervelocity Impact in Specified Direction.* Journal of Guidance, Control and Dynamics, V. 29 No. 2 p 269-278, March-April 2006.

[18] J. Betts, Survey of Numerical Methods for Trajectory Optimization, J. Guidance, Control and Dynamics, vol. 21, no. 2, pp. 193207, Mar. 1998.

[19] P. Lu, *Intercept of Nonmoving Targets at Arbitrary Time-Varying Velocity.* Journal of Guidance, V. 21 No. 1 p 176-178, 1997. Engineering Notes.

[20] C. R. Hargraves, S. W. Paris, *Direct Trajectory Optimization Using Nonlinear Programming and Collocation.* Journal of Guidance, V. 10 No. 4 p 338-342, 1987.

[21] J. P. Riehl, S. W. Paris, *Comparison of Implicit Integration Methods for Solving Aerospace Trajectory Optimization Problems.* AIAA Astrodynamics Specialist Conference and Exhibit, 21-24 August 2006, Keystone CO. AIAA Paper 2006-6033.

[22] N. X. Vinh, Adolf Buseman, Robert D. Culp, *Hypersonic and Planetary Entry Flight Mechanics.* The University of Michigan Press, Ann Arbor 1980.

[23] P. Fote, V. Yousefian, *Inputs to 3 DOF Maneuvering Trajectory Analysis.* Textron Systems Memo 4638-PF-06-016, August 2006.

[24] Dean R. Chapman, *An Approximate Analytical Method for Studying Entry into Planetary Atmospheres.* NASA Technical Report R-11, 1958.

[25] A. E. Bryson, *Applied Optimal Control: Optimization, Estimation and Control.* Taylor and Francis, January 1, 1975.